

Pedestrian Detection via Thermal Imaging

A Technical Report submitted to the Department of Systems and Information Engineering

Presented to the Faculty of the School of Engineering and Applied Science
University of Virginia • Charlottesville, Virginia

In Partial Fulfillment of the Requirements for the Degree
Bachelor of Science, School of Engineering

Sander Abraham
Spring, 2021

Technical Project Team Members
Navya Annapareddy
Emir Sahin

On my honor as a University Student, I have neither given nor received
unauthorized aid on this assignment as defined by the Honor Guidelines
for Thesis-Related Assignments

Signature _____ Date _____
Sander Abraham

Approved _____ Date _____
Tariq Iqbal, Department of Systems and Information Engineering

A Robust Pedestrian and Cyclist Detection Method Using Thermal Images

Navya Annapareddy^{1,*}, Emir Sahin^{1,*}, Sander Abraham^{1,*}, Md Mofijul Islam¹, Max DePiro², Tariq Iqbal¹

¹Engineering Systems and Environment, University of Virginia, Charlottesville, VA

²Perrone Robotics, Inc., Crozet, VA

*Authors contributed equally to this research

e-mail: {na3au, es3hd, sa3ag, mi8uu}@virginia.edu, mdepiro@perronerobotics.com, tiqbal@virginia.edu

Abstract—Computer vision techniques have been frequently applied to pedestrian and cyclist detection for the purpose of providing sensing capabilities to autonomous vehicles, and delivery robots among other use cases. Most current computer vision approaches for pedestrian and cyclist detection utilize RGB data alone. However, RGB-only systems struggle in poor lighting and weather conditions, such as at night, or during fog or precipitation, often present in pedestrian detection contexts. Thermal imaging presents a solution to these challenges as its quality is independent of time of day and lighting conditions. The use of thermal imaging input, such as those in the Long Wave Infrared (LWIR) range, is thus beneficial in computer vision models as it allows the detection of pedestrians and cyclists in variable illumination conditions that would pose challenges for RGB-only detection systems. In this paper, we present a pedestrian and cyclist detection method via thermal imaging using a deep neural network architecture. We have evaluated our proposed method by applying it to the KAIST Pedestrian Benchmark dataset, a multispectral dataset with paired RGB and thermal images of pedestrians and cyclists. The results suggest that our proposed approach can successfully detect pedestrians and cyclists from thermal images alone.

Index Terms—Pedestrian Detection, Cyclist Detection, Thermal Images

I. INTRODUCTION

Autonomous Vehicles (AVs) will share a significant portion of the existing road systems in the next decade. Not only on highways, but these AVs will also be more prominent in our local roadways [1], [2]. While driving on local roadways, AVs will encounter more people, as people will cross (pedestrians) or share (cyclists) the streets with them. Operating in local roadways will be more challenging for AVs, as the AVs must be able to detect people on and by the road to ensure safety [3]. For example, the AVs must detect a person who wants to cross the street or a biker sharing the lane to ensure safety.

Several approaches have been proposed in the literature to identify pedestrians, detect cyclists, recognize human activities, and predict human motion by utilizing various sensor data [4]–[13]. Among those, the learning approaches that utilize RGB data are found to be less effective during low light, or low contrast conditions [14]. Conditions where visible light detection struggles include weather conditions such as fog, rain, and snow where visibility can be directly obscured or made unclear [15]. Other examples include sun glare during the day and a lack of ambient light during the night. Sun

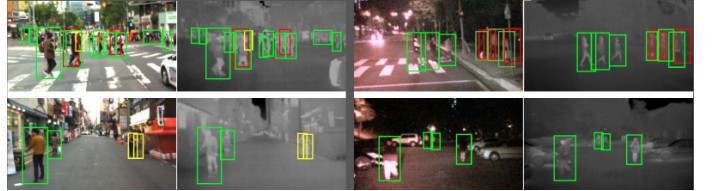


Fig. 1. Example frames from KAIST Multispectral Pedestrian dataset [19]. Image frames are organized into pairs of visible light and LWIR band images. Imaging included both day and night time samples.

glare can cause a whiteout effect when light becomes diffused on objects imaged by RGB cameras [16]. Thermal cameras, however, are more effective than RGB cameras in low visibility conditions due to the detection of infrared energy instead of visible light [17]. Thermal imaging provides high contrast even in environments with low amounts of outdoor light such as during nighttime or in obfuscating weather conditions like fog [18].

Identifying pedestrians and cyclists by utilizing thermal images comes with unique challenges. As most thermal imaging operates in a single band capacity, they are more limited in color range than visible light images. Moreover, humans have relatively consistent internal body temperature and thus thermal intensity. This diminishes the capacity for identifying features of pedestrians such as texture and edges [20].

To address the challenges mentioned above, we have developed a machine learning approach to identify pedestrians and cyclists via thermal images. We utilize a Faster R-CNN model consisting of a Convolutional Neural Network (CNN) and a Region Proposal Network (RPN) [21]. This model composition was chosen as Faster R-CNN can detect objects in real-time providing an opportunity for real world deployment. We evaluated our proposed model on the KAIST Multispectral Pedestrian dataset [22] (see Fig. 1). This dataset contains both thermal and RGB images taken as frames of videos from a vehicle-mounted perspective. The experimental results suggest that our model achieved an average test accuracy of 65.16% and an F1-score of 81.34%.

II. RELATED WORK

A. Shallow Learning Approaches

Several existing works examine pedestrian detection in low light conditions, but without using shallow learning models.

For example, one study used a small handheld thermal camera at night and discovered by getting multiple angles of a person, and passing it through a Histograms of Oriented Gradients algorithm (HoG) [23]. HoG is a method of extracting feature vectors from pixels in images by looking at gradient vectors. A histogram is produced for sections of an image, and analyzed to determine if an object is likely there. Chang et al. applies several other object detection methods in conjunction with HoG, like feature extraction and more importantly, Adaptive Boosting or Adaboost, to detect pedestrians [24].

B. Deep Learning Approaches

Thermal images generally tend to have significantly lower resolution than RGB images due to a need for large pixels to capture the longer wavelength light [25]. The advantage of thermal imaging is in low visibility situations where the lack of visible light impairs regular imaging. For example, Bhattarai and Martinez-Ramon’s work on utilizing thermal input for target detection for firefighting proposed a model that utilized a CNN architecture based on the VGG16 state of the art image classification network [26]. While the results suggest that 2D-CNNs do provide actionable results from thermal images, it is likely that different approaches will result in more robust models since 2D-CNNs require a larger computational overhead which does not satisfy the goal of developing a real time solution.

Several deep learning algorithms have been proposed for pedestrians or person detection [27]–[29]. For example, Vallador developed a multi-scale convolutional network and a convolutional-deconvolutional network to detect people in surveillance footage [30]. The proposed multi-scale convolutional networks utilize sliding windows to generate feature maps of different scales which aims to solve size discrepancy. The convolutional-deconvolutional model connects a deconvolutional layer to the base network to output a segmentation map of the whole image. This allows the model to determine the feature scales it will utilize through training - similar to using an auto encoder for unsupervised learning. This method, while robust, is prone to overfitting and is sensitive to the dataset size [31].

III. DATASETS

Generally, there is a lack of publicly available datasets for thermal imaging, especially regarding pedestrians and cyclists. Currently available datasets include the OSU Thermal Pedestrian dataset and the CSIO thermal object dataset [32]. These datasets were collected with stationary cameras rather than a vehicular mounted camera. In this paper, we conduct experimental evaluation on the KAIST Multispectral Pedestrian dataset [22], a multispectral dataset composed of both pedestrians and cyclists.

The KAIST data is composed of paired annotated thermal images and RGB images of pedestrians and cyclists at multiple times of day. Moreover, the collection was done through vehicle mounted videos mimicking the end goal of real time object identification on a similarly mounted video feed. The

large number of various data samples made it an ideal dataset choice as the input of the model proposed in this paper.

The dataset includes 95,000 paired LWIR and visible light images in both day and night scenarios [33]. Of the 45,000 annotations referencing a type of pedestrian or cyclist, 71.2% were single persons, 19.4% were multiple people, 7.6% were cyclists, and 1.8% were of an uncertain label class. In our experimental evaluation, people and persons were combined into a single label class constituting more than 90% of all annotations. Uncertain labels and frames with missing annotations were excluded from evaluation.

The images from the KAIST benchmark dataset are from a variety of sources, ranging from mounted stationary, handheld, or vehicle mounted cameras. The video output is passed through a series of trackers and their results are evaluated on both center location error and overlap ratio to maintain a consistent camera perspective [19].

The infrared images were collected using long-wavelength IR Cameras which are more robust to visual interference, such as headlights in vehicular contexts. The ground truth annotations were manually collected, labeled by human annotators, and organized into 12 distinct sets of videos decomposed into sequential image frames. As the frames were collected sequentially, not all frames of the KAIST dataset include pedestrians. The dataset is split into 12 sets each with variable amounts of videos, annotations, and class distributions.

IV. PROPOSED APPROACH

We propose a learning model for pedestrian and cyclist detection by utilizing thermal images. The base network of the detector is Faster R-CNN, whose components propose regions of interest through convolutional layer sharing rather than utilizing traditional region proposal algorithms [34]. The proposed model consists of three sequential learning modules (see Fig. 2) with a CNN utilized to feed feature maps to both:

- **Convolutional Neural Network (CNN):** We employ a CNN to extract features from thermal images.
- **Region Proposal Network (RPN):** A neural network, called Region Proposal Network (RPN), is utilized to predict the bounding boxes of objects and propose Regions of Interest (ROI).
- **Fast R-CNN Classifier:** A classifier which utilizes the feature maps from the convolutional network and the regions of interest from the RPN to predict the bounding boxes and classify each bounding box.

A. Pre-processing

The images that the model utilizes are single-channel grayscale image frames taken within the LWIR spectrum. Image processing consists of image normalization to provide the same range of input values across all images.

The pixels of grayscale thermal images contain different values across a single image depending on ambient conditions or the temperature of the outside environment. Normalization results in images with range of values similar within all input data where all the pixel intensity values are adjusted to be in a

statistical range. The input thermal image is normalized with both a mean and standard deviation of 0.5.

B. Convolutional Neural Network

Prior to the object proposal stage, the CNN in our proposed approach extracts feature vectors from the input to create convolutional feature maps. We utilize a pre-trained ResNet50 backbone [35] for the classifier. ResNet50 was trained on and achieved an accuracy of over 92% when evaluated on the ImageNet object recognition database, which is higher than that of the VGG16 architecture utilized within the original Faster R-CNN model.

Typically, three channel RGB inputs are used with ResNet50. To account for the fact our gray-scale input contained only one channel, the single channel was duplicated twice to convert it to three-channel input.

C. Region Proposal Network

Faster R-CNN improves upon the classifier from Fast R-CNN [21] by taking the region proposals generated by the RPN as a baseline in combination with the features of ResNet50 assess ROIs [34]. ROIs are areas suggested by the RPN where objects may be found within a given image. The Region Proposal Network inside of the Faster R-CNN is a neural network found on the last feature map of the convolutional layers in the model. The RPN is trained on top of the CNN of the model.

Faster R-CNN utilizes anchors. An anchor is the central point of a sliding window in a RPN. The RPN includes a classifier and a regressor based upon multiple anchor points on each image. The classifier provides the probability of an annotation having a target object, then the regressor regresses the coordinates of the annotations. The number of anchor points is determined by the image's size, aspect ratio, and the scale of the image. As proposed in the original Faster R-CNN model, we used a 3 scale and 3 aspect-ratio. Correspondingly, each pixel within the input image can have 9 anchor points associated with it. Each input image, in total, can have $9 \times 640 \times 512$ anchor points associated with it. Predictions or cyclists are chosen based on the anchors with the highest overlap with the ground truth which have an Intersection over Union (IoU) score (defined in Section IV-D) higher than 0.7.

In order to train the RPN Network, the following loss function is utilized:

$$L(p_i, t_i) = (1/N_c) \times \sum L_c(p_i, p'_i) + (\lambda/N_r) \times \sum p'_i L_r(t_i, t'_i) \quad (1)$$

where, i is the index of an anchor, p is the probability of being an object or not, t being the vector of four parameterized coordinates of predicted bounding box, t' indicating the parameterized coordinates of the ground truth box. L indicates the \log -loss of two classes (pedestrians and bikers).

This loss is a multi-task loss function, which includes 2 loss functions: The loss of the RPN as well as the loss for classification. The loss can be considered sum of these functions.

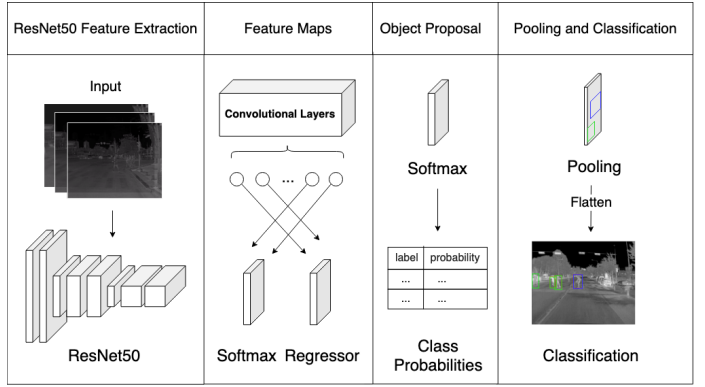


Fig. 2. ROI Pooling and Region Proposal Network Diagram. Following feature extraction via the pre-trained model, the regressor and final Softmax layer are replaced and class probabilities are outputted. Classifications are derived from the ROI pooling process that follows.

$$L = L_c + L_{box} \quad (2)$$

This derivation can be expanded to consider the probabilities of an anchor being an object where p_i is the predicted probability of anchor i being an object, p'_i is the binary ground truth of anchor i being an object, t_i is the predicted four coordinates, t'_i is the ground truth coordinates, N_c is the batch size, N_{box} is the number of anchor locations, and λ is a parameter to equalize the weights of classification and box losses, which is equal to 10. L_1 refers to the smooth L1 loss.

$$r = 1/N_c, w = \lambda/N_{box} \quad (3)$$

$$L(p_i, t_i) = \sum r \times L_c(p_i, p'_i) + w \times \sum p'_i \times L_1(t_i - t'_i) \quad (4)$$

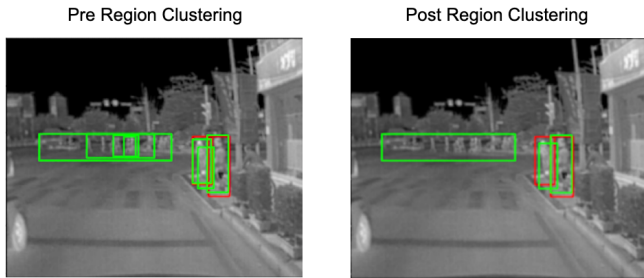
L_c is the loss function for the classification which is the log loss over 2 classes while the loss function L_{box} utilizes L_1 to compute the difference between t_i and t'_i .

$$L_c(p_i, p'_i) = -p'_i \times \log(p_i) - (1 - p'_i) \times \log(1 - p_i) \quad (5)$$

During training, the Fast R-CNN Classifier fine tunes the pre-trained ResNet50 model at the backbone of the Faster R-CNN model. It replaces the last max pooling layer of the ResNet50 with a ROI pooling layer. This pooling layer outputs fixed-length feature vectors of region proposals, replacing the last fully connected and last Softmax layer of the ResNet50 architecture. This provides two final output layers consisting of a Softmax estimator with three classes, outputting a discrete probability per bounding box as well as a bounding-box regression model which predicts offsets relative to the original region of interest for each of the two classes.

ROI pooling occurs during a four-step alternating step training method where the RPN and the Fast R-CNN classifier are trained over one another as described below:

- 1) Fine-tune the RPN for the region proposal task with the pre-trained classifier. Positive samples for the RPN have an IoU of over 0.7 and negative samples have an IoU of 0.3. At the center of each sliding window in the feature map, predict multiple regions of 9 anchors. Calculate loss and train accordingly.



(a) Predictions before region clustering (b) Predictions after region clustering

Fig. 3. Red boxes denote the ground truth bounding box with the labels. Green boxes denote the predictions of our learning model. (a) Our learning approach predicts some objects in a given thermal image. (b) We employ the region clustering approach to detect the appropriate boxes with pedestrians and cyclists.

- 2) Utilizing the current RPN, train the Fast R-CNN classifier and all the layers of the CNN.
- 3) Utilize the current iteration of the Fast R-CNN classifier to initialize further training of the RPN. Only fine tune the layers associated with the RPN without adjusting the shared CNN layers.
- 4) Utilize the current model to only tune the layers specific to the Fast RCNN classifier.

D. Region Clustering

The outputs of the RPN are further clustered to eliminate instances where predictions were self-contained completely or nearly completely in another prediction box. For example, individual pedestrian detection predictions are often present inside a larger prediction encompassing a crowd of pedestrians, similar to the original “person” and “people” labels of the KAIST dataset respectively.

Clustering consisted of three stages. First, predictions that were a proper subset of a larger box were collapsed into the larger one. For the second stage, if a prediction box was not completely superseded but achieved a threshold of overlap of $\geq 50\%$ IoU to another prediction box via Intersection over Union (IoU), the two predictions were merged. The corresponding vertical and horizontal minima and maxima of the two overlapping boxes were averaged (i.e., weighted equally) to create the vertices of the merged prediction.

$$IoU = \frac{A \cap B}{A \cup B} \quad (6)$$

Finally, the third stage of clustering is identical to the second but with a higher threshold of overlap of $\geq 80\%$ IoU. The predicted label of the larger box in each stage of clustering was retained.

E. Model Implementation

We segmented the grayscale thermal images with a scale of 3 and a ratio of 3. We utilized ResNet50 to extract features for the thermal image inputs. We fine tuned every layer under the ResNet50 architecture, including the frozen batch normalization layers to fully train the base convolutional

Metric	Unclustered Model (%)	Clustered Model (%)
F1-score	83.56	81.34
Accuracy	46.87	65.16
Precision	76.28	73.38
Recall	97.69	97.54

TABLE I: Result metrics for the best model for original predictions (before region clustering) and clustered predictions.

network to fit into the novel thermal data. We trained the model for 20 epochs. Due to the large size of the images, the batch size utilized during training was limited to 1. The learning rate was set to 0.0001 during training. Finally, we utilized the Adam optimizer.

V. RESULTS

A. Model Evaluation

The models developed were measured and evaluated on accuracy, precision, and recall. Accuracy was calculated as the rate at which the model correctly identified pedestrians in images. We evaluated an accurate prediction through IoU, which reflects the intersection of the area of the prediction box and ground truth box over the union of the two boxes.

A given prediction was counted as accurate if it had an IoU measure of 0.4 or above. This measure was considered separately for each annotation. In the case of multiple bounding boxes intersecting the same annotation, only the maximum IoU value was considered as a true positive. The model was evaluated on 30% (4 video sets) of the original 12 sets in the KAIST dataset, with the remaining 70% of the data being split into training (67%) and validation (7%) datasets.

The best F1-score, accuracy, precision, and recall for the clustered and unclustered models are presented in Table I. The clustered model outperformed the unclustered model in accuracy (18.29% more). The unclustered model had a slightly higher precision (2.9% more) and F1-score (2.22% more). The two models had nearly equivalent recall.

The proportions and amount of instances of each class (pedestrian and cyclist) are presented in Table II. The class wise proportions of predictions were similar to the proportions of true values. As seen in Table II, cyclists were predicted at a lower rate than the rate they were present in the true labels. Pedestrians were over represented in the predicted labels, indicating that the model has a bias towards the majority class.

Table III presents the true positive and false positive prediction rates per class. The true positive rate for cyclists was higher than that of pedestrians, indicating that the model is more precise in cyclist prediction. This reflects the higher F1-score shown in Table I, as F1-score is a class balanced metric. Some example classification images are presented in Fig. 5.

B. Training Loss

Loss is considered the penalty of a bad prediction and was calculated step wise for each iteration and averaged per epoch. As seen in Fig. 4, the loss starts off high, then exponentially lowers down until it plateaus, indicating model convergence.

	Pedestrians		Cyclists	
Actual	33631	(90.8%)	3417	(9.2%)
Predicted	47726	(92.6%)	3819	(7.4%)

TABLE II: Total values and proportions of class labels in true labels and predictions. Proportions were calculated by the amount of each class present in the total amount of actual and predicted labels.

	Pedestrians		Cyclists	
True Positives	33677	(70.6%)	2966	(77.7%)
False Positives	14049	(29.4%)	853	(22.3%)

TABLE III: Total values and proportions of true and false positive predictions by class. Proportions were calculated over the amount of each type of prediction within each class of labels (pedestrian or cyclist).

C. Discussion

Notably, given that thermal images are low resolution images represented by one-dimensional tensors, both localization and background false positives were frequently observed. Localization false positives occur when a prediction has minimal to significant overlap with a truthful annotation while background false positives occurs when a predicted box has small overlap with a truthful annotation, presumably influenced by background objects or noise. Examples of these false positives can be seen in Fig. 5.

Although the KAIST data we utilized was human annotated, interpolation was used to determine the location of bounding boxes in some frames [19]. This results in missing annotations and background objects incorrectly labeled as pedestrians or cyclists [36]. This is seen in Fig. 3, where our model correctly predicts pedestrians despite there being no associated ground truth label. In this instance, the correct prediction is likely due to the large training set which includes multiple instances of groups of pedestrians that could train the model on the relevant features.

Finally, the region clustering we developed reduced noise

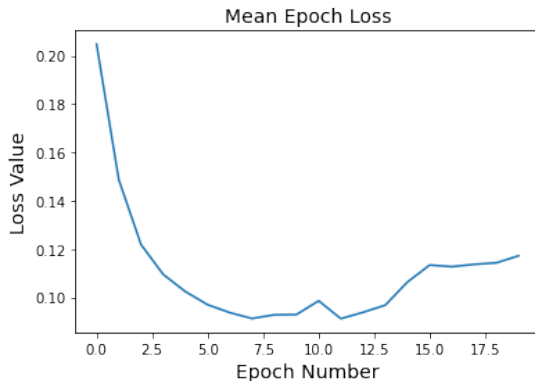


Fig. 4. Training loss over time. The mean loss values over all the iteration of an epoch was taken.

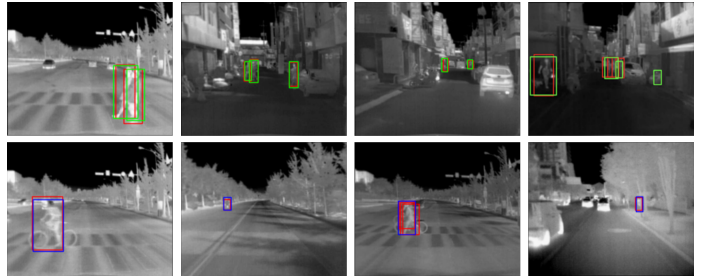


Fig. 5. Example predictions for pedestrians (top row) and cyclists (bottom row). Red boxes denote a ground truth bounding box. Green indicates a predicted pedestrian label. Blue indicates a predicted cyclist label.

within predictions with respect to bounding boxes that were subsets or near-subsets of another prediction. As seen in Table I, clustered predictions achieved a higher accuracy than unclustered predictions. In any given clustering instance, we took the label of the predicted box with the greater area as the label for the merged prediction. This has the potential of disregarding predictions for cyclists in proximity to predictions of pedestrian(s), further contributing to the class imbalance of predicted labels.

VI. FUTURE WORK

We are planning to explore the CNN-LSTM model to extract temporal features from RGB and thermal images to improve the accuracy of pedestrian and cyclist detection in our future work. CNN-LSTM models have been successively utilized to extract spatial-temporal features from grayscale images [37]. In such a model, the LSTM learns temporally global features of videos while the CNN captures the spatial features found in the videos [33]. Previous work has identified that while LSTM models in long-term intent prediction do improve baseline accuracy, there is a trade-off with mean position error rate [38]. Taking a time series approach will require the data to be organized by sequence rather than concatenated frames by class. As an alternative, 3D-CNN and ConvLSTM models can also be utilized to extract spatial-temporal features to capture temporally local features and successively learn short and long-term spatial and temporal features [39], respectively, which we plan to explore in our future work.

Finally, to handle input images of differing sizes, a Multi-Scale CNN (MS-CNN) model could be implemented. The model utilizes several sub-networks of layers optimized for different sizes and then combines the outputs at the end. This method has the advantage of combining feature identification and classification within a combined system, something that is often disjointed in time dependent data.

VII. CONCLUSION

As thermal imaging has become cheaper and more widely available, it has been increasingly implemented in vehicles to improve nighttime and low-visibility pedestrian detection. Thus, it is more critical than ever that robust pedestrian detection via thermal imaging be developed to provide or

augment an effective means of accurate pedestrian and cyclist detection. In this paper, we propose a robust method of identifying pedestrians and cyclists via thermal images. The experimental results suggest that our proposed approach is able to make recommendations with minimal false negatives (0.53%) and a high F1 score (81.34%). These findings imply that our approach creates a robust baseline to build upon, especially for use in multi spectral detection methods.

ACKNOWLEDGMENT

The authors would like to thank Perrone Robotics, Inc. for their support during this research. The authors also acknowledge the Research Computing at UVA for providing computational resources and technical support that have contributed to the results reported within this publication.

REFERENCED CODE

All the referenced and supporting code can be found at the corresponding GitHub repository (<https://github.com/ncanna/thermal-pedestrian-detection>).

REFERENCES

- [1] W. Brenner and A. Herrmann, *An Overview of Technology, Benefits and Impact of Automated and Autonomous Driving on the Automotive Industry*, pp. 427–442. Berlin, Heidelberg: Springer Berlin Heidelberg, 2018.
- [2] A. Alsalmán, L. N. Assi, S. Ghotbi, S. Ghahari, and A. Shubbar, “Users, planners, and governments perspectives: A public survey on autonomous vehicles future advancements,” *Transportation Engineering*, vol. 3, p. 100044, 2021.
- [3] J. Janai, F. Güney, A. Behl, and A. Geiger, “Computer vision for autonomous vehicles: Problems, datasets and state of the art,” 2021.
- [4] M. M. Islam and T. Iqbal, “HAMLET: A hierarchical multimodal attention-based human activity recognition algorithm,” in *IROS*, 2020.
- [5] M. M. Islam and T. Iqbal, “Multi-gat: A graphical attention-based hierarchical multimodal representation learning approach for human activity recognition,” in *IEEE Robotics and Automation Letters (RA-L)*, 2021.
- [6] T. Iqbal, S. Li, C. Fourie, B. Hayes, and J. A. Shah, “Fast online segmentation of activities from partial trajectories,” in *ICRA*, 2019.
- [7] T. Iqbal, S. Rack, and L. D. Riek, “Movement coordination in human-robot teams: A dynamical systems approach,” *IEEE Transactions on Robotics*, vol. 32, no. 4, pp. 909–919, 2016.
- [8] M. S. Yasar and T. Iqbal, “A scalable approach to predict multi-agent motion for human-robot collaboration,” in *IEEE Robotics and Automation Letters (RA-L)*, 2021.
- [9] M. S. Yasar and T. Iqbal, “Improving human motion prediction through continual learning,” in *ACM/IEEE Int. Conf. on Human-Robot Interaction (HRI), LEAP-HRI Workshop*, 2021.
- [10] T. Iqbal and L. D. Riek, “A method for automatic detection of psychomotor entrainment,” *IEEE Transactions on affective computing*, vol. 7, no. 1, pp. 3–16, 2015.
- [11] T. Iqbal, M. J. Gonzales, and L. D. Riek, “Joint action perception to enable fluent human-robot teamwork,” in *Proc. of IEEE Robot and Human Interactive Communication*, 2015.
- [12] T. Iqbal and L. D. Riek, “Coordination dynamics in multi-human multi-robot teams,” *IEEE Rob. and Auto. Letters (RA-L)*, 2017.
- [13] T. Iqbal and L. D. Riek, “Temporal Anticipation and Adaptation Methods for Fluent Human-Robot Teaming,” in *IEEE International Conference on Robotics and Automation (ICRA)*, 2021.
- [14] J. Arrospe, L. Salgado, M. Nieto, and F. Jaureguizar, “On-board robust vehicle detection and tracking using adaptive quality evaluation,” in *2008 15th IEEE International Conference on Image Processing*, pp. 2008–2011, 2008.
- [15] Y. W. Xu, X. B. Cao, and H. Qiao, “Optical camera based pedestrian detection in rainy or snowy weather,” in *Fuzzy Systems and Knowledge Discovery* (L. Wang, L. Jiao, G. Shi, X. Li, and J. Liu, eds.), (Berlin, Heidelberg), pp. 1182–1191, Springer Berlin Heidelberg, 2006.
- [16] K. Yoneda, N. Suganuma, R. Yanase, and M. Aldibaja, “Automated driving recognition technologies for adverse weather conditions,” *IATSS Research*, vol. 43, no. 4, pp. 253–262, 2019.
- [17] E. Yurtsever, J. Lambert, A. Carballo, and K. Takeda, “A survey of autonomous driving: Common practices and emerging technologies,” 2019.
- [18] E. Bernard, N. Rivière, M. Renaudat, M. Péalat, and E. Zenou, “Active and thermal imaging performance under bad weather conditions,” in *6th International Symposium on Optronics in Defence and Security (OPTRO 2014)*, (Paris, FR), 2014. Thanks to 3AF.
- [19] S. Hwang, J. Park, N. Kim, Y. Choi, and I. S. Kweon, “Multispectral pedestrian detection: Benchmark dataset and baselines,” in *Proceedings of IEEE Conference on Computer Vision and Pattern Recognition (CVPR)*, 2015.
- [20] N. Negied, E. Hemayed, and M. Fayek, “Pedestrians’ detection in thermal bands—critical survey,” *Journal of Electrical Systems and Information Technology*, vol. 106, 06 2015.
- [21] R. B. Girshick, “Fast R-CNN,” *CoRR*, vol. abs/1504.08083, 2015.
- [22] Y. Choi, N. Kim, S. Hwang, K. Park, J. S. Yoon, K. An, and I. S. Kweon, “Kaist multi-spectral day/night data set for autonomous and assisted driving,” *IEEE Transactions on Intelligent Transportation Systems*, vol. 19, no. 3, pp. 934–948, 2018.
- [23] J. Kim, “Pedestrian detection and distance estimation using thermal camera in night time,” in *2019 International Conference on Artificial Intelligence in Information and Communication (ICAIIIC)*, pp. 463–466, 2019.
- [24] S. Chang, F. Yang, W. Wu, Y. Cho, and S. Chen, “d on hog feature,” in *Proceedings 2011 International Conference on System Science and Engineering*, pp. 694–698, 2011.
- [25] T. Luhmann, J. Piechel, and T. Roelfs, *Geometric Calibration of Thermographic Cameras*, pp. 27–42. Dordrecht: Springer Netherlands, 2013.
- [26] M. Bhattarai and M. Martínez-Ramón, “A deep learning framework for detection of targets in thermal images to improve firefighting,”
- [27] V. John, S. Mita, Z. Liu, and B. Qi, “Pedestrian detection in thermal images using adaptive fuzzy c-means clustering and convolutional neural networks,” in *2015 14th IAPR International Conference on Machine Vision Applications (MVA)*, pp. 246–249, 2015.
- [28] J. Liu, S. Zhang, S. Wang, and D. N. Metaxas, “Multispectral deep neural networks for pedestrian detection,” *CoRR*, vol. abs/1611.02644, 2016.
- [29] W. Li, D. Zheng, T. Zhao, and M. Yang, “An effective approach to pedestrian detection in thermal imagery,” in *2012 8th International Conference on Natural Computation*, pp. 325–329, 2012.
- [30] E. Valldor, “Person detection in thermal images using deep learning.”
- [31] Z. Cui, W. Chen, and Y. Chen, “Multi-scale convolutional neural networks for time series classification,” 2016.
- [32] A. Akula, N. Khanna, R. Ghosh, S. Kumar, A. Das, and H. Sardana, “Adaptive contour-based statistical background subtraction method for moving target detection in infrared video sequences,” *Infrared Physics Technology*, vol. 63, pp. 103 – 109, 2014.
- [33] S. Hwang, J. Park, N. Kim, Y. Choi, and I. S. Kweon, “Multispectral pedestrian detection: Benchmark dataset and baseline,” in *2015 IEEE Conference on Computer Vision and Pattern Recognition (CVPR)*, pp. 1037–1045, IEEE.
- [34] S. Ren, K. He, R. Girshick, and J. Sun, “Faster r-cnn: Towards real-time object detection with region proposal networks,” 2016.
- [35] K. He, X. Zhang, S. Ren, and J. Sun, “Deep residual learning for image recognition,” 2015.
- [36] J. Liu, “Exploiting multispectral and contextual information to improve human detection,” 2017.
- [37] M. Z. Islam, M. M. Islam, and A. Asraf, “A combined deep cnn- lstm network for the detection of novel coronavirus (covid-19) using x-ray images,” *Informatics in Medicine Unlocked*, vol. 20, p. 100412, 2020.
- [38] S. Ahmed, M. N. Huda, S. Rajbhandari, C. Saha, M. Elshaw, and S. Kanarachos, “Pedestrian and cyclist detection and intent estimation for autonomous vehicles: A survey,” vol. 9, no. 11, p. 2335.
- [39] L. Zhang, G. Zhu, P. Shen, J. Song, S. A. Shah, and M. Bennamoun, “Learning spatiotemporal features using 3dcnn and convolutional lstm for gesture recognition,” in *2017 IEEE International Conference on Computer Vision Workshops (ICCVW)*, pp. 3120–3128, 2017.

The Hummingbird Light Attack Aircraft

A Technical Report submitted to the Department of Mechanical and Aerospace Engineering

Presented to the Faculty of the School of Engineering and Applied Science
University of Virginia • Charlottesville, Virginia

In Partial Fulfillment of the Requirements for the Degree
Bachelor of Science, School of Engineering

Sander Abraham
Spring, 2021

Technical Project Team Members

Lori Abbed
Justice Allen
Marcus Dozier
Eli Kidd
Landry Myers
D'Michael Thompson

On my honor as a University Student, I have neither given nor received
unauthorized aid on this assignment as defined by the Honor Guidelines
for Thesis-Related Assignments

Signature _____ Date _____

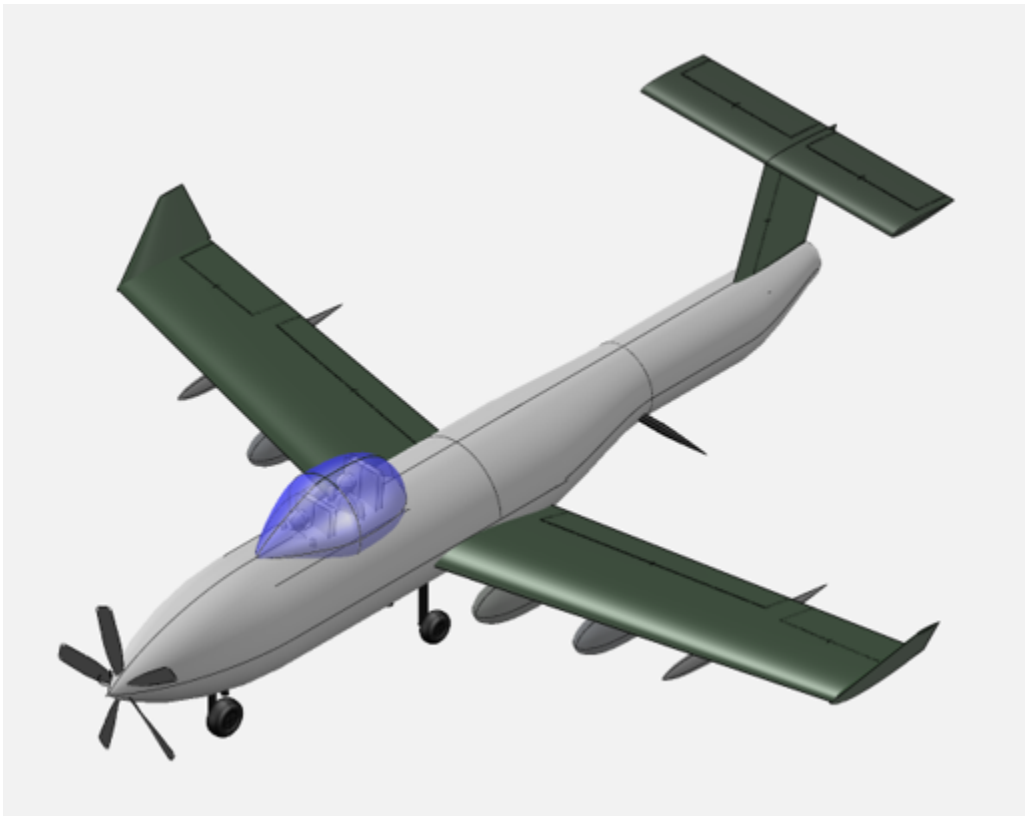
Sander Abraham

Approved _____ Date _____

Jesse Quinlan, Department of Mechanical and Aerospace Engineering

The Hummingbird

AIAA 2020-2021 Undergraduate Design Proposal



MAE 4660

Mechanical and Aerospace Engineering

University of Virginia

May 14, 2021

I Team Hummingbird

Name	Signature	AIAA Number
Lori Abbed		1180294
Sander Abraham		1141521
Justice Allen		1180099
Marcus Dozier		1180513
Eli Kidd		965543
Landry Myers		1230790
D'Michael Thompson		1230789

Name	Signature	AIAA Number
Dr. Jesse Quinlan		306245

Contents

I	Team Hummingbird	i
II	Executive Summary	1
III	Vehicle Summary	2
IV	Introduction	2
V	Design Process	3
VI	Sizing	4
	VI.1 Initial TOGW	4
	VI.2 Initial Fuselage	6
VII	Configuration	9
	VII.1 Concept Down Select	9
	VII.2 Configuration Iteration	9
	VII.3 Initial Configuration	9
	VII.4 Fuselage	9
VIII	Aerodynamics	13
	VIII.1 About VSPAERO	13
	VIII.2 Initial Wing Design	14
	VIII.3 Increasing L/D	15
	VIII.4 Final Wing Aerodynamics	18
IX	Stability and Control	19
	IX.1 Tail Sizing	19
	IX.2 Static Margin, Stability Derivatives, Control Surfaces	20
X	Propulsion	21
	X.1 Engine Selection Process	21
	X.2 About GasTurb	24
	X.3 Establishing an Initial Model	25

X.4	Current PT6-A GasTurb 13 Model	26
X.5	Rotor	42
X.6	Initial Rotor Model	43
XI	Structural Design	49
XI.1	Wing Stress	49
XI.2	V-n diagram	51
XII	Weight Statement	53
XII.1	Initial Estimates	53
XII.2	FLOPS Weight Analysis	54
XIII	Performance	55
XIII.1	Takeoff and Landing Field Length	55
XIII.2	Mission Performance	56
XIII.3	Payload-Range	57
XIII.4	Survivability	58
XIV	Cost Estimation and Analysis	62
XIV.1	Overview of Cost Methodology	63
XIV.2	Assumptions	63
XIV.3	Calibration	64
XIV.4	Results	65
XV	Conclusion	66
XVI	Acknowledgements	66
	Appendices	72
I	Initial TOGW Calculation	72
II	Takeoff and Landing Assumptions	72
III	Noise Signatures	73
III.1	XROTOR Outputs	73
III.2	Matlab Script for Service Ceiling	75
IV	Cost Variables	76

List of Figures

1	Highlighted Features	1
2	Dimensioned Diagram of the Hummingbird	2
3	Initial Objective Tree	3
4	Sensitivity Analysis of the Takeoff Field Length	4
5	Empty Weight Calculations as a Function of TOGW	5
6	Isometric View of Initial Aircraft In Solidworks	8
7	Dimensioned Side View of Initial Aircraft In OpenVSP, Sections A and B Shown	9
8	Cross-Section Side View of Final Aircraft In OpenVSP, Major Components Shown	12
9	Comparison of L/D by Configuration of the Initial Wing Design	15
10	L/D Comparison With and Without Winglets	15
11	Revised Wing Design Including: Area Increase, Sweep, Taper, and Incidence	16
12	For -6° to 20° AoA: (a) L/D (b) C_L (c) C_D	17
13	Final Wing Design	18
14	Output of the VSPAERO Stability Analysis	19
15	Reverse Flow Turboprop [1]	22
16	Afterburning Turbojet Engine Schematic [2]	22
17	Separate Exhaust Turbofan Engine Schematic [2]	23
18	Service Regions for Various Propulsion Systems [3]	24
19	PT-6A Total Temperatures and Pressures By Engine Stage [4]	25
20	T-S and P-V Diagrams	28
21	Total Temperature and Pressure Graphs By Engine Stage (Left: GasTurb, Right: PT-6A manual)	28
22	Parametric Analysis, Altitude and Mach Number vs. Shaft Power Delivered	29
23	Parametric Analysis, Altitude and Mach Number vs. Net Thrust	29
24	Parametric Analysis, Altitude and Mach Number vs. Thrust Specific Fuel Consumption	30
25	Parametric Analysis, Altitude and Mach Number vs. Thermal Efficiency	31

26	The Brayton Cycle [5]	32
27	An additively manufactured component's complex cross section [6]	32
28	Expected Future Engine Temperature Capabilities [7]	34
29	A Trend of Engine Thermodynamic Efficiency Improvements By Year [8]	35
30	A Trend of Engine Propulsive Efficiency Improvements By Year [8]	36
31	T-S and P-V Diagrams	39
32	Total Temperature and Pressure Graphs By Engine Stage (Left: 2025 PT-6A GasTurb, Right: Current PT-6A GasTurb)	40
33	Parametric Analysis, Altitude and Mach Number vs. Shaft Power Delivered	40
34	Parametric Analysis, Altitude and Mach Number vs. Net Thrust	41
35	Parametric Analysis, Altitude and Mach Number vs. Thrust Specific Fuel Consumption	41
36	Parametric Analysis, Altitude and Mach Number vs. Thermal Efficiency	42
37	Initial Rotor Model Front Geometry	44
38	Initial Rotor Model Chord Distribution (c/R vs r/R)	45
39	Initial Rotor Model Blade Twist Angle Distribution (β° vs r/R)	46
40	Final Rotor Model Chord Distribution (c/R vs r/R)	47
41	Final Rotor Model Blade Twist Angle Distribution (β° vs r/R)	48
42	Final Rotor Model Front Geometry	49
43	Wing Configuration	50
44	FEA of the Wing	51
45	V-n Diagram	52
46	V-n Diagram with Gust Lines With ULF = 3.75	53
47	Sensitivity Analysis of the Takeoff Field Length	55
48	Design Mission Sequence	56
49	Payload Range Diagram. Note that the bottom of the chart is set at the OEW	58
50	XROTOR Acoustic Analysis for Takeoff Case	59
51	XROTOR Acoustic Analysis for Cruise Case	60
52	XROTOR Acoustic Analysis for Service Ceiling Case	61

List of Tables

1	Key Vehicle Characteristics	2
2	Tools Used	3
3	Weight Fraction Estimates by Flight Segment	5
4	Initial Fuselage Sizing Complete Table of Weights and Dimensions	6
5	Initial Section C Component Parameters	8
6	Initial Fuselage Sizing Summary of Relevant Parameters	8
7	Final Fuselage Sizing Complete Table of Weights and Dimensions	10
8	Final Fuselage Sizing Electronics	11
9	Fuselage Sizing Summary of Relevant Parameters	11
10	Initial Fuselage Sizing Additional Design Information	11
11	Default Armaments List	12
12	Comparison of Wing Design Parameters Between Initial Design and State-of-the-Art	14
13	Approximated Temperature & Pressure Values For PT-6A	25
14	PT-6A GasTurb Additional Input Values	26
15	PT-6A Turboprop Propeller Inputs	27
16	Current Turboprop Model Flow Rates, Total Temperature, and Total Pressure	27
17	PT-6A GasTurb Turboprop Model Relevant Outputs	27
18	Improved PT-6A GasTurb “Basic Data” Input Values	37
19	PT-6A GasTurb Additional Input Values	38
20	Improved Turboprop Model Flow Rates, Total Temperature, and Total Pressure	39
21	Improved PT-6A GasTurb Turboshaft Model Relevant Outputs	39
22	XROTOR Inputs for Initial Rotor Model	43
23	Design Speeds from the V-n Diagram	52
24	Empirical Weight Estimations	53
25	Weight Statement	54

26	Takeoff Field Lengths	56
27	Landing Field Lengths	56
28	Design Mission Results. 3126.9 lb fuel burn, Total Range of 836.1 nmi.	57
29	Ferry Mission Results. 1325.3 lb fuel burn, Total Range of 950 n mi.	57
30	Possible Configurations to Achieve More Range	58
31	XROTOR Inputs for Initial Rotor Model	59
32	XROTOR Outputs for Takeoff Case	59
33	XROTOR Inputs for Cruise Case *XROTOR crash, lower power than available used.	60
34	XROTOR Outputs for Cruise Case	60
35	XROTOR Outputs for Service Ceiling Case *XROTOR crash, lower power than available used.	61
36	XROTOR Outputs for Service Ceiling Case	61
37	Input Variables and Assumptions	64
38	Initial TOGW Calculation Varying TOGW by 1000 lb	72
39	Finer Initial TOGW Calculation Varying TOGW by 200 lb	72
40	Assumed Values for Takeoff and Landing Calculations	72
41	Variables Nomenclature	76

II Executive Summary

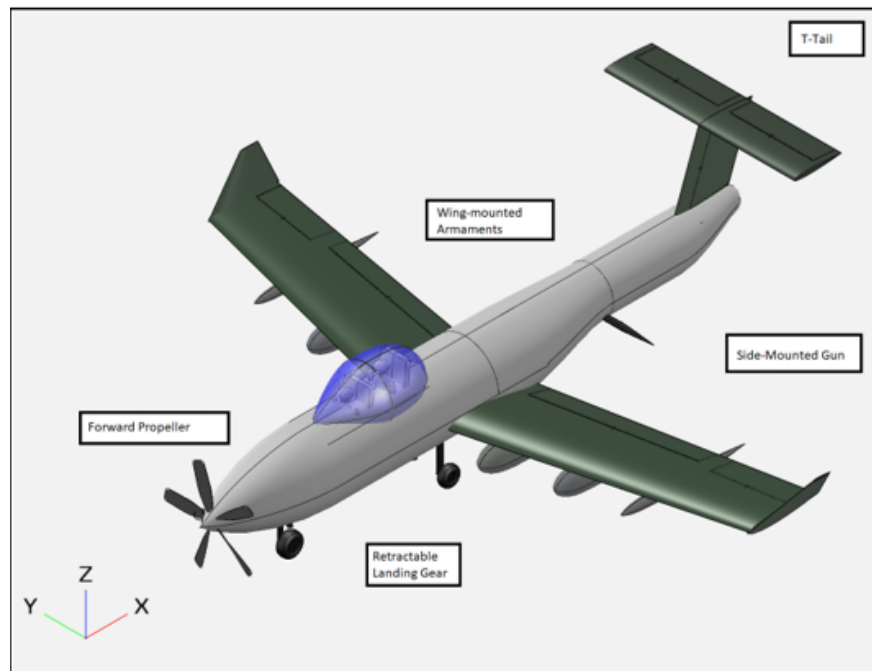


Figure 1: Highlighted Features

Advancements in military aircraft have pushed the boundaries of a plane's capabilities, but also cost. This creates a niche for a cheap aircraft that can be placed in remote and underdeveloped locations and provide close air support that other aircraft would be too expensive to operate. This report provides a preliminary for a Light Attack Aircraft as requested in the RFP by the AIAA Student Design Competitions [9]. The RFP set out requirements for a light fighter plane capable of carrying two pilots, armaments, and an integrated gun on a loiter design mission. Additionally, the plane must be able to takeoff and land from short austere runways, and meet other performance and operational requirements while minimizing cost. This report presents the design of The Hummingbird as a proposal to this RFP. The Hummingbird's notable features include a single forward mounted turboprop engine, a T-tail empennage, wing-mounted payload, and a deployable side-mounted gun—all seen in figure 1. The Hummingbird, with a full payload, has a maximum range of 1740 nmi and costs \$29 million to acquire and \$1743 per flight hour to operate. The Hummingbird has a TOGW of 14433 lb and an empty weight of 8002 lb. This design is able to meet all requirements set out in the RFP.

III Vehicle Summary

Table 1: Key Vehicle Characteristics

TOGW (OEW)	14433 (8002) lb
Design Mission Block Fuel Burn	3126.9 lb
TSFC at Cruise	0.54 lb/(h·lbf)
Takeoff/Landing Field Length	3313 ft / 2555 ft
Takeoff/Landing Field Length at 6000 ft	3931 ft / 2981 ft
Service Ceiling	34000 ft
CL_{cruise} / CL_{max}	0.81 / 2.75
Aircraft Length	42.7 ft
Wing Area (AR)	42.9 ft
Wing Span	278.85 ft ² (6.6)
Acquisition Cost	\$29,322,000
Operating Cost per Flight Hour	\$1742.86

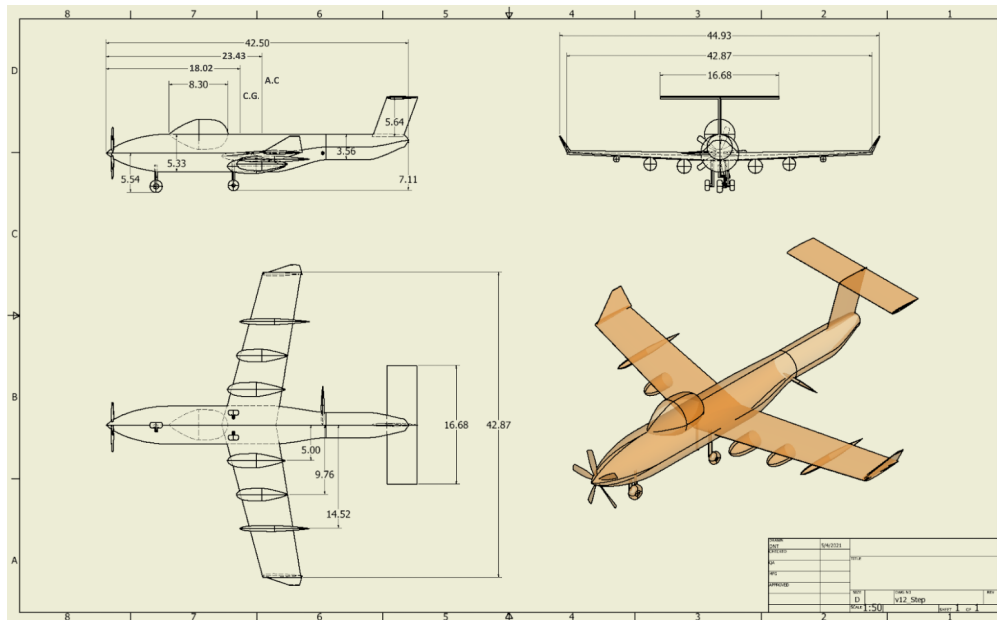


Figure 2: Dimensioned Diagram of the Hummingbird

IV Introduction

The AIAA Undergraduate RFP calls for a low cost light attack aircraft capable of fulfilling the close air support role traditionally fulfilled by a helicopter. Furthermore, the plane must be able to operate out of an austere field. These explicit goals imply several notional design objectives and associated measures for performance. Figure 3 outlines the

initial objective tree created after analyzing the RFP objectives. The intermediate levels represent implied objectives, with the last level indicating possible metrics to measure performance.

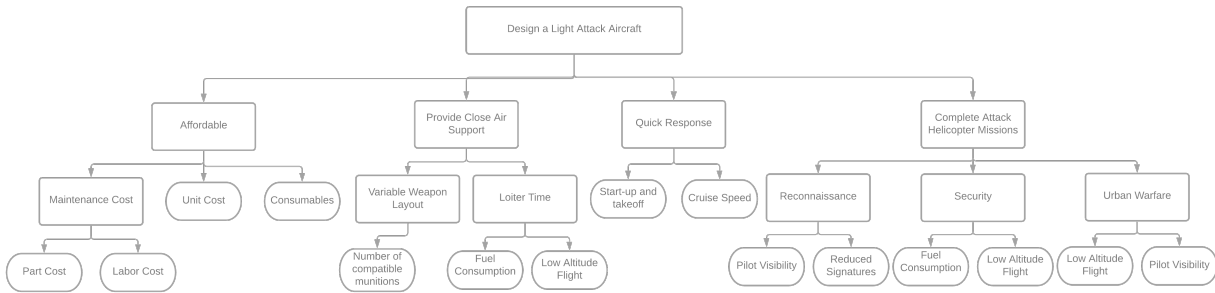


Figure 3: Initial Objective Tree

To this end, the Hummingbird was designed with these goals in mind. For instance, the affordability objective was kept in mind throughout the design process. It influenced design choices to minimize complexity and utilize existing components. For example, the engine selected was the Pratt & Whitney Canada PT6A-6 Variant, a commonly used and well known engine.

V Design Process

To design the aircraft, both empirical and model based methods were used. Empirical methods, such as the ones provided in Nikolai and Roskam set the starting point for further design work [3, 10, 11]. Initial values were assumed to be similar to those of existing aircraft such as the Fairchild Republic A-10 Thunderbolt II or the Embraer EMB 314 Super Tucano since these and other aircraft had similar design objectives and purposes. From there, equations were used to further the design until all major values had been propagated through and an initial model existed. Those values would serve as the inputs for model based design. Table 2 provides the tools and what regime of analysis they conducted.

Table 2: Tools Used

Program	Applied Area
AAA [12]	Cost Analysis
The Flight Optimization System (FLOPS) [13]	Mission Analysis and Weight Estimation
GasTurb [14]	Engine Modeling
OpenVSP [15]	Modeling
Solidworks [16]	Structural Analysis
VSP Aero [15]	Aerodynamics
XROTOR [17]	Propeller Analysis

From there the output would be compared to the empirical results as a cross reference. From there trade studies are conducted like the one shown below in Figure 26. Results are also compared to other aspects of the aircraft as a check for agreement. This process is iterated until a closed loop is formed with a satisfactory output achieved, and then continually updated as further design progress is made.

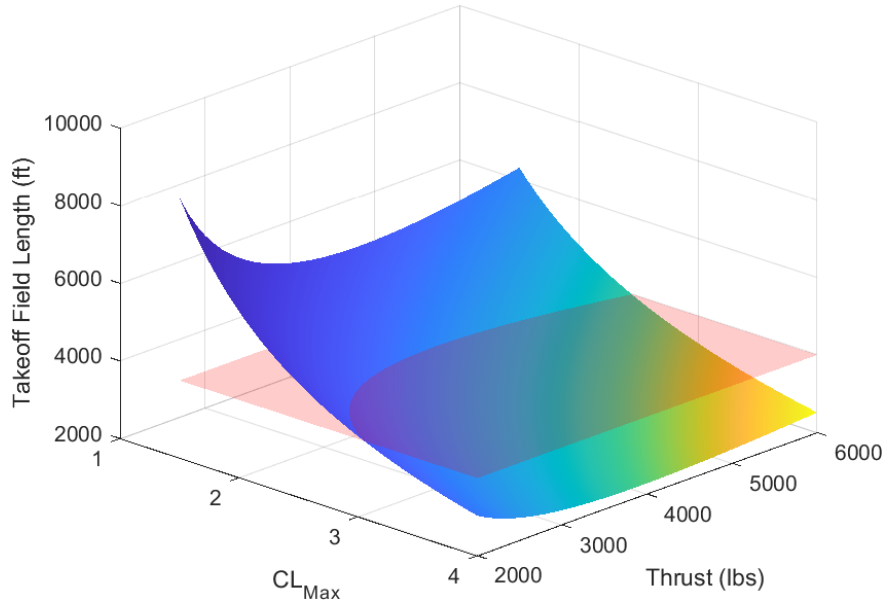


Figure 4: Sensitivity Analysis of the Takeoff Field Length

VI Sizing

VI.1 Initial TOGW

The initial Takeoff Gross Weight serves as the first variable to be defined and form the basis for further initial designing. To get the initial TOGW a weight fraction method was used. From the design mission, weight ratios are estimated for each phase of the flight. Taking these weight fractions, shown in Table 3 and the initial TOGW estimation of 8000 lb, the fuel weight can be calculated. The fixed weight was estimated at 3600 lb. Using equations 1 and 2, the empty weight and required empty weight can be calculated [3].

$$W_{empty\ available} = W_{TO} - W_{fuel} - W_{fixed} \quad (1)$$

$$W_{empty\ required} = 0.911 \cdot W_{TO}^{0.947} \cdot 0.84 \quad (2)$$

From there a new TOGW is estimated and the process is repeated until the empty weight and required empty weight converge. Appendix I has the values that were calculated tabulated and Figure 5 plots the Empty Weight and Empty Weight Required calculated from this method.

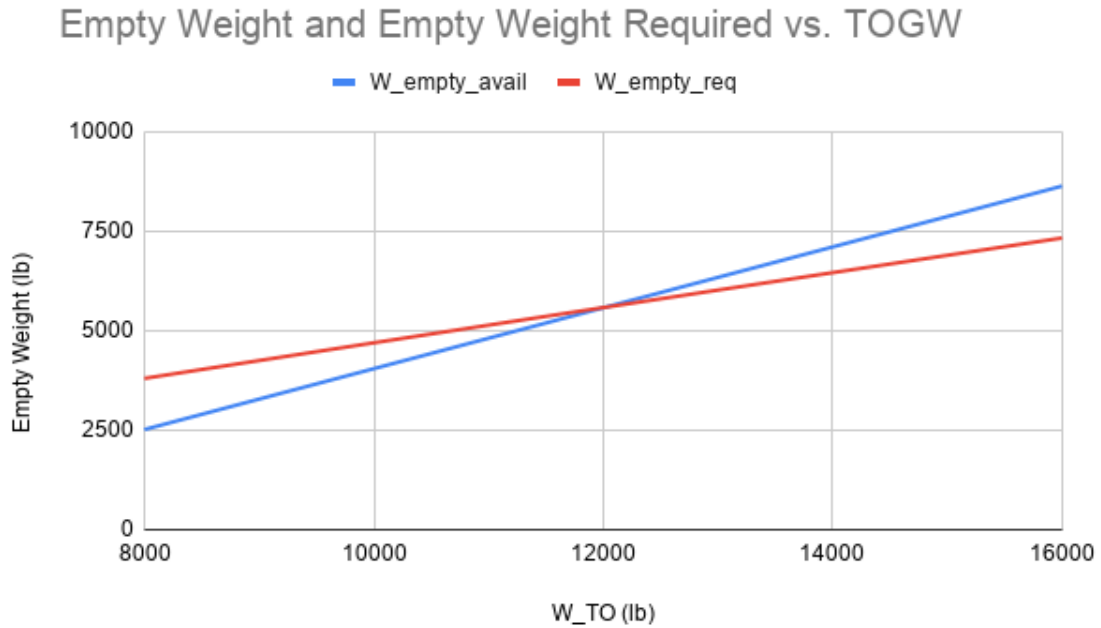


Figure 5: Empty Weight Calculations as a Function of TOGW

Table 3: Weight Fraction Estimates by Flight Segment

Mission Profile	Weight Ratio (formula)	Weight Ratio
Start/take off	w2/w1	0.975
Climb out to cruise	w3/w2	0.975
Cruise out	w4/w3	0.985
Descent	w5/w4	0.980
Loiter	w6/w5	0.898
Climb out	w7/w6	0.980
Cruise back	w8/w7	0.985
Descent/land/taxi	w9/w8	0.990
Reserve (climb to 3000)	w10/w9	0.990
Reserve (Loiter 45 mins)	w11/w10	0.980

$$Payload\ Growth\ Factor = \frac{dW_{TO}}{dW_{fixed}} \quad (3)$$

From these calculations a payload growth factor of 3.13 can be calculated from equation 3. As a result an initial TOGW of 12018 lb was found. This number seemed reasonable as it weighed similarly to other aircraft in its class with a shared purpose.

VI.2 Initial Fuselage

Initial fuselage sizing was based around the general aviation sizing procedures put forth by Nicolai, where the aircraft is approximated as having a cylinder fuselage section (termed Section A in our analysis) and a rear-facing cone of the same diameter as a tail section (termed section B) [3]. The analysis was performed using parameters such as maximum fuel weight, cruise velocity and altitude, and estimated empennage dimensions and weights from a previous take-off gross weight (TOGW) analysis. Several basic assumptions and approximations were laid out by Nicolai, which include: assuming the wings (and payload on wings) will be located at center of gravity (will not be included in calculations), and the fuselage's exterior material and structure is centered around the aircraft's center of gravity (not considered during this analysis). Analysis began using the Embraer EMB 314 Super Tucano length and estimated width of 37.34 and 4.66 feet respectively (derived from ideal thickness to length ratio for subsonic aircraft) [18].

Section A, Main Fuselage

The cylindrical section was developed to house the PT-6A Turboprop engine, the two passengers (from RFP), their cockpit furnishings, fuel tanks (including mechanical equipment), electronics, and structural internal wing sections [9]. The engine was approximated as a cylinder with dimensions and weights resembling that of a PT-6A turboprop engine, similar to that of the Super Tucano. Exact specifications are shown in Table 4.

Table 4: Initial Fuselage Sizing Complete Table of Weights and Dimensions

Component	Total Weight (lb)	Length (ft)	Diameter/ Width (ft)	Approximated Shape
Two Pilots	360	N/A	N/A	N/A
Cockpit Furnishings	895.97	8.33	4.67	Square Prism
JP-4 Fuel (Maximum Volume)	2828.12	9.07	4.67	Half - Cylinder
JP-4 Fuel (Minimum Volume)	141.41	N/A	N/A	N/A
Flight Electronics	1633.5	3.42	3.42	Cube
PT-6A Turboprop Engine	598	6.00	3	Cylinder
Initial Empennage	78.23	N/A	N/A	Point

The estimated passenger weight (including gear) was reported as 180 lbs (given by Nicolai). Furnishing weight was determined as a function of passenger quantity and flight dynamic pressure, as described by Nicolai, this weight includes ejection seats for all passengers and assumes the aircraft is subsonic. The following equation was used [3]:

$$W_{Furnishings} = 34.5 \cdot pq^{0.25} + 22.8 \cdot \left(\frac{pq}{100}\right)^{0.743} \quad (4)$$

where p is the number of passengers and q is the dynamic pressure. The dynamic pressure was calculated at cruise velocity and altitude, as calculated in the TOGW analysis, which yielded 2438.495 lb/(ft²s²), and the number of passengers was input as 2. The results are shown in Table 4. Nicolai approximated for 2 passengers a cockpit length of

100 inches, or roughly 8.33 feet. Next, using a known required maximum fuel weight from TOGW analysis, we could calculate a fuel volume using the density of JP-4 jet fuel. The fuel tank volume, which includes the required fuel volume, was calculated as well; calculations assumed an internally mounted bladder tank with a packing factor of 6.5 (that took into account the mechanical equipment required by the fuel system). This fuel tank volume could be represented in an initial model as a half-cylinder, with the same diameter as the fuselage, which would be mathematically used to determine the required length of the fuel tank. A general electronics setup table for all types of aircraft was given by Nicolai, this table was likely outdated and electronics in modern times are much lighter, so this estimate is likely conservative. After performing brief research into the nature of the electronics included in his documentation, slight modifications were made to the final list of selected electronics to reduce weight, mainly by limiting the selected components to only those necessary for the flight and survival of a small attack aircraft (specifically larger radar and reconnaissance components were omitted). The electronics from Nicolai were often missing volumes or weights, so an average electronics density was calculated from the known electronics and applied to the full table of components. This allowed a general volume of electronics to be created. Packaging and optimal functionality and maintenance placement was not considered in the initial sizing and all electronics were assumed to fit within a box. A generalized electronics weight and volume is depicted in Table 4. For this section, the total length of the section was determined by summing the lengths of the relevant components (the cockpit, fuel tanks, electronics, and engine). Obviously, this would lead to an over estimation of total length, as the full fuselage volume is not utilized but it leaves room for components like the structural internal wing, wiring, and fuselage structure. Further, a slight fuselage taper and nose cone were added in OpenVSP to make the plane look more appropriate and generate a working aerodynamic model, this nose cone was sized manually and was 7 feet in length. A rough landing gear model was also added in OpenVSP and allowed for height measurements as well, landing gear was assumed to contribute minimally to center of gravity and was not included in mathematical analysis. This information is included in Table 6.

Section B, Tail

The tail section was only constrained by the 15° tail strike military criteria for landing gear. This constraint became the slope of the cone, assuming the landing gear would be located somewhere near the end of the main fuselage. The cone was further constrained to have a diameter equal to that of the main fuselage. The only weighted component in this section's calculations was that of the empennage, which was approximated in the TOGW analysis. The empennage was validated using an empennage area to wing area ratio of 0.3 as described by Nicolai, our ratio was slightly higher than ideal, but was still usable. Approximations for empennage weight are based around an empirical relationship between weight and the area of the horizontal and vertical tails [11]. The relevant empennage parameters are given in Table 5:

Parameter	Value
Vertical Tail Area	21.24 ft ²
Horizontal Tail Area	49.88 ft ²
Total Empennage Area	71.11 ft ²
Total Wing Area	218.5 ft ²
Ratio of Empennage and Wing Areas	0.325
Estimated Empennage Weight	78.23 ft ²

Table 5: Initial Section C Component Parameters

Table 6: Initial Fuselage Sizing Summary of Relevant Parameters

Section	Component	Location (From Nose to Front of Component) (ft)	Length (ft)
A	Nose Cone	0	6.98
	Engine	6.98	6.00
	Cockpit	12.98	8.33
	Fuel Tanks	21.31	9.07
	Electronics	30.38	3.42
	Entire Section	0	33.8
B	Entire Section	33.8	8.71
A, B	Entire Fuselage	0	42.51
A, B	Optimal Fuselage (Ideal L/D Ratio of 8)	0	37.34

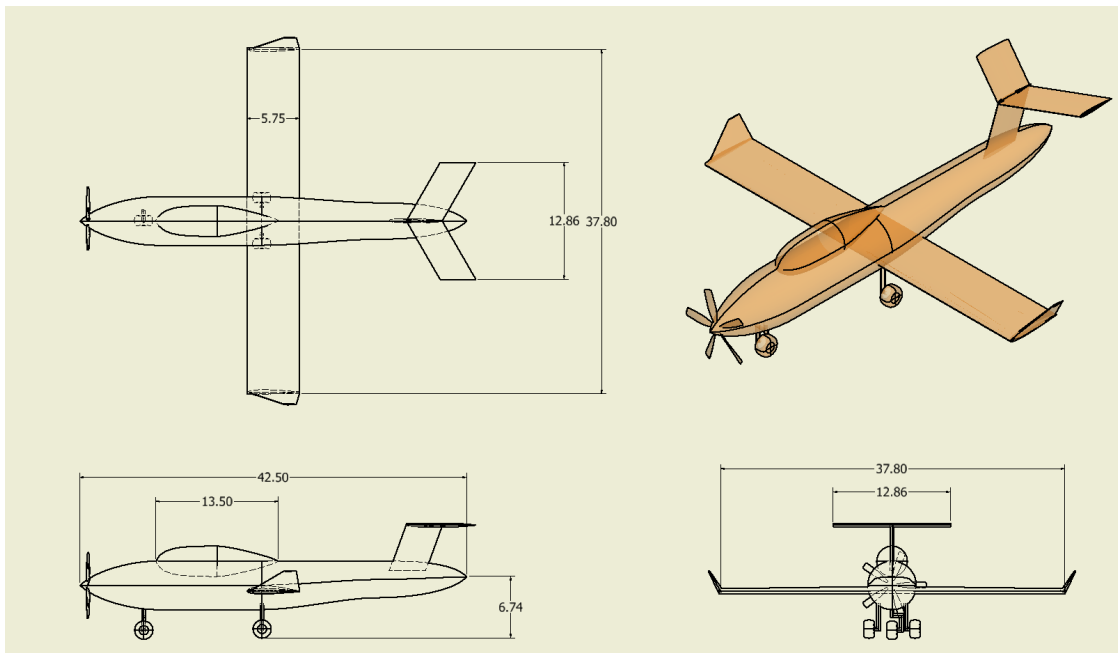


Figure 6: Isometric View of Initial Aircraft In Solidworks

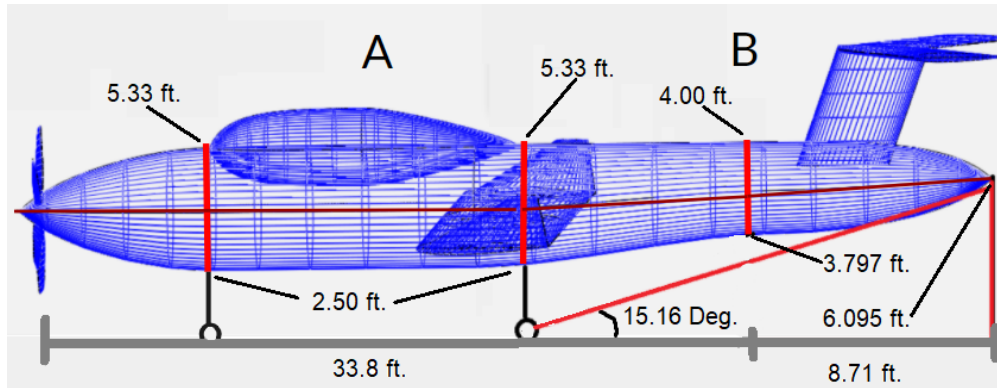


Figure 7: Dimensioned Side View of Initial Aircraft In OpenVSP, Sections A and B Shown

VII Configuration

VII.1 Concept Down Select

VII.2 Configuration Iteration

VII.3 Initial Configuration

VII.4 Fuselage

Since the initial model was slightly longer than the optimal fuselage length, variations in diameter and length were performed to quantify their impact on aircraft stability and weight distribution. With the initially included components we found the absolute smallest aircraft we could feasibly design would be 34.112 feet long, however it was determined that reducing the length of the aircraft, for our given empennage design, was not advantageous for aircraft control, so the total fuselage length of 42.51 feet was maintained throughout the final design iterations. Rather, it was deemed more feasible to increase the diameter of the plane by 1 foot. This allowed us to achieve a closer to optimal length and gain additional internal volume. This further allowed us to contour and shape the fuselage to increase aesthetic appeal, reduce weight, and increase aerodynamics. This increase in diameter also allowed for shorter, wider fuel tanks and significantly decreased the variation in center of gravity seen throughout the aircraft's flight. The next major change to the initial model was that of a titanium tub surrounding the pilots and cockpit, this was a consideration for aircraft and passenger survivability. The tank weight is shown in Table 7. This significant weight addition moved the center of gravity forward, drastically impacting the aircraft's weight distribution. To counteract this, the main weapon, the .50 caliber machine gun, which is discussed in the armament section, was added to the tail section of the fuselage. This

machine gun, the associated mount, and ammunition would be used to offset the weight of the titanium tub. This was deemed feasible with use of a gun camera in the electronic components. Ultimately these additions allowed the center of gravity to remain central with great improvements to aircraft survivability and function.

Table 7: Final Fuselage Sizing Complete Table of Weights and Dimensions

Component	Total Weight (lb)	Component Length (ft)	Component Diameter/ Width (ft)	Approximated Shape
Pilot (2)	360	N/A	N/A	N/A
Titanium Shielding	1102.31	N/A	N/A	N/A
Cockpit Furnishings (Including Ejection Seat)	895.97	8.33	5.33	Square Prism
JP-4 Fuel (Maximum Volume)	3402	9.07	5.33	Half - Cylinder
JP-4 Fuel (Minimum Volume)	170.1	N/A	N/A	N/A
Flight and Survivability Electronics	1633.5	10.76	1x 2.11 1x 1.82	Two Square Prisms
PT-6A Turboprop Engine	598	6.00	3	Cylinder
Empennage	78.23	N/A	N/A	Point Mass
Rear Mounted Machine Gun (Including Mount)	140.50	5.508	0.583	Square Prism
Ammunition (200)	771.618	N/A	N/A	N/A

Next a final list of electronic components was compiled. The total weight remained the same as the approximate weight generated in the initial design, however the individual electronics were packaged in a manner that allowed for ease of access for maintenance, described as “chest height and one deep” [3]. The electronics were approximated as cubes, laid out along both sides to reduce consumed fuselage length and placed relative to each other to ensure an even weight distribution. Electronics are shown in Table 8. One later adjustment that was made was the addition of more fuel. Similar to the initial fuselage sizing assessment, maximum fuel weight was given, this time by mission profile analysis in FLOPS, then fuel volume, required fuel tank volume, and the required length of the half cylinder fuel tank were calculated using the same methods as discussed previously. There was 600 lb increase in fuel capacity, but due to the added diameter of the fuselage, there was not a significant increase in fuel tank length nor was there a large variation in center of gravity. Lastly, the empennage underwent significant modifications throughout the iterative design process, empennage design, specifically its size, seemed dependent on the aircraft’s center of gravity, which varied minimally throughout the fuselage design process. The most notable change in empennage design was that the horizontal tail design was modified by removing the initial sweep. Ultimately, the total area of the empennage did not change significantly. And the area based weight assessment was relatively constant.

Payload

Requirements:

Table 8: Final Fuselage Sizing Electronics

Side	Component	Weight (lb)	Side Length (ft)	Location (Measured From Nose To Front of Component) (ft)
Left	Lead Computing Optical Sight	5	0.496	0
	UHF DF Horning	5	0.496	0.496
	Range Only Radar	25	0.848	0.992
	Autopilot System	168.5	1.603	1.84
	Inertial Navigation System	207	1.717	3.443
	Terrain Following Radar	249	1.826	5.16
	TACAN	61	1.142	6.986
	UHF Communications	51	1.076	8.128
	Head-up Display	37	0.967	9.204
	Gyrocompass	8.4	0.590	10.171
Right	Gun Camera	2	0.365	0
	Air Data Computer	14	0.699	0.365
	Flight Data Recorder	15.6	0.725	1.064
	Intercom System	19.2	0.777	1.789
	Attack Radar	387.2	2.11	2.566
	Radar Warning and Horning	182	1.645	4.676
	High Frequency Radio	78.4	1.242	6.321
	Air-To-Ground IFF	53	1.090	7.563
	Radar Altimeter	38.2	0.977	8.653
Both	ILS-VOR	27	0.870	9.63
Both	All Electronics	1633.5	N/A	10.766

Table 9: Fuselage Sizing Summary of Relevant Parameters

Section	Component	Location (From Nose to Front of Component) (ft)	Length (ft)
A	Engine	3.002	6.00
	Cockpit	10.170	8.33
	Fuel Tanks	18.516	8.358
	Entire Section	0	22.695
B	Electronics	28.596	10.767
	Gun and Ammunition	25.449	5.508
	Entire Section	22.695	19.955
A, B	Entire Fuselage	0	42.51
A, B	Optimal Fuselage (Ideal L/D Ratio of 8)	0	42.64

Table 10: Initial Fuselage Sizing Additional Design Information

Parameter	Value
Fuselage Diameter	5.331 ft
Fuselage length	42.51 ft
Total Internal Component Weight	8982.124 lb
Center of Gravity (Measured From Nose)	18.024 ft
Variation In Center of Gravity (Maximum Fuel to Minimum Fuel)	+0.276 ft (Forward)

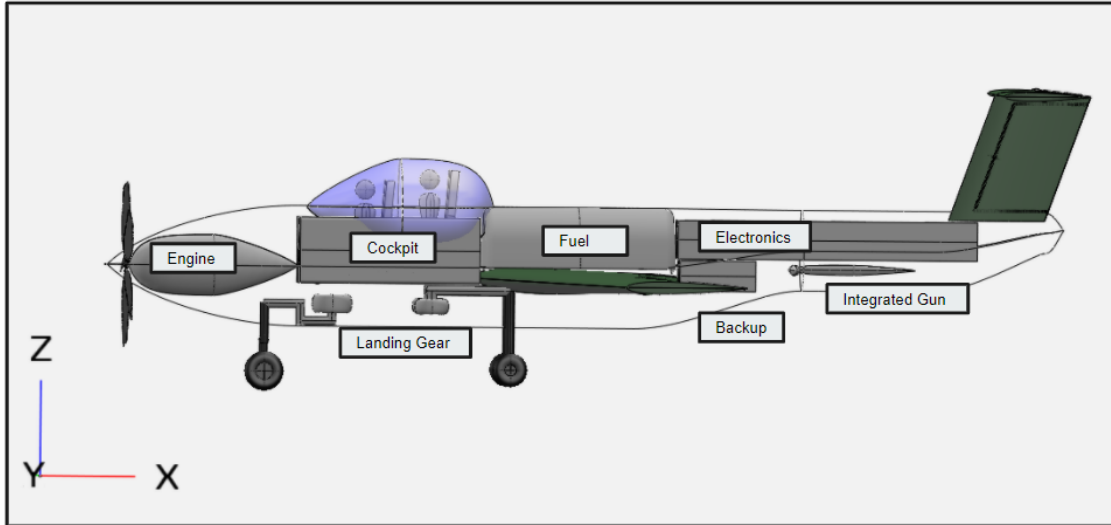


Figure 8: Cross-Section Side View of Final Aircraft In OpenVSP, Major Components Shown

- Our aircraft payload has been designed to satisfy the following objectives: 3000 lbs of payload and armament
- Provisions for carrying/deploying a variety of weapons, including rail-launched missiles, rockets, and 500 lb (maximum) bombs
- Integrated gun for ground targets

Wing Mounted Armaments

To meet the payload requirements, our design utilizes six wing hardpoints that will carry the following armament tabulated in Table 11:

Table 11: Default Armaments List

Name	Weight	Description
Mark 82 Bomb	2 x 500 lbs	Unguided, general purpose bomb
AGM-65K Maverick	2 x 790 lbs	Air-to-ground, high penetration missile
AIM-9X Sidewinder	2 x 190 lbs	Air-to-air missile
Total Payload	2960 lbs	Not including side-mounted .50-cal cannon and ammunition

The Mark 82 bomb is a general-purpose, unguided aircraft bomb that contains 89kg of explosives. The Mark 82 was developed in 1940 and remains in service today [19]. Including one of these bombs would satisfy the RFP, however our design incorporates two in order to balance each other on the aircraft wings and provide more bombing capability. In addition to the pair of Mark 82 bombs, two AGM-65K Maverick missiles provide additional ground-targeting capabilities. The Maverick family of missiles are a proven series of air-to-ground guided weapons that are valuable against a variety of targets, including air defences, ships, heavy armor, and ground equipment. These missiles are still being used by aircraft such as the A-10 and F-15E [20]. We chose to use the K variant for two reasons. First, the K

variant is a modern version of the AGM-65 that utilizes a heavyweight penetrator warhead, which will provide our aircraft with more offensive capability than using the standard H variant [21]. Second, the increased weight-per-missile allows our aircraft to carry fewer missiles to meet payload specification, which reduces drag and improves aerodynamic performance. Rounding out the default payload is a pair of AIM-9X Sidewinder air-to-air missiles. The AIM-9X is the latest variant of the popular Sidewinder missile platform, currently produced by Raytheon and utilized by aircraft such as the F/A-18, F-22, and the F-35 [22]. These missiles help our design combat aerial threats to the aircraft or the friendly forces on the ground, such as attack jets and helicopters. We have considered other configurations that could be substituted with the default configuration, depending on the needs for a given mission. Aside from using other variants or combinations of the armaments from the default payload, such as using the AGM-65H or mounting more bombs instead of missiles, our design also would support the M134D-H, which is a self-contained mini-gun pod designed by Dillon Aero that weighs 350 lbs each [23]. Using these mini-gun pods, in addition to the side-mounted cannon, would increase the sustained damage output of our craft at the expense of powerful, one-time-use weaponry.

Internal Gun

In order to incorporate an internal gun, we chose a side-mounted FN MP3 .50-caliber cannon in the rear of our aircraft. The FN MP3 is an 80.5lb machine gun that is designed for aircraft and advertises offensive and defensive power at nearly 1,850 meters [24]. Since our aircraft fuselage is relatively small and cramped in the nose, we decided not to fit a forward-facing cannon, such as those seen in other attack aircraft like the A10 or A-29. Instead, we drew inspiration from the AC130's side-mounted arsenal of 25mm, 40mm, and 105mm munitions [25]. A side-mounted cannon allows our design to strafe the combat site and provide sustained coverage, while also allowing the aircraft to stow away the cannon when not in use to improve aerodynamics.

VIII Aerodynamics

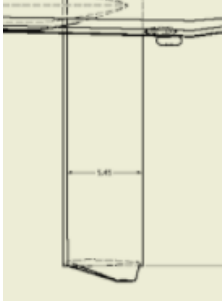


VIII.1 About VSPAERO

VSPAERO is a vortice lattice solver developed by David Kinney at NASA that is integrated with OpenVSP. VSPAERO applies discrete vortices to the degenerate geometry generated by OpenVSP in order to obtain a pressure distribution that can be used to find lift, drag, slip, and the (x,y,z) forces and moments. In addition to freestream and flight conditions, the solver also includes capabilities to analyze propellers using actuator disks [26]. For our design process, we initially utilized VSPAERO propeller analysis to determine aerodynamic parameters before transitioning to free stream conditions due to the improved run-time performance and ease of use.

VIII.2 Initial Wing Design

Our initial wing was rectangular in shape with an area of 218.5 ft² and a wingspan of 38 ft. For the airfoil, we chose the NACA 63A-415[27]. These starting values were developed based on comparisons made against other state-of-the-art attack aircraft, such as the A-10 and A-29, and were also utilized in the derivation of the take off gross weight. Both of these aircraft have straightforward, and rectangular wing designs. Table 12 contains comparisons between their dimensions and that of our initial wing. Our initial design's sizing is roughly between that of the A-10 and A-29, which is reflected by the design parameter comparison.

Table 12: Comparison of Wing Design Parameters Between Initial Design and State-of-the-Art

	Initial Design	A-29 [28]	A-10 [29]
Wing Area (ft ²)	218.5	209	506
Wingspan (ft)	38	37.17	57.5
Airfoil	NACA 64A-415	NACA 64A-415	NACA 6716
Fuselage Length	43.74	37.47	53.25
Wing Shape			

After implementing the initial design in OpenVSP, we performed a basic analysis of the aerodynamic performance of the design using VSPAERO. Using propeller analysis, we ran VSPAERO on angles of attack between 3° and 5° at a Mach of 0.3 in order to determine the peak L/D. We also adjusted the wing design to see how the airfoil, sweep angle, taper ratio, and inclusion of winglets impacted L/D max. Figures 9 and 10 summarize the results of these propeller-based simulations.



Wing Analysis



Config	Best AOA	Mach	L/D	CL	CDo
NACA 64A415	4	0.3	12.189	0.499	0.0254
NACA 64A215	5	0.3	11.728	0.534	0.0262
NACA 2412	4	0.3	11.964	0.461	0.0252
NACA 2415	4	0.3	11.848	0.461	0.0257
10° Sweep	4	0.3	12.222	0.497	0.0260
20° Sweep	5	0.3	12.337	0.573	0.0265
0.8 Taper	4	0.3	11.834	0.506	0.0252
0.6 Taper	5	0.3	11.501	0.635	0.0268

Figure 9: Comparison of L/D by Configuration of the Initial Wing Design

Config	AOA	Mach	L/D	CL	CDo
Winglets	4	0.3	12.189	0.499	0.0254
No Winglets	4	0.3	11.629	0.474	0.0250

Figure 10: L/D Comparison With and Without Winglets

As shown in the chart, the straight-winged design with the NACA 64A415 had a higher L/D than designs with no winglets, other airfoils, and taper ratios less than one. However, increasing the sweep angle led to a minor increase in L/D over the default design. Ultimately, we chose to use the rectangular wing with no sweep for our initial design, since the wings would be simpler to manufacture and lighter, which would improve the cost of the aircraft without majorly impacting L/D.

VIII.3 Increasing L/D

A significant increase in the fidelity of our initial model's fuselage and armament caused a large increase in the total drag of the aircraft, resulting in a need to increase the L/D produced by the wing design. In order to achieve this, we maintained a constant aspect ratio of 6.6 and introduced a sweep of 15° and increased the area and wingspan to 278.85 ft² and 42.9 ft, respectively. We also introduced a taper ratio of 0.7 to reduce the weight and improve structural stability

of the larger wing. Finally, we introduced an incidence of 5° to the wing, which helped reduce the angle of max L/D that had increased due to the previous changes. Figure 11 shows the wing design with these modifications.

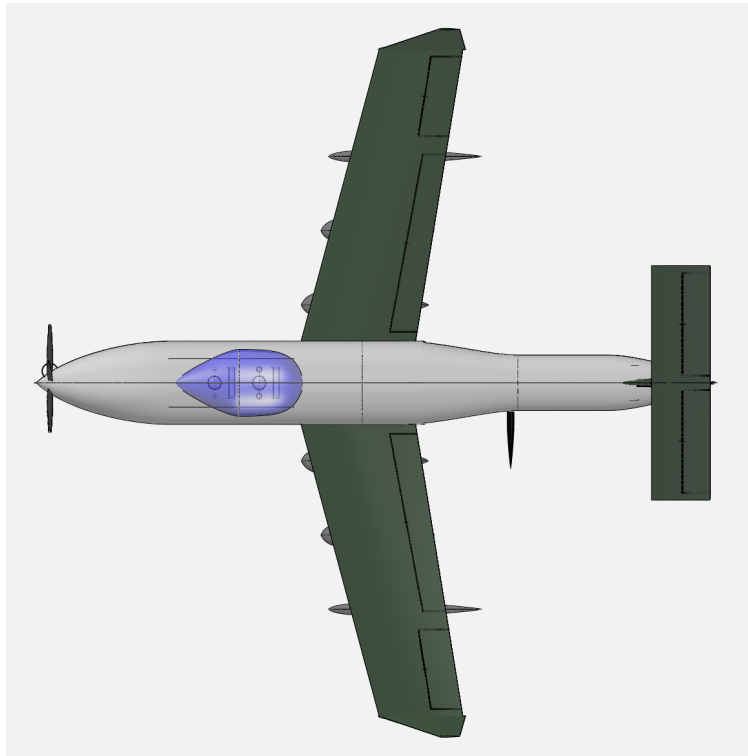


Figure 11: Revised Wing Design Including: Area Increase, Sweep, Taper, and Incidence

In order to perform a more in-depth aerodynamic analysis using VSPAERO, we chose to use a free stream analysis. This allowed the simulation to automatically iterate between a wide range of angles of attack without having to restart the simulation for each one, which was a limitation of the propeller analysis. We performed the simulation between -6° to 20° . This resulted in a max L/D of 11.7 at an angle of attack of 6° , which was in line with what was necessary based on our performance analysis. The plots of L/D, CL, and $CD_{0, i, tot}$ are shown in Figure 12.

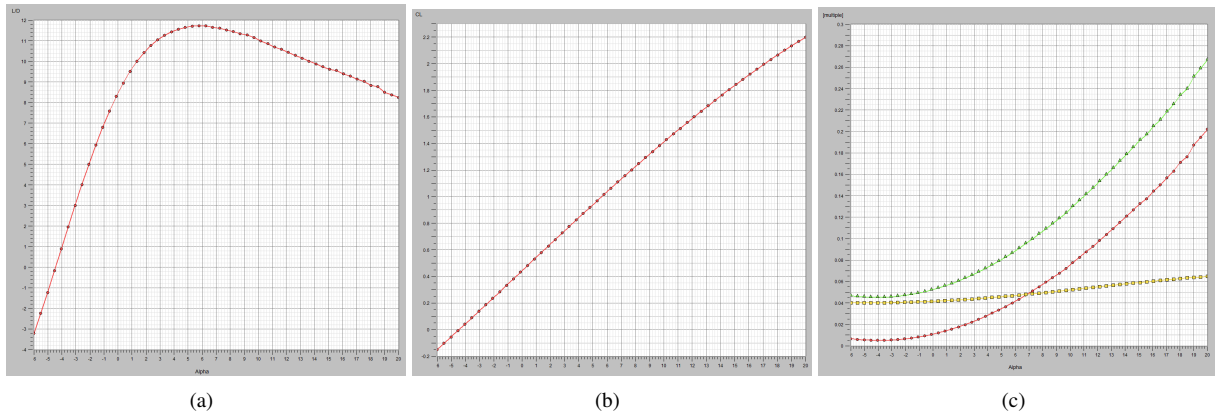


Figure 12: For -6° to 20° AoA: (a) L/D (b) C_L (c) C_D

Increasing Stability The free stream VSPAERO analysis revealed a pitch moment CM_y less than 0 for zero angle of attack, which is a sign of vertical instability. In order to combat the instability and increase CM_y to be positive at a zero-angle of attack, a dihedral angle of 2° was introduced. The empennage sizing was also increased (see Empennage section for more details).

VIII.4 Final Wing Aerodynamics

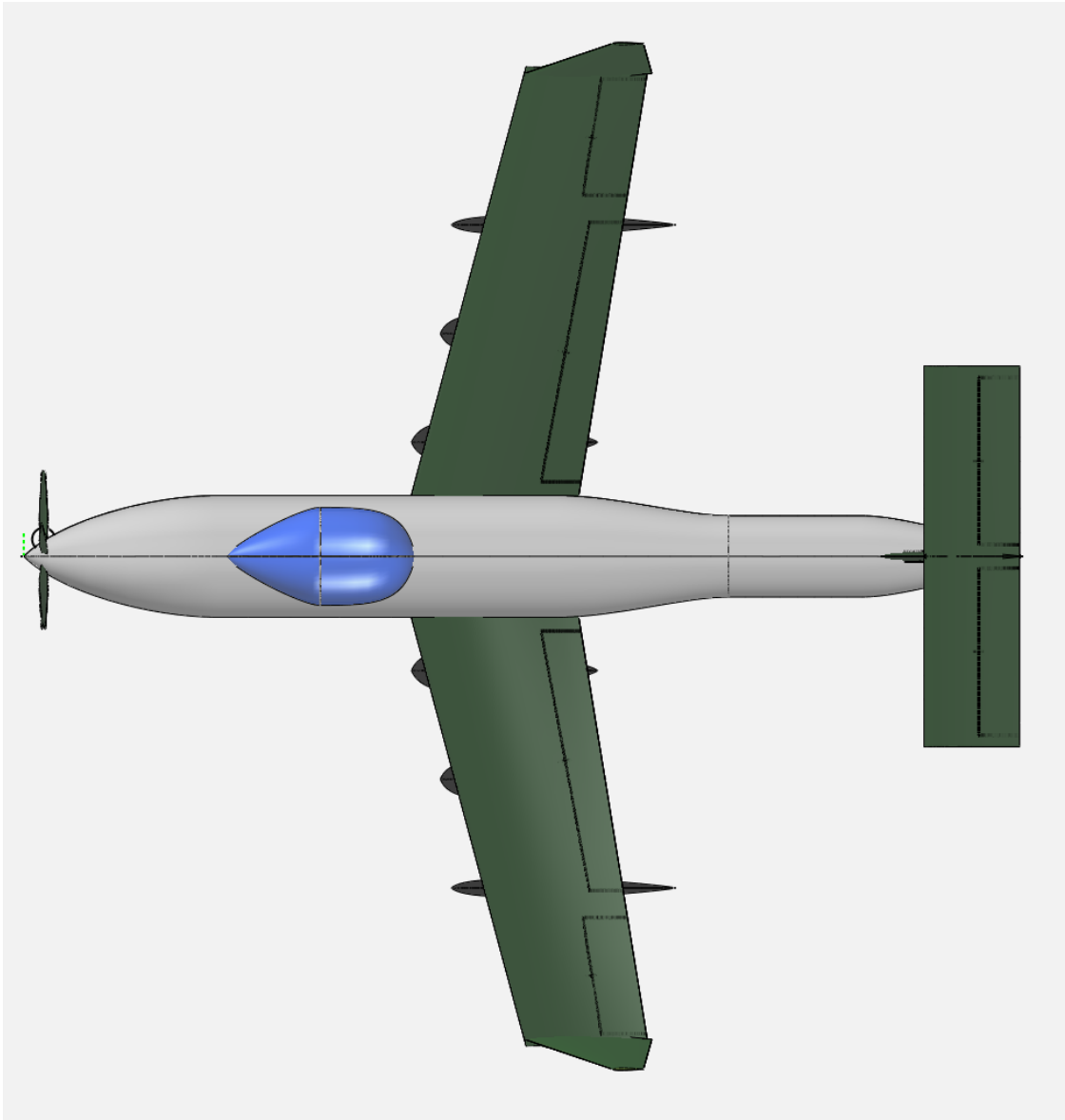


Figure 13: Final Wing Design

Figure 13 depicts our final wing design, including the resized empennage and slight dihedral angle. With this design, we ran a detailed VSPAERO simulation from -6° to 20° with half-degree precision. The plots resemble those of Figure 12 from the previous simulation, with a final L/D Max of 11.3 at 6° and a positive pitch moment for zero angle of attack. Additionally, a stability analysis was performed using the built-in methods in VSPAERO, which produced an approximate summary of stability derivatives and moments as depicted in Figure 14. We are confident that our wing design provides the aircraft with the means to affordably and effectively control the skies.

```

-----
# Name      Value      Units
Sref_      278.8500000 Lunit^2
Cref_      6.5000000 Lunit
Bref_      42.9000000 Lunit
Xcg_       20.0712290 Lunit
Ycg_       -0.0000000 Lunit
Zcg_       0.4014530 Lunit
Mach_      0.3000000 no_unit
AoA_       0.0000000 deg
Beta_      0.0000000 deg
Rho_       0.0023770 Munit/Lunit^3
Vinf_      293.8000000 Lunit/Tunit
Roll_Rate  0.0000000 rad/Tunit
Pitch_Rate 0.0000000 rad/Tunit
Yaw__Rate  0.0000000 rad/Tunit

# Case      Delta  Units  CFx  CFy  CFz  CMx  CMy  CMz  CL  CD  CS  CML  CMn  CMn
#
Base_Aero  +0.000 n/a  0.0041607 -0.0000000 0.3906736 0.0000000 0.0232089 -0.0000000 0.3906736 0.0085212 -0.0000000 -0.0000000 0.0232089 0.0000000
Alpha      +1.000 deg -0.0029705 -0.0000001 0.4823283 -0.0000000 -0.0080625 0.0000000 0.4823066 0.0111994 -0.0000001 0.0000000 -0.0080625 -0.0000000
Beta       +1.000 deg 0.0035901 -0.0081431 0.3905413 0.0033719 0.0224971 -0.0012227 0.3905413 0.0085895 -0.0080792 -0.0033719 0.0224971 0.0012227
Roll_Rate  +1.000 rad/Tunit -0.0019584 -0.0184115 0.3870835 0.0440463 0.0238864 -0.0003263 0.3870835 0.0102495 -0.0184115 -0.0440463 0.0238864 0.0003263
Pitch_Rate +1.000 rad/Tunit 0.0025701 0.0000001 0.5246223 0.0000000 -0.2082294 -0.0000000 0.5246223 0.0123512 0.0000001 -0.0000000 -0.2082294 0.0000000
Yaw__Rate +1.000 rad/Tunit -0.0022255 0.0370359 0.3908150 -0.0117059 0.0216540 0.0154551 0.3908150 0.0093549 0.0370359 0.0117059 0.0216540 -0.0154551
Mach       +0.100 no_unit 0.0042600 -0.0000000 0.4013810 0.0000000 0.0245141 -0.0000000 0.4013810 0.0089456 -0.0000000 -0.0000000 0.0245141 0.0000000

#
# Base Derivative:
# Aero wrt wrt wrt wrt wrt wrt wrt
# Coef Total Alpha Beta p q r Mach U
# - per per per per per per M per
# - rad rad rad rad rad rad rad u
#
CFx 0.0041607 -0.4085862 -0.0326910 -0.0838120 -0.1437822 -0.0874704 0.0009937 0.0002981
CFy -0.0000000 -0.0000044 -0.4665649 -0.2521809 0.0000132 0.5072801 -0.0000001 -0.0000000
CFz 0.3906736 5.2514266 -0.0075819 -0.0491741 12.1089643 0.0019474 0.1070740 0.0321222
CMx 0.0000000 -0.0000004 0.1931931 0.6033008 -0.0000000 -0.1603360 -0.0000000 -0.0000000
CMy 0.0232089 -1.7917241 -0.0407831 0.0092796 -20.9220248 -0.0212980 0.0130519 0.0039156
CMz -0.0000000 0.0000013 -0.0700567 -0.0044699 -0.0000013 0.2129210 -0.0000000 -0.0000000
CL 0.3906736 5.2514266 -0.0075819 -0.0491741 12.1089643 0.0019474 0.1070740 0.0321222
CD 0.0085212 0.1534466 0.0039140 0.0236724 0.3462320 0.0114185 0.0042439 0.0012732
CS -0.0000000 -0.0000044 -0.4629039 -0.2521809 0.0000132 0.5072801 -0.0000001 -0.0000000
CML 0.0000000 0.0000004 -0.1931931 -0.6033008 0.0000000 0.1603360 0.0000000 0.0000000
CMn 0.0232089 -1.7917241 -0.0407831 0.0092796 -20.9220248 -0.0212980 0.0130519 0.0039156
CMn 0.0000000 -0.0000013 0.0700567 0.0044699 0.0000013 -0.2129210 0.0000000 0.0000000

#
# Result Value Units
SM 0.3412686 no_unit
X_np 22.2894747 Lunit
#
#

```

Figure 14: Output of the VSPAERO Stability Analysis

IX Stability and Control

IX.1 Tail Sizing

The tail of the aircraft was sized according to Nicolai's method [3]. The moment arms of the vertical and horizontal tail were sized in three different iterations. The first, and very rough, iteration utilized center of gravity estimates from the A-29 calculated by taking relative measurements from a photograph of the aircraft. We assumed that the center of gravity of the aircraft was near the back middle of the wing. This resulted in an lvt of 19.2 ft and an lvt of 18.9 ft. The second iteration utilized the calculated center of gravity of our aircraft and assumed the tail to be at the end of the fuselage, resulting in moment arms of lvt = 18.8 ft and lvt = 19.2 ft. Finally, we utilized Raymer's method of equating lvt and lvt to 55% of the total fuselage length [30]. This created significantly longer moment arms of 23.5 ft.

To continue Nicolai's tail sizing method, we selected tail volume coefficients from the Beechcraft T-34 single turboprop military trainer aircraft: 0.048 for vertical and 0.76 for horizontal. This allowed me to calculate the area of the vertical and horizontal tails. With an earlier fuselage length of 33.7 ft, the areas were 21 ft² and 50 ft², respectively. These increased to 23 ft² and 57 ft² with a 44.3 ft fuselage. With a final fuselage length of 43 ft, we wanted to increase longitudinal stability, so we increased the horizontal tail volume coefficient to 0.9 (which will be discussed further in

this section), resulting in a vertical tail area of 24.5 ft² and horizontal tail area of 69.5 ft².

The T-tail design was chosen during an early trade study on our aircraft with information from Raymer's textbook. This orientation was chosen to increase the effectiveness and efficiency of the horizontal tail, as well as allowing it to be clear of wing wake and propwash. While the T-tail is not suitable for all flight regimes, our cruise and maximum Mach values were expected to be well within the suitable regime for the T-tail design.

Aspect ratios, taper, and sweep for the vertical and horizontal tails were selected by literature from the Indian Institute of Technology [31]. Lower aspect ratios for the tail than the wing were selected in order to reduce structural weight. Professor Tulapurkara details that minimizing drag from the tail should not be prioritized above reduction of structural weight, and thus cost, so a lower aspect ratio is preferable. The aspect ratios for the vertical and horizontal tails selected are, respectively, 1.3 and 4. Taper ratio was selected based on minimizing cost, so both tails used a value of 1. Finally, the sweep of the vertical tail was selected as 20° in order to increase the moment arms of the vertical and horizontal (via the T-tail design) tails for a low/medium Mach number. The sweep of the horizontal tail was left at 0° as an increased sweep to decrease drag divergence Mach was unnecessary at our low/medium Mach flight.

IX.2 Static Margin, Stability Derivatives, Control Surfaces

The static margin was calculated using Nicolai's equations. A plot of coefficient of lift over angle of attack was first created using Flightstream aerodynamics analysis of just the wing and tail separately. This resulted in a static margin of around 6% of the chord length, calculated via Nicolai's method. We then turned to VSPAero which allowed us to run aerodynamics analyses of the entire aircraft. After one failed attempt that resulted in a negative margin, we found success when analyzing the updated aircraft design including pods. With an aircraft center of gravity at around 16 ft, the static margin was quite small at only 3%, again using Nicolai's method. The center of gravity was then pushed further back to around 18 ft, which resulted in a suitable static margin of just under 5%. This value changed one final time with a change in horizontal tail size, resulting in a static margin of 4.2%. This value was in the range that we had hoped for to provide stability for the aircraft.

Directional stability was calculated at the same time as the static margin using VSPAero. Between the two subsequent analyses, the change in coefficient of pitching moment with respect to angle of attack, $C_{m,\alpha}$ moved more negative, thus showing a greater restoring moment and greater stability. However, both of these trials struggled as the coefficient of pitching moment at zero lift, $C_{m,0}$ was a negative value, meaning that there was no positive trim condition for the aircraft, which was unacceptable to our aircraft [32]. This instability was corrected by increasing the horizontal tail volume coefficient from 0.76 to 0.9. This succeeded in pushing the $C_{m,0}$ value positive to 0.035. This also resulted in a new C_m , value of $-0.03 / ^\circ$ ($-1.8 / \text{rad}$), the negative value of which signals stability. Therefore, the positive $C_{m,0}$ and negative C_m , show directional stability of our aircraft.

Lateral stability was calculated using VSPaero simulations. Unfortunately, $C_{l,\beta}$ the derivative of the rolling moment coefficient with respect to side-slip angle β was found to be positive for our aircraft with a value of $0.003 /^\circ$ ($0.19 /\text{rad}$). Lateral stability is achieved with a negative $C_{l,\beta}$. While we did not have time to correct this stability concern, this would be a primary focus of future work. This lateral instability could be solved by increasing the sweep of the wings; our current wings are swept only 15° , so there is room to increase this sweep in future improvement [33]. We could also seek to utilize a greater dihedral angle than our current 2° in our wings to increase lateral stability. The current $C_{l,\beta}$, of $0.003 /^\circ$ is a small enough value that we are confident that this could be moved negative with only a few alterations to the design.

Directional stability was also calculated using VSPaero simulations. $C_{n,\beta}$ the derivative of the yawing moment coefficient with respect to side-slip angle, was calculated as $-0.0012 /^\circ$ ($-0.07 /\text{rad}$). This number is negative, yet should be positive for directional stability. This value could be moved positive by increasing the size of the vertical tail, just as the horizontal tail area was increased to create a positive $C_{m,0}$ for longitudinal stability. This could also be improved by increasing the sweep of the wings. A larger sweep angle could improve both the directional and lateral stability, so would be a first step in future work on this design. The $C_{n,\beta}$ of $-0.0012 /^\circ$ has a very small magnitude far smaller than that of the beneficial longitudinal stability derivative, so the team is again confident that directional stability could be achieved with only minimal alterations this design.

The three control surfaces were sized using Roskam's method of area ratios[11]. We selected the Embraer EMB-312 Tucano as a similar aircraft driven by a single propeller. The ailerons were sized to be 10% of the area of the wing, resulting in an aileron area of 28 ft^2 . The elevator was 44% of the horizontal tail area, resulting in an elevator area of around 31 ft^2 . Finally, the rudder was a significantly large 70% of the vertical tail area, resulting in a rudder area of 17 ft^2 .

An additional control surface was added via a trim tab at the aft of the elevator on the horizontal tail. This was sized as 5% of the elevator area, resulting in a trim tab area of 1.5 ft^2 . This will be a pilot-controlled variable trim tab to allow for changed settings during take off, cruise, and landing.

X Propulsion

X.1 Engine Selection Process

The first objective for the propulsion development portion of the project was to select a usable engine platform for the aircraft. The mission requirements and weight/size descriptions of the aircraft in the RFP were the main criteria used in initially selecting an engine type and class. Given the constraint of only allowing engine technologies that are able to

be realistically developed by 2025, initial research was done on both engine design and potential future improvements.

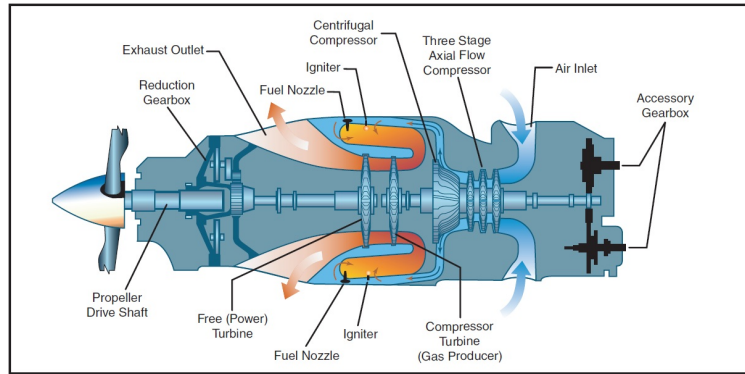


Figure 15: Reverse Flow Turboprop [1]

First, for military aircraft, a common method of propulsion is a turboprop engine. Turboprop engines have an inlet, compressor, burner, and turbine which work to provide shaft power to the propeller in order to produce thrust. Thrust is created both from the propellers, which converts the mechanical shaft power supplied by the turbine to usable thrust, and the engine core, which is a function of the freestream and exit velocities as well as the air and fuel mass flow rates through the engine. For a turboprop specifically, figures of merit exist to quantify the engine's efficiency such as the propeller efficiency and the gearbox efficiency. More generally, turboprop engines also have thermal efficiency η_{th} and propulsive efficiency η_p , which quantify the thermodynamic losses in the engine. For a turboprop, the attractiveness of the engine lies in its high propulsive efficiency [2]. Turboprop engines are found in a variety of both military and civilian aircraft. For military use, both the EMB-314/A-29 Super Tucano and the AT-6 Wolverine are powered by turboprop engines, two aircraft studied as capable existing options for the design mission.

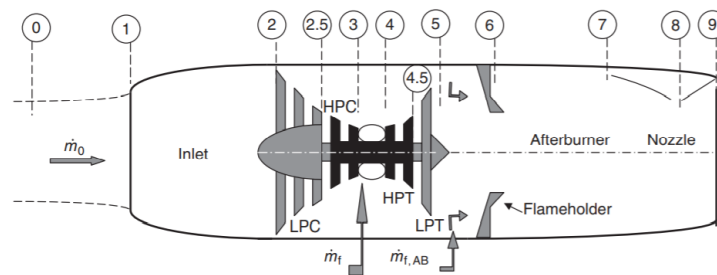


Figure 16: Afterburning Turbojet Engine Schematic [2]

Another usable engine type is the turbojet, shown above. Looking at modern military aircraft, one can see that turbojets have been steadily phased out of use in modern aircraft design, being replaced almost entirely by either turbofan engines (discussed later) or lower-speed turboprop engines where appropriate. While turbojets do still see use as missile propulsion systems, it cannot be overlooked how by most modern standards for aircraft, there is no

satisfactory justification to run a turbojet engine over a comparable turbofan, with the lone exception perhaps being the relative simplicity of a turbojet relative to a turbofan.

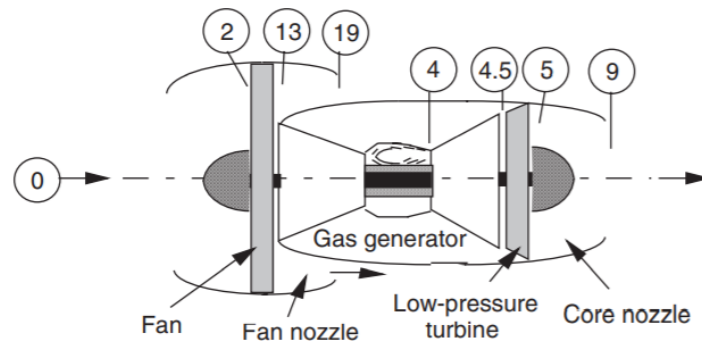


Figure 17: Separate Exhaust Turbofan Engine Schematic [2]

Another type of aircraft engine commonly employed today, both in civilian and military applications, is the turbofan engine. As the name implies, the turbofan was developed to reach a middle ground between the previous two engine types, combining the higher efficiencies of turboprop engines with the superior thrust capabilities of turbojet engines. A turbofan is broadly divided into two sections: the core and the fan. The core of a turbofan is functionally identical to a standard turbojet engine. Free stream air enters the engine through an inlet, passing through a compressor or series of compressors before mixing with fuel and igniting in the combustion chamber. This heated air then passes through the turbine, which extracts power to run the compressor and fan, before being expelled out a nozzle to propel the aircraft forward. Where a turbofan differs from a turbojet centers on the fan at the front of the engine. As shown below, not all the air that passes through the fan enters the core of the engine, and some of it bypasses the engine core entirely. For the air that does not enter the core, the engine functions similarly to a standard propeller. This air is slightly accelerated as it passes through the fan, and generates additional thrust alongside the core turbojet component. This improved thrust output comes with nearly no significant additional fuel flow rate relative to the core alone, making a turbofan more fuel efficient than a traditional turbojet [1].

As this high-level breakdown has demonstrated, each classification of propulsion system brings its own advantages and downsides to the discussion. One must consider a variety of factors, including thrust output, weight, fuel efficiency, and flight envelope, in order to make an informed decision on what general propulsion system is the most ideal for a given aircraft design. From the RFP, it is known that the light attack aircraft must have a service ceiling of at least 30,000 feet, while in preliminary analysis, it was derived that the aircraft should have a cruise capability of about 300 knots at a minimum. Plotting these two parameters on the graph below, it is clear that a piston-prop engine does not meet these minimum requirements. Therefore, the best starting point for a propulsion system is likely a turboprop engine of some variety. While a turbofan may also be worth investigating, there is valid concern that most turbofans

may be overqualified for the given mission requirements. There can be such a thing as having too much thrust, and when looking at cost-effectiveness and overall weight gains from using a turbofan over a turboprop, the trade-offs for integrating a turbofan propulsion system begin to become concerning relative to the gains.

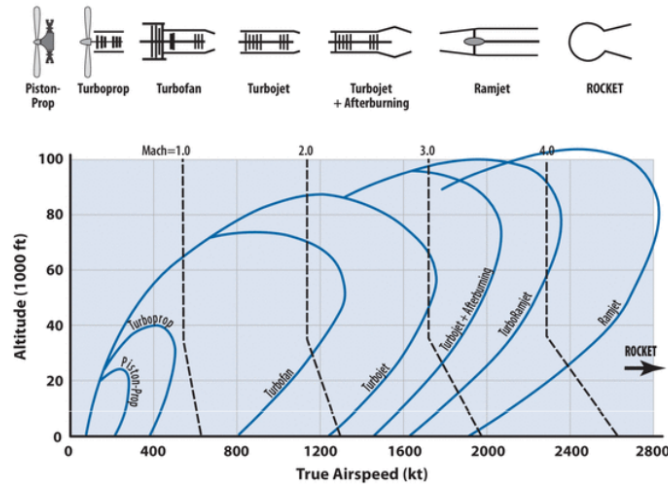


Figure 4.6 Level-flight propulsion options.

Figure 18: Service Regions for Various Propulsion Systems [3]

Given the requirements of the RFP, and the nature of the austere light attack aircraft being designed, the conclusion of our initial research is that a turboprop engine is the most appropriate form of propulsion. A turbofan could also be applicable, but the added weight is a major drawback as well as, given the low flight speeds of the attack aircraft's intended usage, the increased power may be unnecessary.

X.2 About GasTurb

GasTurb is a gas turbine cycle analysis software that can allow users to create gas turbine engine designs and off-designs, calculate engine's fluid dynamic parameters and performance, run parametric and Monte Carlo simulations for design optimization, model engine deterioration over time, do detailed stress analysis, and model engine performance(s) for various flight envelopes. The tool was designed by career aerospace performance engineer Dr. Joachim Kurzk with the company GasTurb GmbH in Aachen, Germany. GasTurb 13 will be used to help determine and optimize engine performance using known flight envelopes and engine size/weight estimations. The objective of GasTurb 13 analysis for this project is to obtain engine performance and efficiency values, predict fuel consumption, and get basic engine cycle information (such as temperature and pressure) to base future improvements off of. The model will be initially developed using known flight regimes, mainly altitude and mach number in combination with estimated engine parameters, such as size, burner temperatures, and spool speed.

X.3 Establishing an Initial Model

Since the Embraer EMB 314 Super Tucano, a comparable aircraft to our design, is powered using the Pratt Whitney PT-6A-68C turboprop engine, that was the engine used as a baseline for our analysis. The first objective of the GasTurb modelling was to recreate this engine design digitally. The Pratt Whitney PT-6A engine manual had a large quantity of data regarding engine performance, design, and operating conditions. The relevant data used in creating the PT-6A model will be given in successive paragraphs. The most significant information found in the engine manual was a total temperature and total pressure by engine stage graph. It should be noted that the Pratt Whitney graph shown below identifies engine stages at different numbers than the GasTurb program output. The following table was created to clarify this issue.

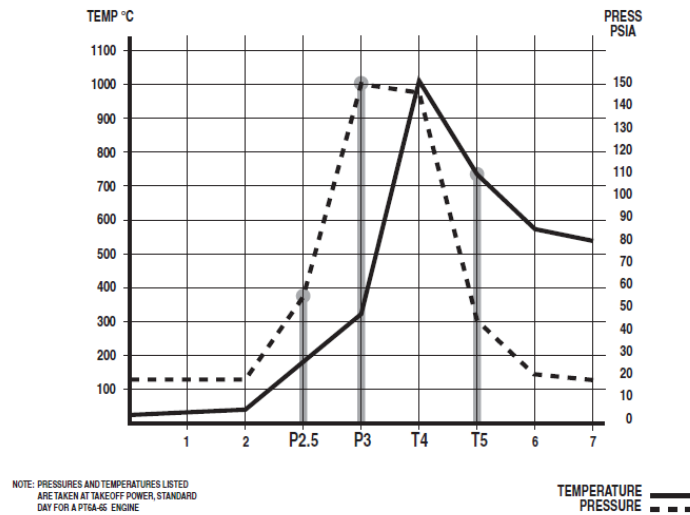


Figure 19: PT-6A Total Temperatures and Pressures By Engine Stage [4]

Table 13: Approximated Temperature & Pressure Values For PT-6A

#	Stage	Temperature (R)	Pressure (Psi)
0	Ambient	529.67	15
1	Air intake	539.67	15
2	Compressor inlet	581.67	15
3	Compressor exit	1059.67	150
4	Turbine inlet	2289.67	145
5	Interturbine	1839.67	40
6	Turbine exit	1526.67	20
7	Exhaust	1009.67	15

Some additional minor information was also extracted from the text. First, compressor compressor ratios were found, they were seen to vary by engine model and would range from 9.0 to 12.1, this value was extremely relevant to GasTurb as it is one of the main inputs. Tip-clearance of compressor and turbine blades was also given explicitly

as 0.010” which will be needed for more complex modelling. Propellor and spool rotational speeds were also given, 1500 RPM and 39000 RPM respectively. Lastly, a parametric graph relating air temperature, pressure, and engine performance was given, this is an additional resource to base the initial engine design off of. Ultimately, this document, the flight mission profile (mainly the aircraft speed and maximum/minimum altitude(s)), and knowledge of thermodynamic engine cycles was used to develop the first PT-6A GasTurb model [34].

X.4 Current PT6-A GasTurb 13 Model

GasTurb Analysis Inputs

The GasTurb model utilized to model the PT-6A was the “1-spool Turboprop” with the following properties shown in Table 14.

Table 14: PT-6A GasTurb Additional Input Values

Property:	Units:	Value:	Comments:
Ambient Conditions: Total Temperature	R	518.67	Default, sea level conditions
Ambient Conditions: Total Pressure	Psia	14.6959	Default, sea level conditions
Ambient Conditions: Ambient Pressure	Psia	14.6959	Default, sea level conditions
Ambient Conditions: Relative Humidity [%]	N/A	0	Default
Compressor Efficiency: Polytropic Efficiency	N/A	0.9	Within reasonable value
Compressor Design: Nominal Spool Speed	RPM	39000	Given from PT-6A manual
Turbine Efficiency: Polytropic Efficiency	N/A	0.9	Within reasonable values
Heat Exchanger (Method 1): Heat exchanger Design Eff.	N/A	0.85	Within reasonable values, adjusted to return correct outputs
Heat Exchanger (Method 1): Heat exchanger Design P35/P3	N/A	0.975	Within reasonable values, adjusted to return correct outputs
Heat Exchanger (Method 1): Heat exchanger Design P7/P6	N/A	0.75	Within reasonable values, adjusted to return correct outputs

Since the propeller design was being completed simultaneously and separately in XROTOR, estimates as to the propeller dimensions are given as follows in Table 15

Table 15: PT-6A Turboprop Propeller Inputs

Property:	Unit:	Value:	Comments:
Propeller Diameter	ft	6.06955	From initial analysis (see Propeller Design section)
Propeller Design RPM	N/A	1500	Given from PT-6A manual
Propeller Efficiency	N/A	0.875	Within reasonable values
Static Propeller Efficiency	N/A	0.875	Within reasonable values

GasTurb Analysis Outputs

The PT-6A GasTurb model was validated by comparing the outputs to the known Pratt Whitney PT-6A engine manual recorded values. The output engine temperatures were all within 20% of the manual values. The recorded power output of the engine was 850 hp, the GasTurb model was 846.5 hp. The turboprop outputs are given in the table below, the additional thrust output is included and is estimated to be 3000 lbs for the actual PT-6A.

Table 16: Current Turboprop Model Flow Rates, Total Temperature, and Total Pressure

Station	Mass Flow Rate (lb/s)	Total Temperature (R)	Total Pressure (Psia)
0	N/A	518.67	14.696
1	25	518.67	14.696
2	25	518.67	14.696
3	25	1082.26	154.307
3.5	25	1624.86	150.450
4	25.277	2291.67	145.440
5	25.277	1719.55	39.189
6	25.277	1719.55	19.595
7	25.277	1197.84	14.696

Table 17: PT-6A GasTurb Turboprop Model Relevant Outputs

Parameter	Value
Thrust	2836.76 lb
Power Generated	846.5 hp
Fuel Flow	0.27738 lb/s
PSFC	1.1796 lb/(hp*h)
TSFC	0.3520 lb/(lb*h)
Thermal Efficiency	0.1158 %

GasTurb Thermodynamic Cycle Graphs

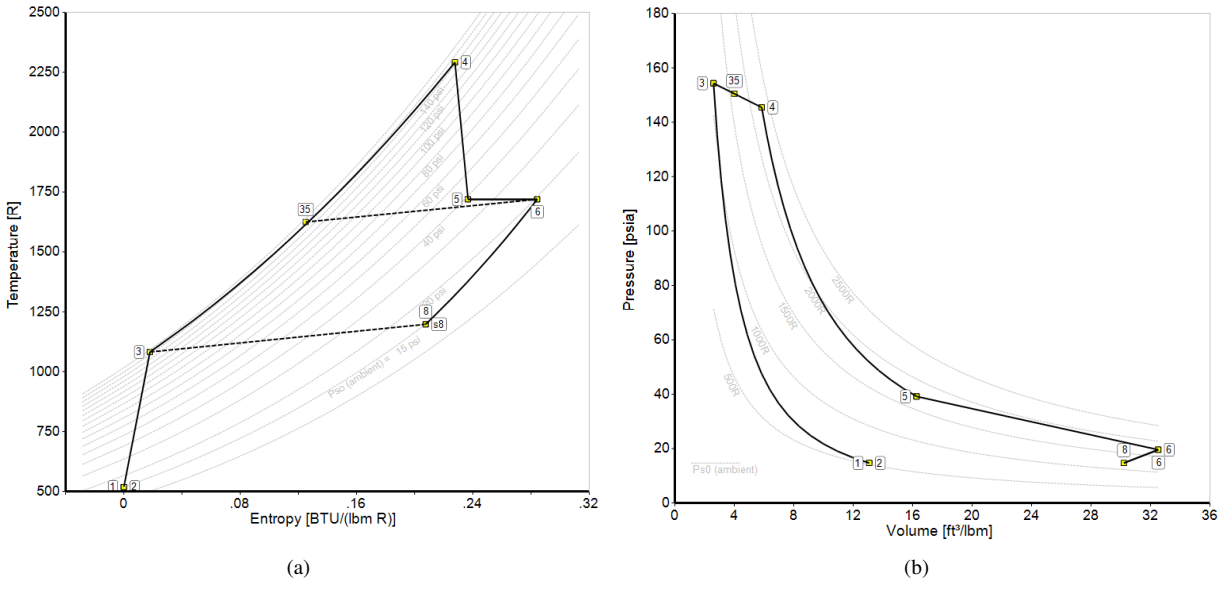


Figure 20: T-S and P-V Diagrams

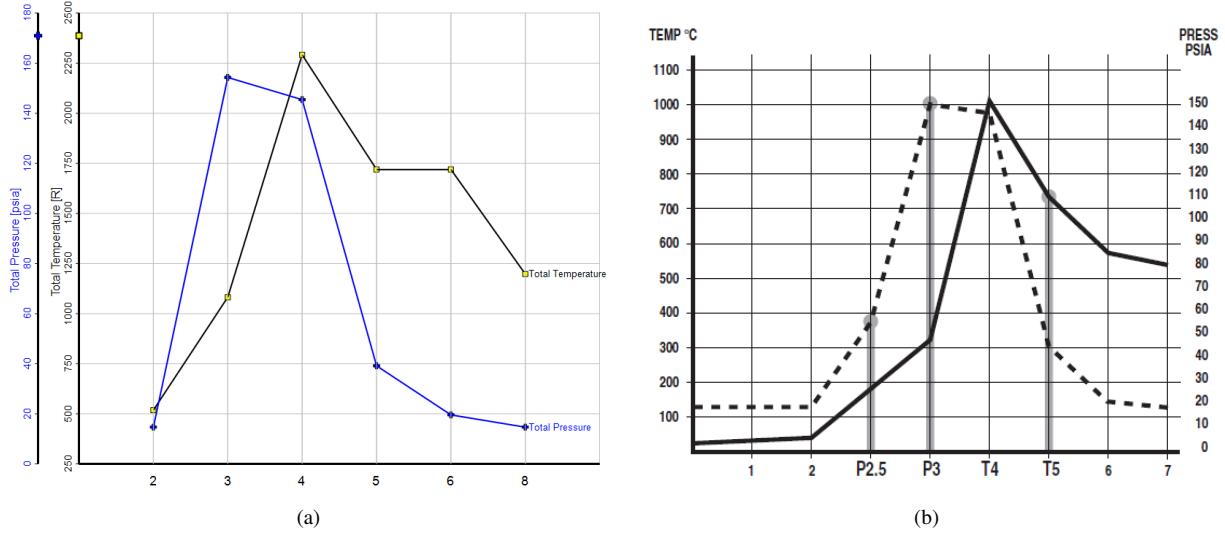


Figure 21: Total Temperature and Pressure Graphs By Engine Stage (Left: GasTurb, Right: PT-6A manual)

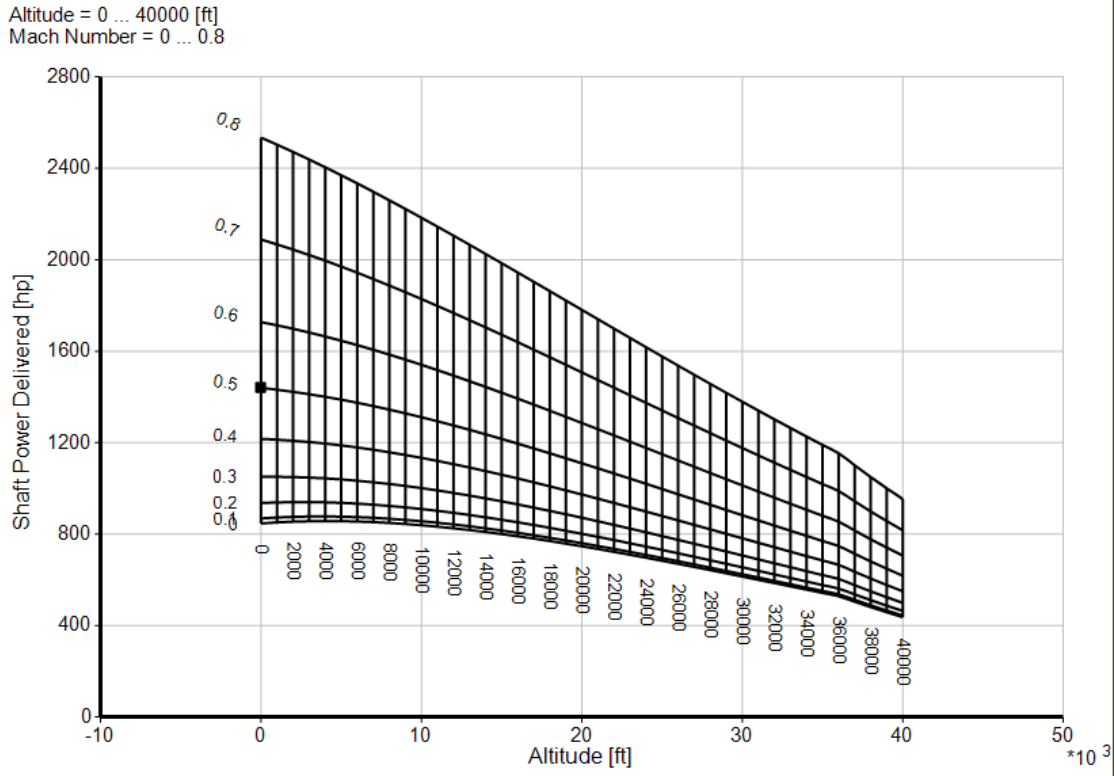


Figure 22: Parametric Analysis, Altitude and Mach Number vs. Shaft Power Delivered

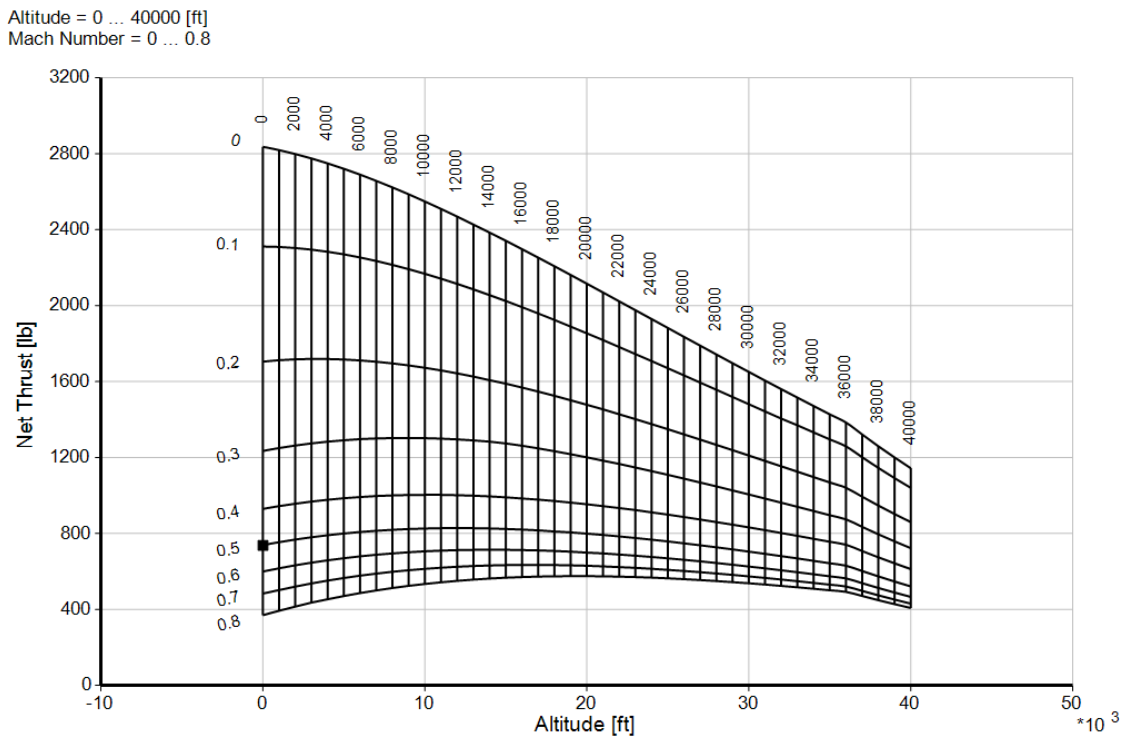


Figure 23: Parametric Analysis, Altitude and Mach Number vs. Net Thrust

Altitude = 0 ... 40000 [ft]
Mach Number = 0 ... 0.8

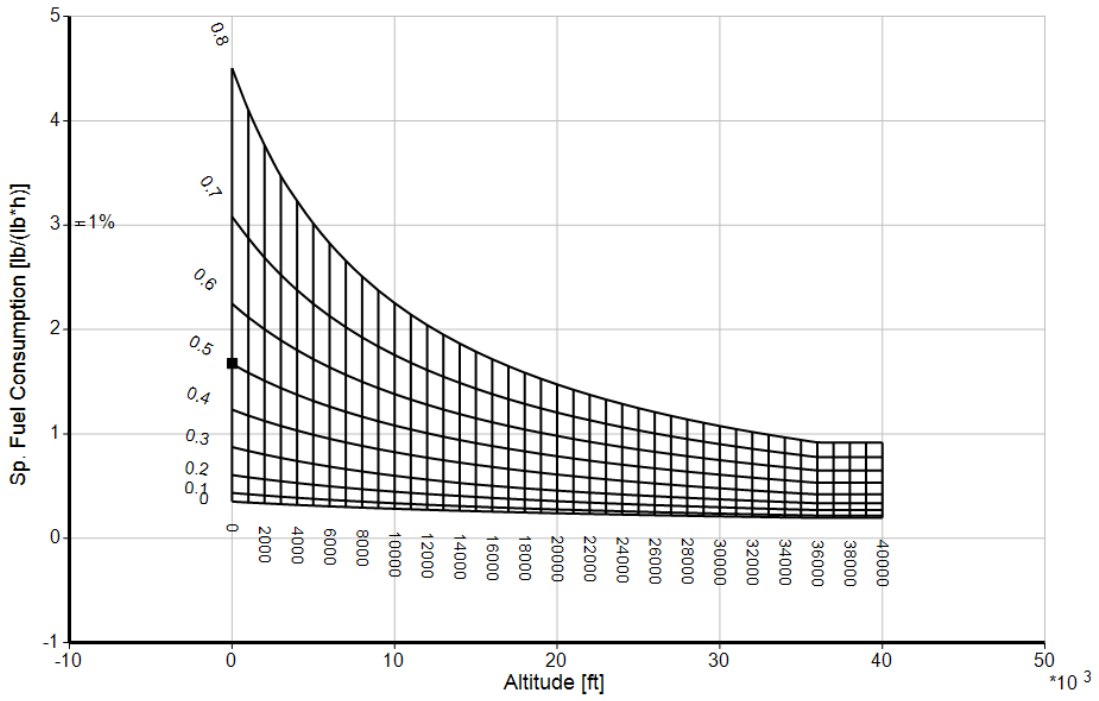


Figure 24: Parametric Analysis, Altitude and Mach Number vs. Thrust Specific Fuel Consumption

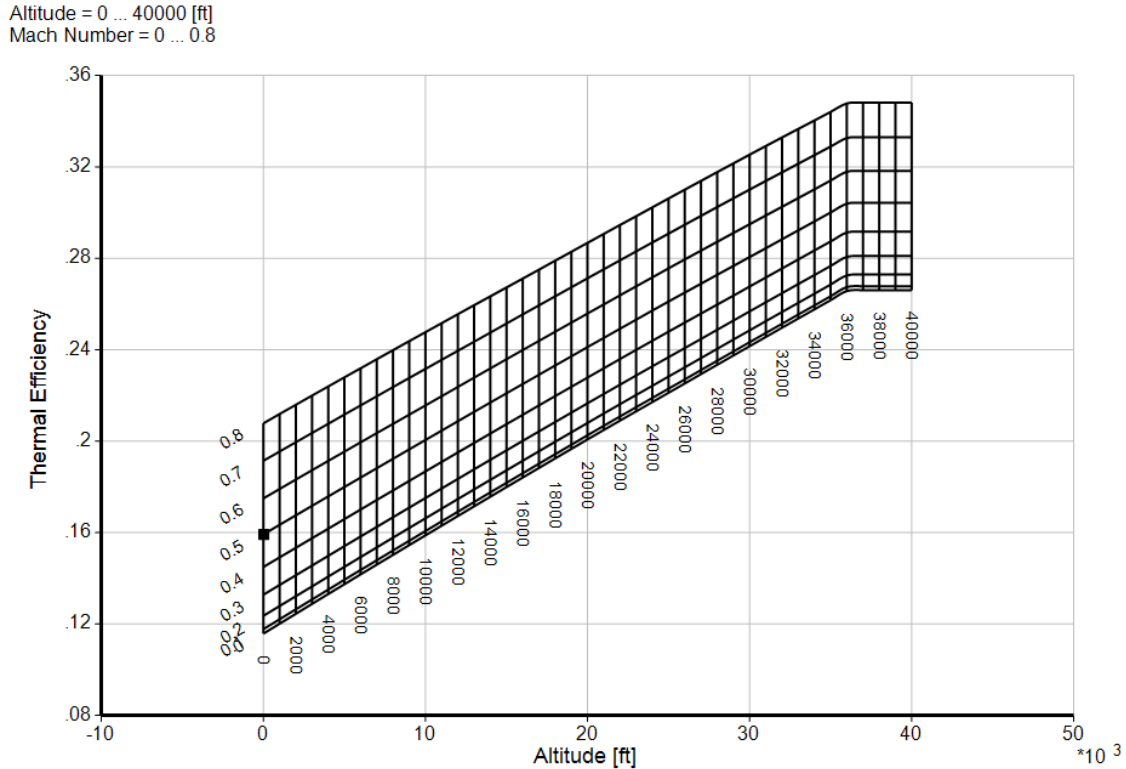


Figure 25: Parametric Analysis, Altitude and Mach Number vs. Thermal Efficiency

2025 Improved PT6-A GasTurb Model

The RFP calls for a propulsion system that is optimized for 2025 engine technology. The likelihood of a new light attack aircraft engine being developed in that time is low, so we decided to perform this analysis by using an existing engine platform and modifying it to include better technology, which will be discussed below. The engine outputs for this engine will be used in the aircraft performance discussion.

Proposed Improvements and Expected Gains

Engine cycles are limited by several bounds: the maximum stored energy in the fuel, the maximum service temperatures of engine materials and the maximum strengths of components in the system. The maximum performance of any gas turbine cycle will occur when the kinetic energy output by the system is equivalent to the total energy of the fuel input to the system, this of course is never truly possible as there are always extreme losses to entropy, escaping heat, acoustics, and many other inefficiencies. The best engine designers can do is to modify and improve engine cycles to remove or limit these factors. For most modern engines, the Brayton cycle, consisting of (1) isentropic compression (compressor), (2) isobaric heat addition (combustion), (3) isentropic expansion (turbine), and (4) isobaric heat rejection (exhaust), is the basis upon which engine performance is based.

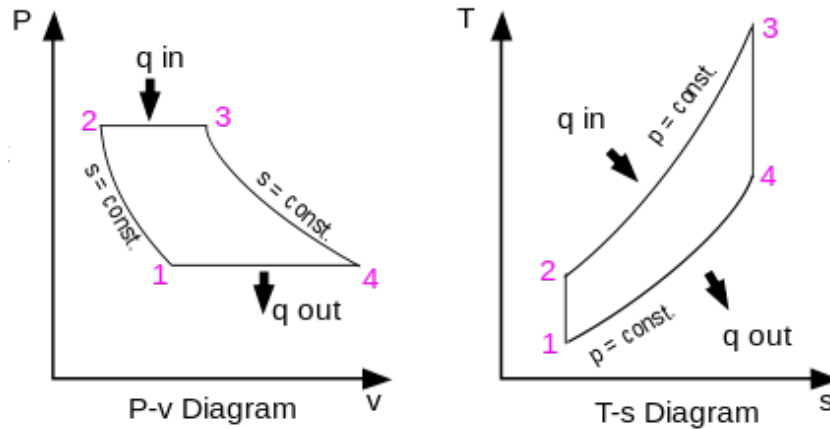


Figure 26: The Brayton Cycle [5]

Most importantly, the Brayton efficiency (%), shown below, gives a good indication of which engine components to improve to best reduce engine losses and increase performance [35, 5]:

$$\eta_T = 1 - (T_4 - T_1)/(T_3 - T_2) \quad (5)$$

Equation 5 suggests the following: when improving cycle efficiency it is beneficial to have a lower exhaust temperature, T_4 , a higher engine inlet temperature, T_1 , a higher turbine temperature, T_3 , and a lower combustion inlet temperature. In the case of a gas turbine system, these correlate to the following objectives: (1) obtaining the highest possible compression prior to combustion, (2) increasing the temperature of the fluid as much as possible during combustion, and (3) removing as much energy from the fluid as possible in the turbine section of the engine.



Figure 27: An additively manufactured component's complex cross section [6]

Within the foreseeable future, the main potential improvement to increase the strength of centrifugal compressors is the addition of additive manufacturing (AM). AM has already had a massive impact on the aerospace industry, from

rocket fuel injectors to aircraft turbines, companies like General Electric have made huge strides to both increase the quality and affordability of additively manufactured engine components, a market predicted to continue growing into the near future [6]. The benefits of using AM compressor stages include: the mechanical properties of the material can be tailored to best manage the axial forces as well as allow tighter tolerances to reduce spillage internally (for shrouded impellers), again increasing the performance of the system. Additively manufactured IN-738 nickel superalloy test coupons created via selective laser melting (SLM) were shown to have significant anisotropy in their material properties, which when optimized, can result in up to 25% increases in strength [36]. This can be directly related to increases in spool speeds and angular velocities of compressor components. Unfortunately, AM does not come without its drawbacks— mainly quality assurance and cost. Due to their complexity, it is very difficult to assess the created microstructures and geometry of AM components. Some methods require destructive testing of simultaneously printed components or advanced x-ray techniques, both of which are expensive. It is important to analyze the microstructure, as AM parts are very sensitive to unmelted particle/powder inclusions and porosity, as shown below [37]. Though it is presumed for the sake of analysis that these problems can be overcome by 2025 and direct improvements to compression ratio, spool speed, and compressor efficiency will be added.

Another practical means of increasing the temperature gain of the engine is to incorporate AM fuel injectors. As described earlier, AM has the opportunity to build very precise and complex components. In the case of the fuel injection system, AM could allow for designs that better particulate the injected fuel, increasing the exposed surface area of fuel particles and allowing closer to stoichiometric fuel combustion to occur. This would lead to greater efficiencies and slightly increased engine temperatures. General Electric predicts that not only are AM fuel injectors 25% lighter, but can improve fuel efficiency by upwards of 5% [6]. An AM fuel injection system will be included and can be seen in the increased burner efficiency parameter.

Another potential solution to increasing the pressure at the combustion chamber inlet is to utilize a water mist or coolant before the fluid enters the compressor stage of the aircraft. The justification for this is that the coolant/mist will cool the air, reducing its volume and increase the mass flow rate into the compressor. This system presents the practical questions of how to cool the water and where the water would come from. It may be practical in this case to utilize a hydrogen fuel cell auxiliary power unit, whose byproducts of functioning are electricity and water. These systems in CFD simulations have been shown to increase takeoff and landing performance as well as generally improve aircraft efficiency (as predicted by the Brayton efficiency) [38]. Lastly, these systems will expose the engine to additional moisture so internal corrosion and oxidation may be accelerated, especially in unprotected metals and aft end ceramics. Ultimately, in a trade study analysis, it was found that these systems were expensive, reduced survivability, and could lead to unforeseen damage to the aircraft and engine, we did not decide to implement these changes in the engine platform.

A consideration for engine improvements was the use of electric aircraft propulsion. Aside from the obvious

reason of cleaner energy, the major benefit of electric propulsion would be decreasing the noise profile of the engine. Given that stealth is a concern and the aircraft is expected to loiter for 45 minutes in what could be a dangerous area, decreasing the noise profile in this manner could be invaluable. Additionally, there is some evidence that EAP could improve certain performance metrics of the aircraft. The main drawback of EAP is that it is a relatively new field compared to the other forms of propulsion explored before, especially for military aircraft. Currently, the foremost electric aircraft in the field is the X-57 Maxwell. The X-57 uses Lithium-Ion batteries to power its 14 electric motors which are distributed throughout the wing. Due to the capacity of the batteries, the plane may only be used for relatively short flights, which is a deterrent given the RFP's longer ferry mission [34].

The next major objective for engine designers is to increase the temperature gain during combustion, this is typically limited by the melting temperature of the materials used in the combustion chamber and high pressure turbine sections afterwards. This is achieved through use of high service temperature materials or by applying thermal barrier coatings (TBC's) (with high melting and sintering temperatures) to lower exposure temperatures of structural materials (usually metals). In the case of high temperature engine materials, metals typically have optimal strengths but lack in high melting temperatures, while ceramics, in this application, are very desirable, as they have extremely high melting temperatures (though for some, high temperature phase transformations may present a concern) and high strengths (though brittle failure is more probable with ceramic materials). This class of materials is classified as ultra-high temperature ceramics, and research is currently focused on borides, carbides, and nitride materials. The application of TBC's onto the structural metals in the engine will similarly allow higher operation temperatures. These materials will be technologically feasible by 2025 and will be worth the additional expenses, they will be implemented to the improved engine.

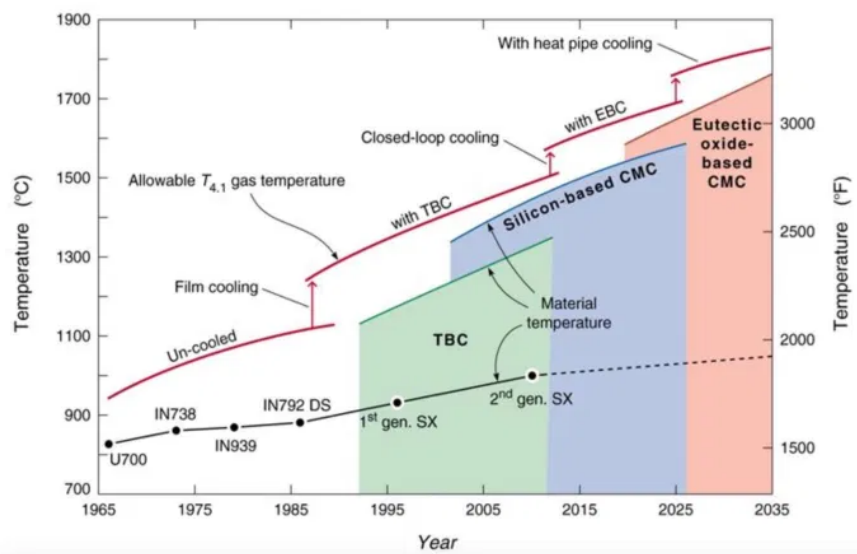


Figure 28: Expected Future Engine Temperature Capabilities [7]

Lastly, some other considerations for improving the combustion process include use of alternative fuels and ignition methods. One future technology that may be implemented is that of hydrogen fuel. Though impractical for our application as it can be volatile, has a low density, and would require cryogenic storage conditions, hydrogen fuel is enticing because it has a much higher energy density than traditional hydrocarbon jet fuels and could result in greater thrust outputs and efficiencies, as well as potentially mitigating environmental concerns (for general aviation) [39]. Lastly, to further justify improvements to our turboprop engine, more general aviation trends were used. These trends were based on the justification that computational fluid dynamics and improvements in engine materials will make future engines capable of producing more thrust, less aerodynamic drag, and having less weight. It was predicted that an improvement in thermodynamic efficiencies by 0.4% per year until 2025, resulting in a total 2% increase in thermodynamic efficiency, predominantly shown in compressor and turbine sections of the engine, this claim is substantiated from implementation of previously mentioned use of AM components, stronger materials, and TBC coatings. Similarly, the propulsive efficiencies showed a 0.3% increase per year and a 1.2% increase by 2025. The same source was also able to predict an improvement of 6% in regards to engine cooling losses, again enabled by AM, specifically losses from oversized air-cooling channels in turbine blades (prevalent in modern engines) could be removed by 2025. The same source suggests that future combustion efficiencies can be as high as 99% by 2025, converting almost all of the energy from the aircraft’s fuel source into usable energy [8].

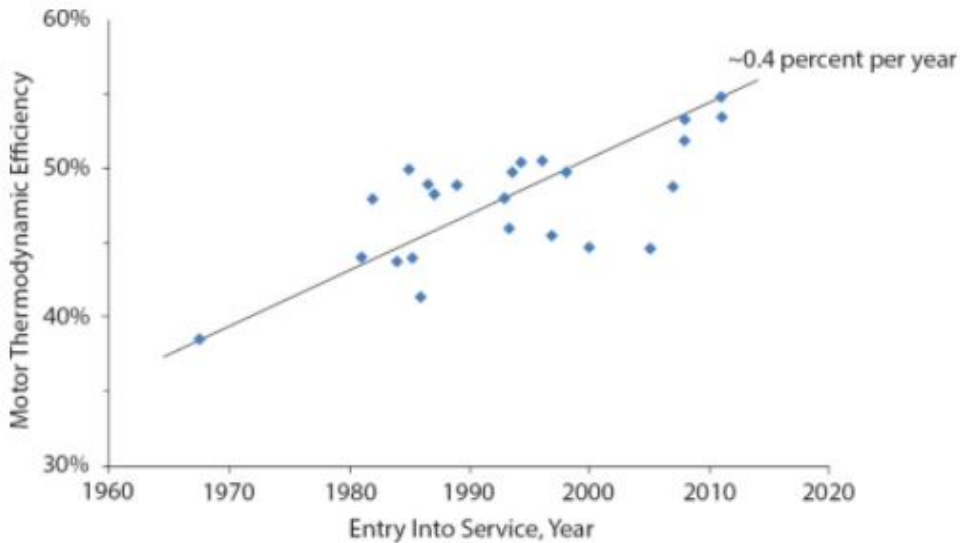


Figure 29: A Trend of Engine Thermodynamic Efficiency Improvements By Year [8]

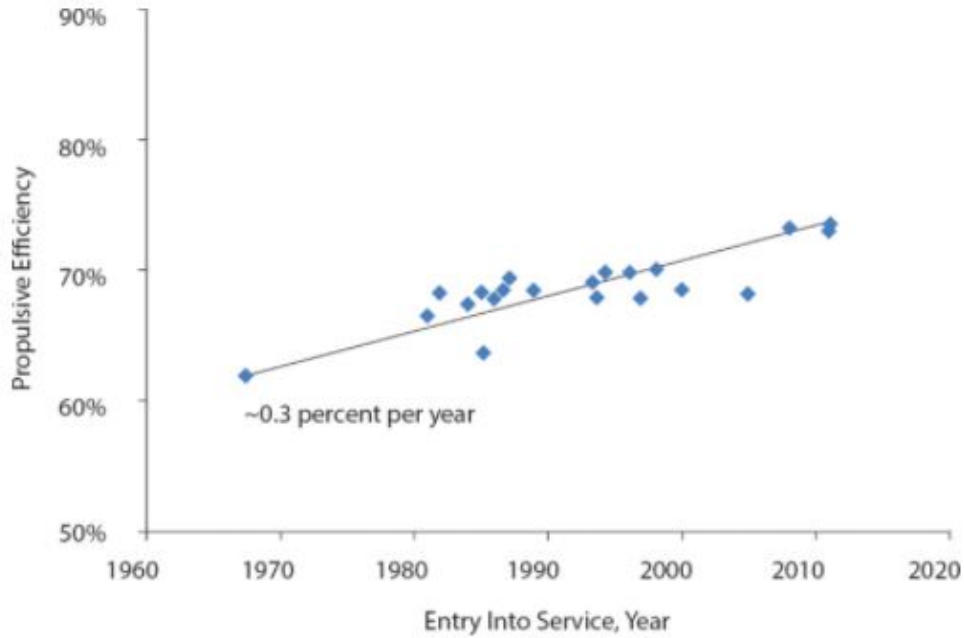


Figure 30: A Trend of Engine Propulsive Efficiency Improvements By Year [8]

A summary of engine improvements is given as follows:

- Burner exit temperature increased to 2405 R, an increase of about 5% from previous engine model [7].
- Burner efficiency increased to 99%, an increase of 5% from previous engine model [8].
- Heat exchanger efficiency increase of 6% from previous engine model [8].
- Combustor and turbine efficiency increase of 1.5% from previous engine model [8].
- Spool speed and propeller RPM up 2% account for improvements in shape and strength of materials [36].

GasTurb Analysis Inputs

The improved GasTurb model utilized the “1-spool Turboprop” with the following properties:

Table 18: Improved PT-6A GasTurb “Basic Data” Input Values

Property	Units	Value	Comments
Inlet Corr. Flow W2Rstd	lb/s	25	Recommended value (5-25 lb/s)
Inlet Pressure Ratio	N/A	1	Default
Pressure Ratio	N/A	10.5	Within the researched range (9-12.1), adjusted to return correct outputs
Burner Exit Temperature	R	2405	Improved parameter
Burner Design Efficiency	N/A	0.99	Improved parameter
Burner Part Load Constant	N/A	1.6	Default, not used in analysis
Fuel Heating Value	BTU/lb	18638	Given value for JP-4 jet fuel
Overboard Bleed	lb/s	0	Default, used to reduce mass flow in combustor, not needed
Mechanical Efficiency	N/A	0.99	Within reasonable values
Burner Pressure Ratio	N/A	0.9667	Within reasonable values, adjusted to return correct outputs
Turbine Exit Duct Pressure Ratio	N/A	0.5	Within reasonable values, adjusted to return correct outputs
Exhaust Pressure Ratio P8/Patm	N/A	1	Within reasonable values, adjusted to return correct outputs

The “Secondary Air System” values were left as default and did not contribute to the analysis. “Cooling with Steam” and “Propeller Map” options were not utilized in this analysis. The remaining inputs are documented in the following table:

Table 19: PT-6A GasTurb Additional Input Values

Property	Units	Value	Comments
Ambient Conditions: Total Temperature	R	518.67	Default, sea level conditions
Ambient Conditions: Total Pressure	Psia	14.6959	Default, sea level conditions
Ambient Conditions: Ambient Pressure	Psia	14.6959	Default, sea level conditions
Ambient Conditions: Relative Humidity [%]	N/A	0	Default
Compressor Efficiency: Polytropic Efficiency	N/A	0.915	Improved parameter
Compressor Design: Nominal Spool Speed	RPM	39780	Improved parameter
Turbine Efficiency: Polytropic Efficiency	N/A	0.915	Improved parameter
Heat Exchanger (Method 1): Heat exchanger Design Eff.	N/A	0.79	Improved parameter
Heat Exchanger (Method 1): Heat exchanger Design P35/P3	N/A	0.975	Within reasonable values, adjusted to return correct outputs
Heat Exchanger (Method 1): Heat exchanger Design P7/P6	N/A	0.75	Within reasonable values, adjusted to return correct outputs
Propeller Inputs: Propeller Diameter	ft	6.06955	From initial analysis (see Propeller Design section)
Propeller Inputs: Propeller Design RPM	N/A	1530	Improved parameter
Propeller Inputs: Propeller Efficiency	N/A	0.875	Within reasonable values
Propeller Inputs: Static Propeller Efficiency	N/A	0.875	Within reasonable values

GasTurb Analysis Output

The improved model was validated by the researched improvement percentages, specifically the thermal efficiency: the models thermal efficiency improved by 3.19% from the original model, which is inline with the predicted 2% increase in efficiency that was researched. The model was able to show a 28% increase in thrust and a 45% improvement in shaft power delivered. Further, GasTurb predicted a slightly higher mass flow rate through the engine (increased by 15%) and fuel flow rate (14% improvement). The results are as follows:

Table 20: Improved Turboprop Model Flow Rates, Total Temperature, and Total Pressure

Station	Mass Flow Rate (lb/s)	Total Temperature (R)	Total Pressure (Psia)
0	N/A	518.67	14.696
1	28.940	518.67	14.696
2	28.940	518.67	17.433
3	28.940	1082.26	154.307
3.5	28.940	1651.69	150.450
4	29.306	2405.00	145.440
5	29.306	1801.75	39.189
6	29.306	1801.75	19.595
7	29.306	1259.91	14.696

Table 21: Improved PT-6A GasTurb Turboshaft Model Relevant Outputs

Parameter	Value
Thrust	3645.52 lb
Power Generated	1233.3 hp
Fuel Flow	0.31694 lb/s
PSFC	0.92516 lb/(hp*h)
TSFC	0.3130 lb/(hp*h)
Thermal Efficiency	0.1477%

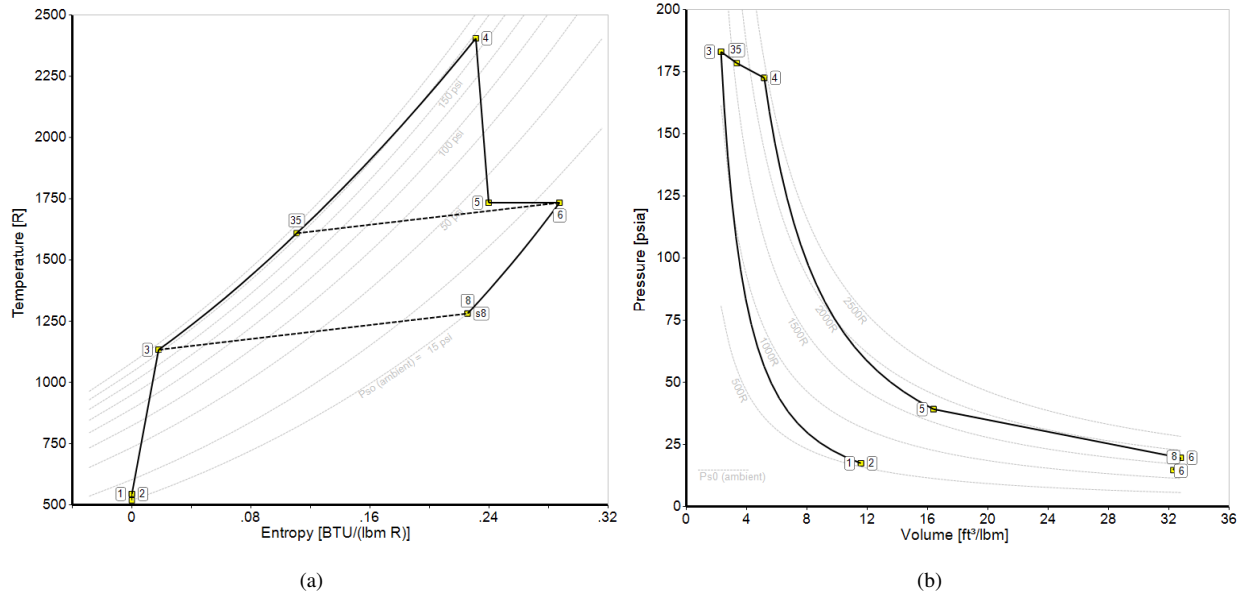


Figure 31: T-S and P-V Diagrams

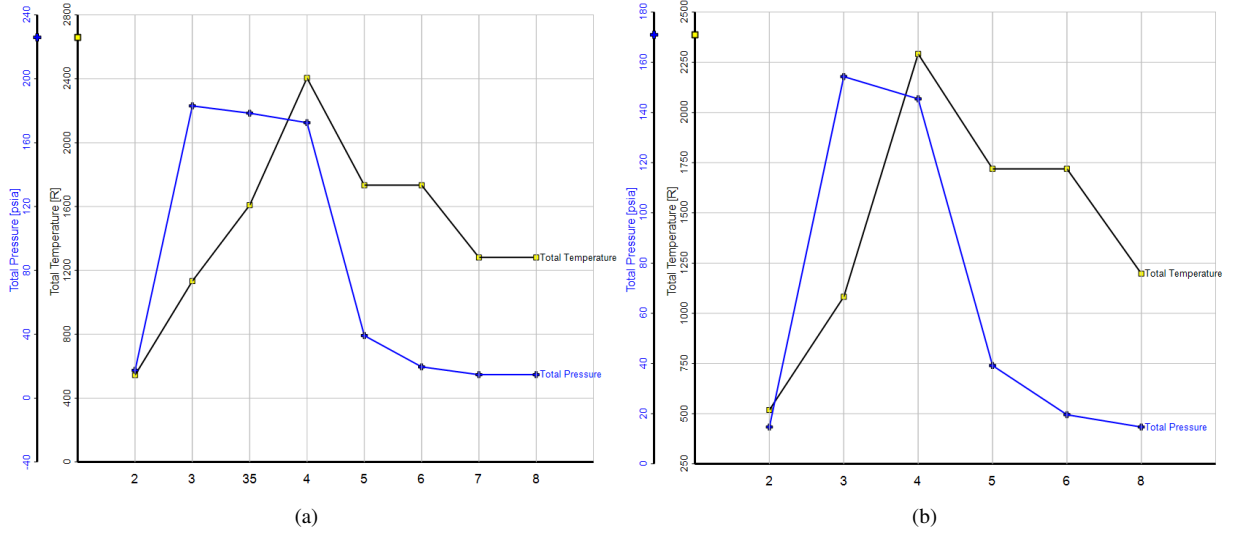


Figure 32: Total Temperature and Pressure Graphs By Engine Stage (Left: 2025 PT-6A GasTurb, Right: Current PT-6A GasTurb)

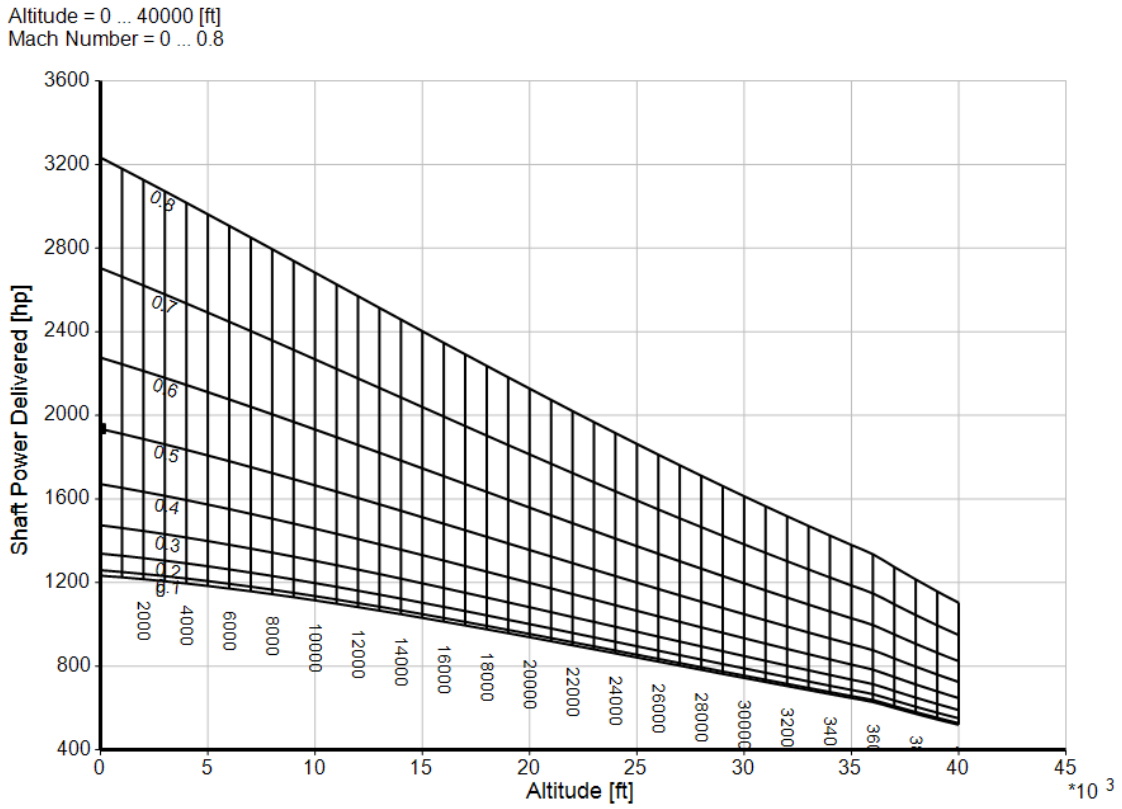


Figure 33: Parametric Analysis, Altitude and Mach Number vs. Shaft Power Delivered

Altitude = 0 ... 40000 [ft]
 Mach Number = 0 ... 0.8

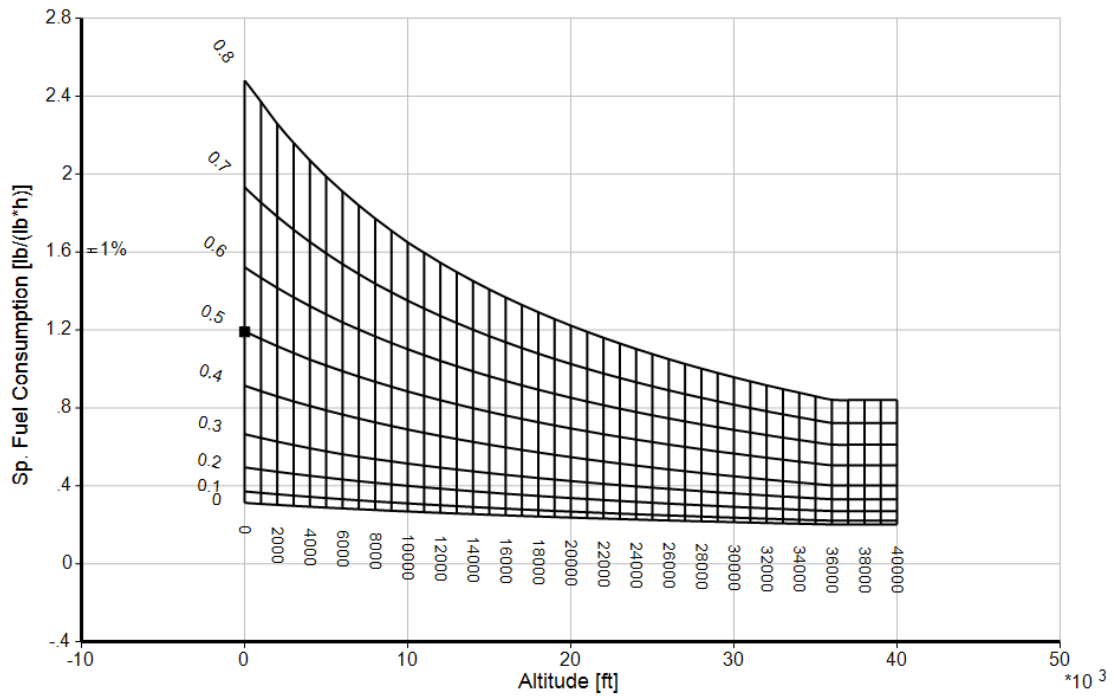


Figure 34: Parametric Analysis, Altitude and Mach Number vs. Net Thrust

Altitude = 0 ... 40000 [ft]
 Mach Number = 0 ... 0.8

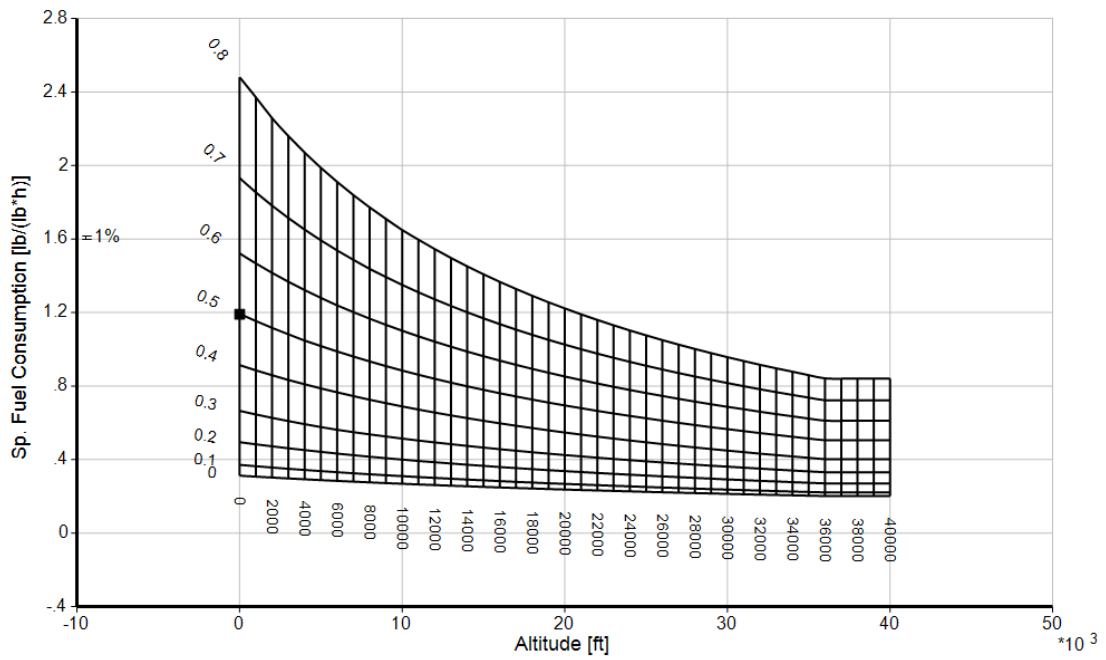


Figure 35: Parametric Analysis, Altitude and Mach Number vs. Thrust Specific Fuel Consumption

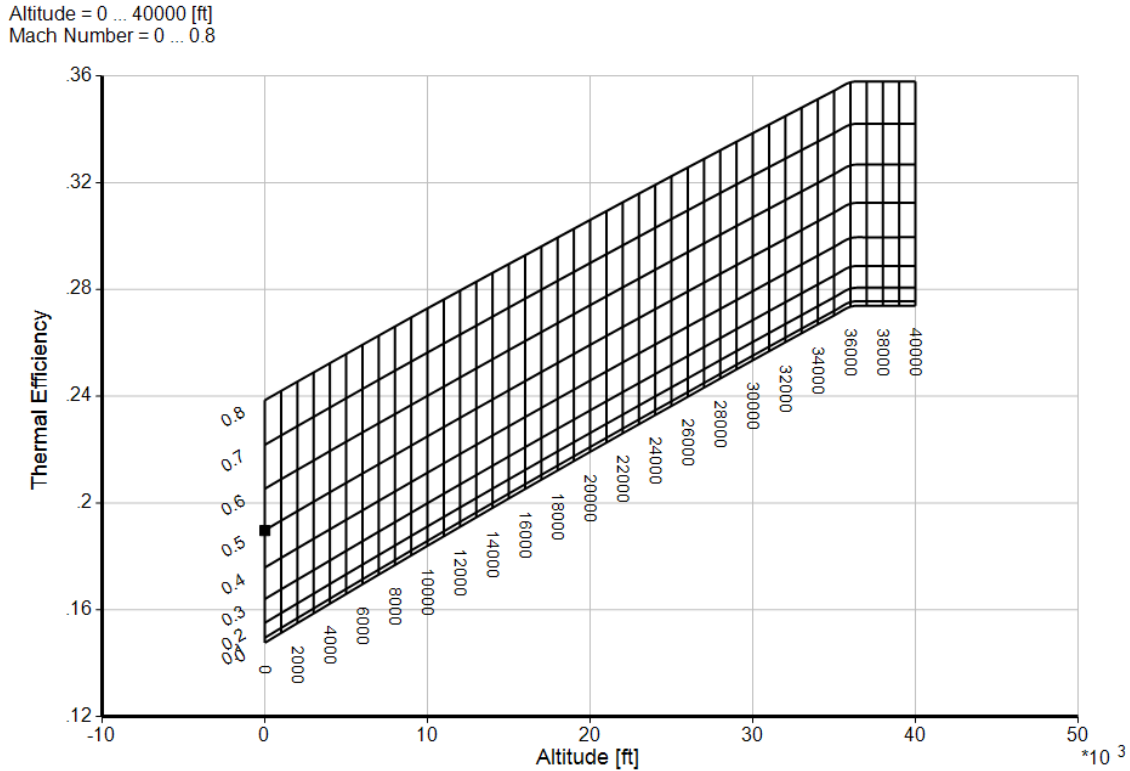


Figure 36: Parametric Analysis, Altitude and Mach Number vs. Thermal Efficiency

X.5 Rotor

Based on RFP requirements and trade studies performed by the team, it was determined that an aircraft design powered by a single turboprop would be optimal. XROTOR was chosen as the design tool based on the team's previous experience with the program and it being an extensively used tool in the professional aerospace community. The following sections will detail XROTOR's capabilities, the initial rotor design, the iterative refinement process, and the final rotor design.

About XROTOR

XROTOR is a design and analysis software for ducted propellers, free-tip propellers, and windmills [17]. The program has many capabilities available to the user including: automated design of minimum induced loss rotor, interactive medication of a rotor geometry, twist optimization, operating parameter envelope analysis, structural analysis, acoustic analysis, plotting of geometry, aerodynamic parameters, and performance maps, and many more. The program offers three main formulation techniques for analysis: graded momentum, potential, and vortex. All case studies for the final model were run using the most accurate and computationally expensive method, vortex formulation. This program was created by Dr. Mark Drela and Harold Youngren in collaboration with MIT and offered in both Unix and Windows 32

environments. The objective of XROTOR design and analysis for this project is to initially design the rotor, modify the rotor, obtain thrust and efficiency values, and analyze the acoustics of the rotor.

X.6 Initial Rotor Model

The initial rotor model was developed in XROTOR using a combination of published PT6A values and research on typical single turboprop aircraft rotors. The inputs seen below in Table 22 were used to design the initial rotor in the DESI sub menu. Additionally, this model was generated using the XROTOR default graded momentum formulation.

Table 22: XROTOR Inputs for Initial Rotor Model

Property	Units	Value	Comments
Blades	N/A	5	Based on Super Tucano
Tip Radius	ft	3	Estimated, nominal value
Hub Radius	ft	0.41	Estimated, nominal value
Hub Wake Displacement	ft	0.164	Estimated, nominal value
Velocity	ft/s	196.9	From Initial Takeoff Calculations
RPM	RPM	2200	From PT6A-6 data
Power	hp	1691	From PT6A-68C data
Lift Coefficient	N/A	0.5	Estimated, nominal value

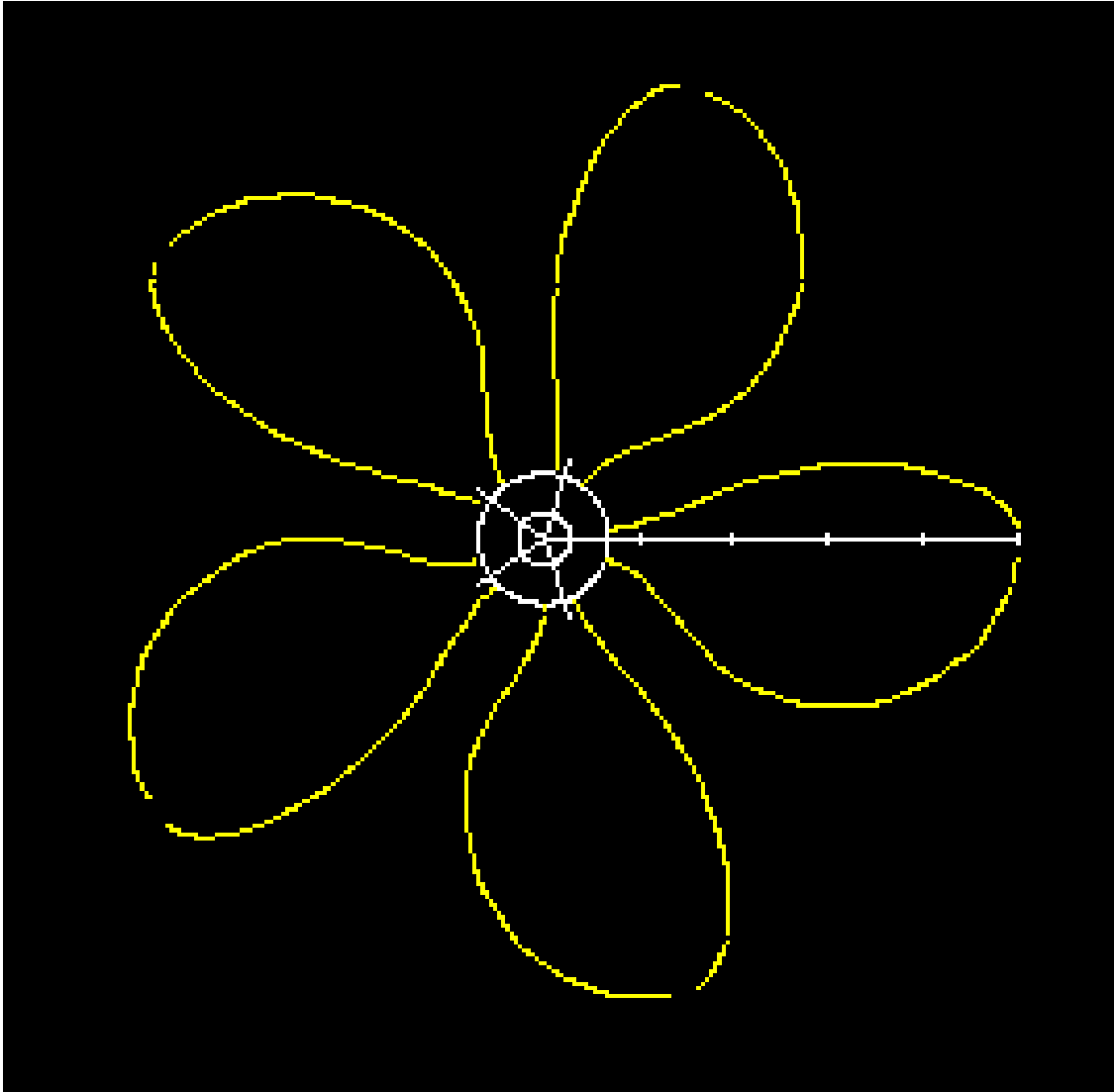


Figure 37: Initial Rotor Model Front Geometry

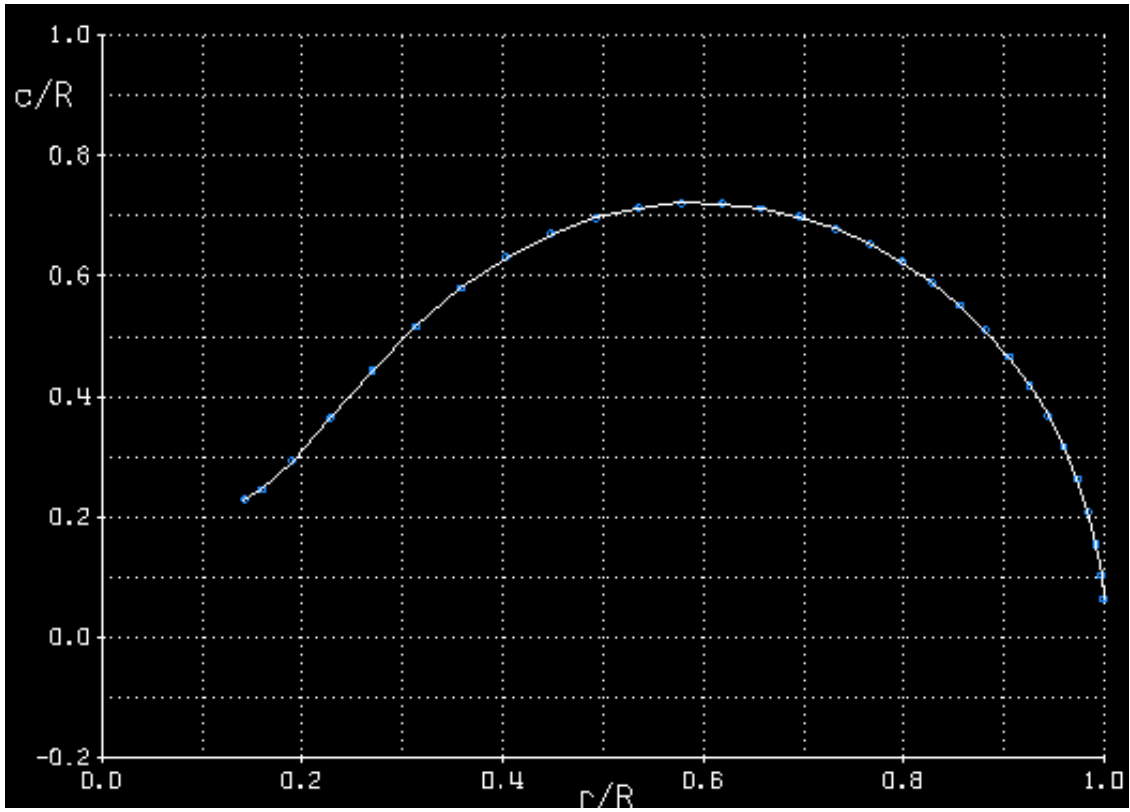


Figure 38: Initial Rotor Model Chord Distribution (c/R vs r/R)

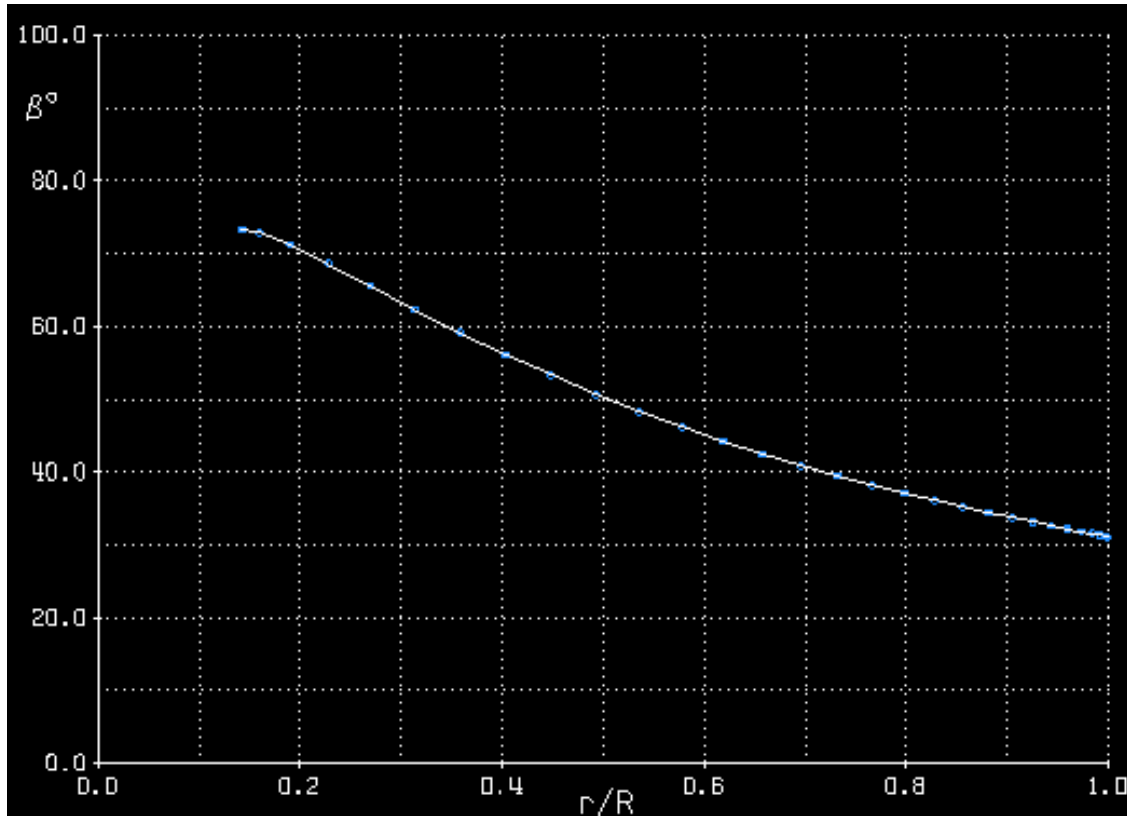


Figure 39: Initial Rotor Model Blade Twist Angle Distribution (β° vs r/R)

The front geometry, chord distribution, and blade twist distribution of the initial rotor produced are shown above in Figures 37 to 39. This design acted as the base model for all future modifications and optimizations. However, because this rotor was created based on early estimations for the takeoff case and generalized research, it was incapable of supporting steady level cruise. The next section will describe the methods used to improve this initial design and the final rotor model.

Final Rotor Model

The RFP states multiple specific objectives and requirements that relate to and constrain the rotor design and propulsion in general: takeoff field length of under 4000 ft, maximum efficiency for extended periods of cruise, and a service ceiling above 30000 ft. Creating the initial rotor model based on takeoff conditions emphasized the priority of maximizing low velocity thrust; however, in order to continue producing thrust at higher velocities and altitudes, the rotor needed significant modifications. The MODI sub menu of XROTOR offered multiple functions and tools to improve the initial design. The first series of modification iterations involved scaling down the chords to increase rotor thrust and efficiencies for the cruise and service ceiling cases. Using the SCAL function in XROTOR, changes can be applied radially to all blades according to the following function:

$$(Chord)_{new} = (Chord)_{old} \cdot [A + B \cdot (r/R)] \quad (6)$$

where A is the Constant Chord Scaling Factor and B is the Linear Chord Scaling Factor. The final chord distribution seen below in Figure 40 was developed after multiple iterations of scaling the chord using both scaling factors. By comparing Figures 38 and 40, the resulting chord distribution modifications can be described as both constantly decreased, as well as linearly relaxed as the radius increases.

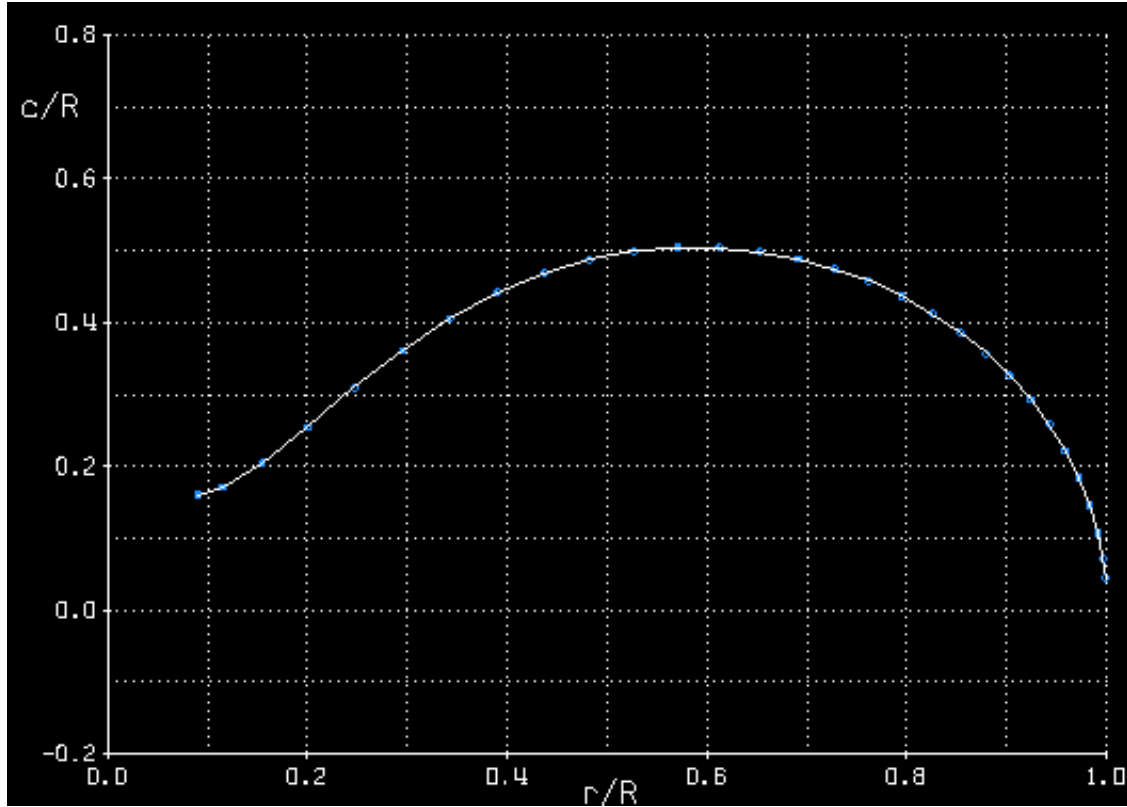


Figure 40: Final Rotor Model Chord Distribution (c/R vs r/R)

The second major modification made to the initial rotor design dealt with the blade twist angle distribution. XROTOR offers the OPTI function which finds the most efficient twist angle distribution for a given rotor design. Using this function produced the twist angle distribution seen below in Figure 41. It is worth noting that the β_0 spike seen at the maximum radius was caused by an unknown $\alpha(CL)$ function inversion failure and has no perceivable impact on rotor performance.

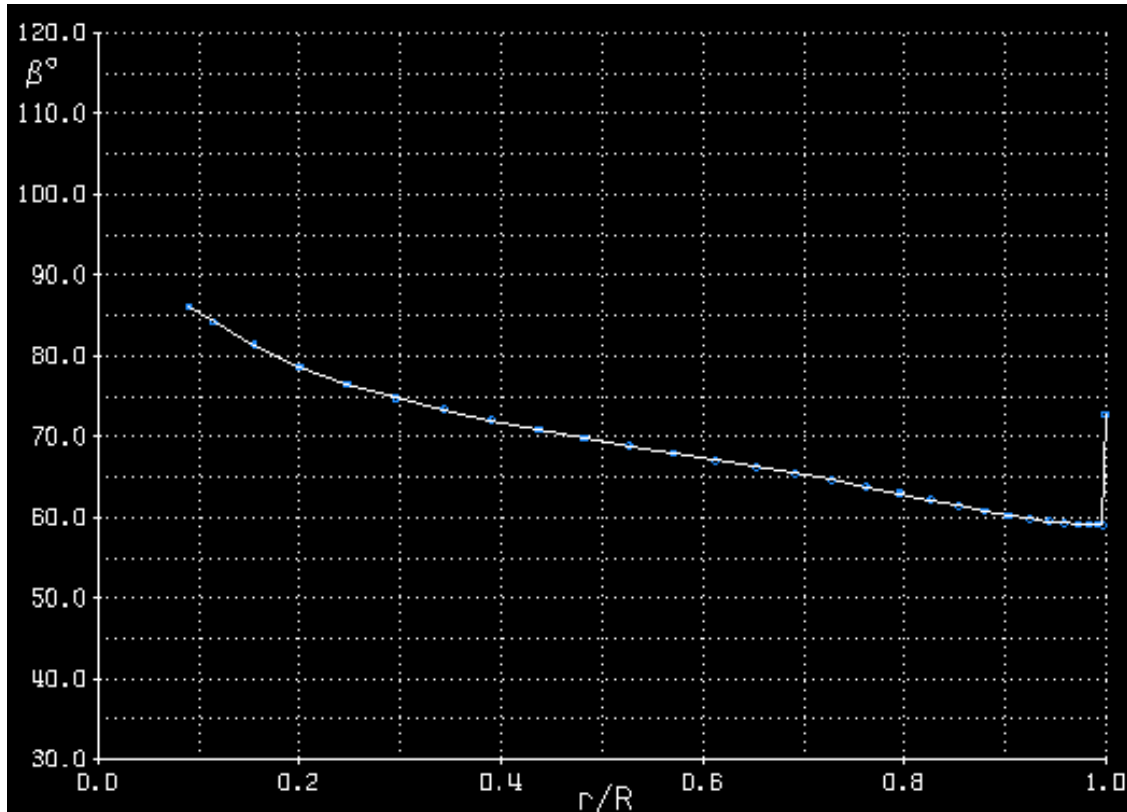


Figure 41: Final Rotor Model Blade Twist Angle Distribution (β° vs r/R)

The final modification to the rotor design consisted of modifying both the central hub radius and hub wake displacement radius to be more consistent with previous design studies conducted using XROTOR [40]. This change manifested in both values being set to 0.246 ft, a decrease in hub radius and an increase in hub wake displacement radius. The resulting final rotor model front geometry is presented below in Figure 6. The performance outputs and case studies conducted with this final propeller design can be found in the Performance section of this work.

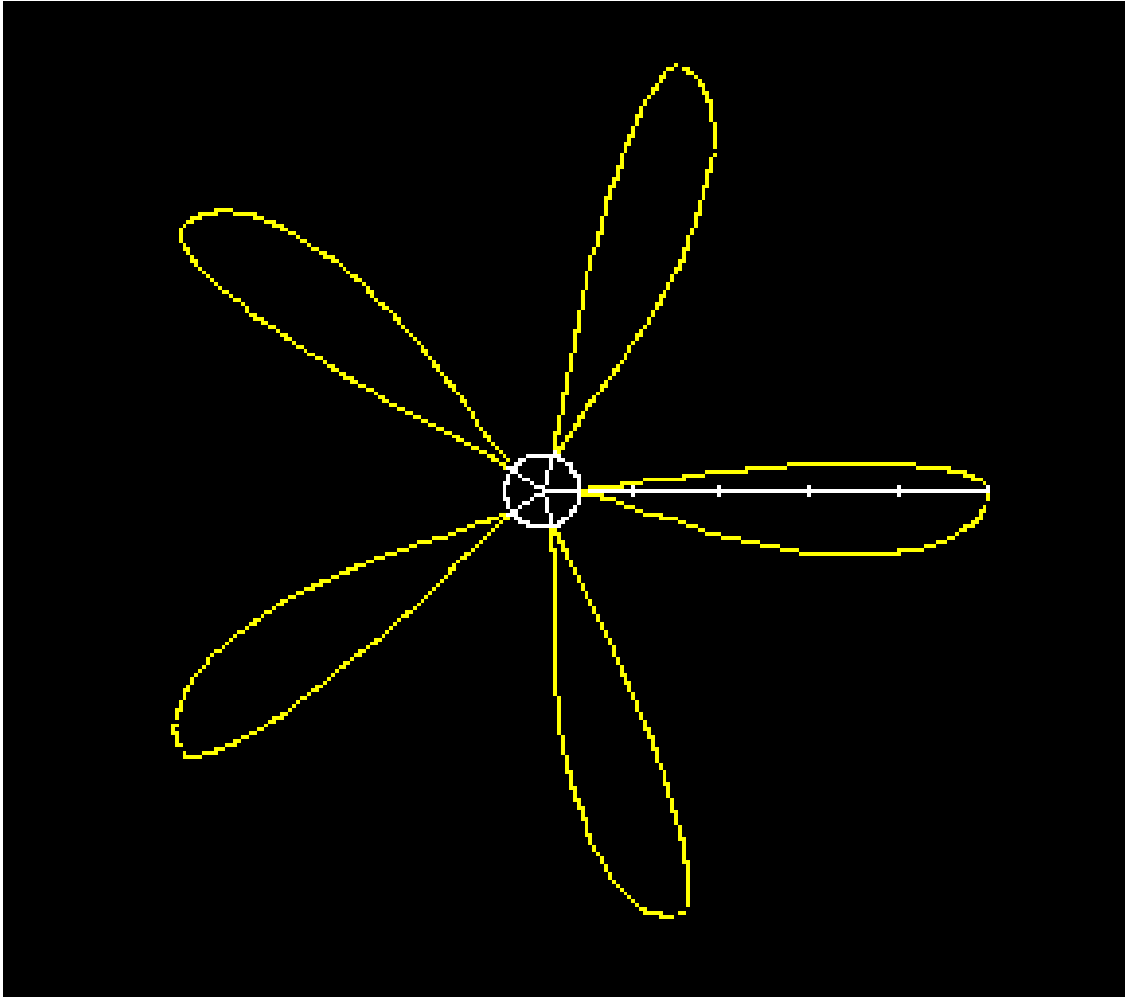


Figure 42: Final Rotor Model Front Geometry

XI Structural Design

XI.1 Wing Stress

For the wing structure of the design a multi-rib layout with two I-beam spars along the wing was chosen and selected the aluminum alloy 7075-T6 as the material due to its relatively low density and high yield strength. The wing configuration can be seen in figure 43.

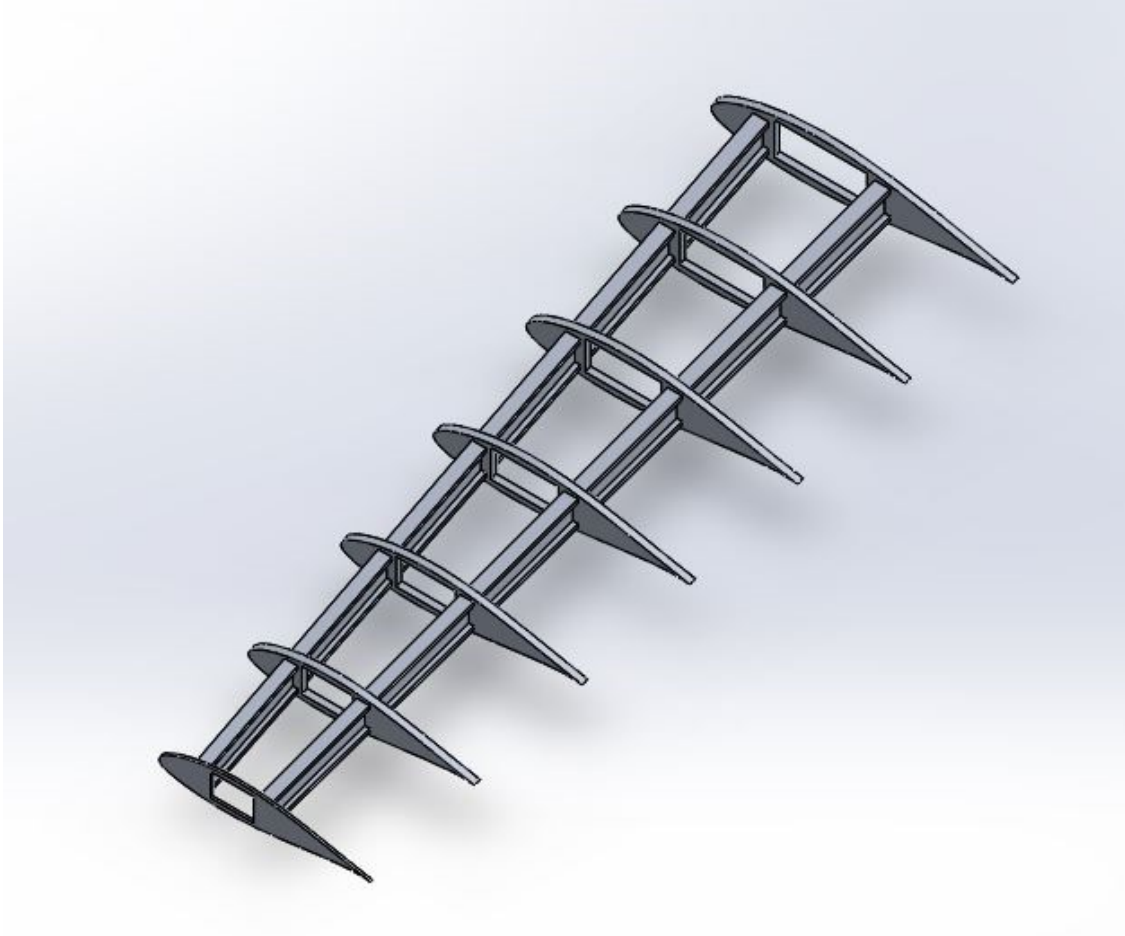


Figure 43: Wing Configuration

The ribs are tapered from the root chord of the wing to the tip chord and are swept at the angle specified in the wing design. The cutouts in the center of each rib serve to not only reduce the weight of the wing, but can also allow for storage inside of the wing. The initial model of the wing was well above the estimated weight from the equations and had a very high margin of safety, so the size of the spars were reduced in order to obtain a result closer to the weight estimation. A study on the structure in Solidworks to analyze the stress on the wing when the aircraft is experiencing an ultimate load factor of 3.75, and the results can be seen in Figure 44.

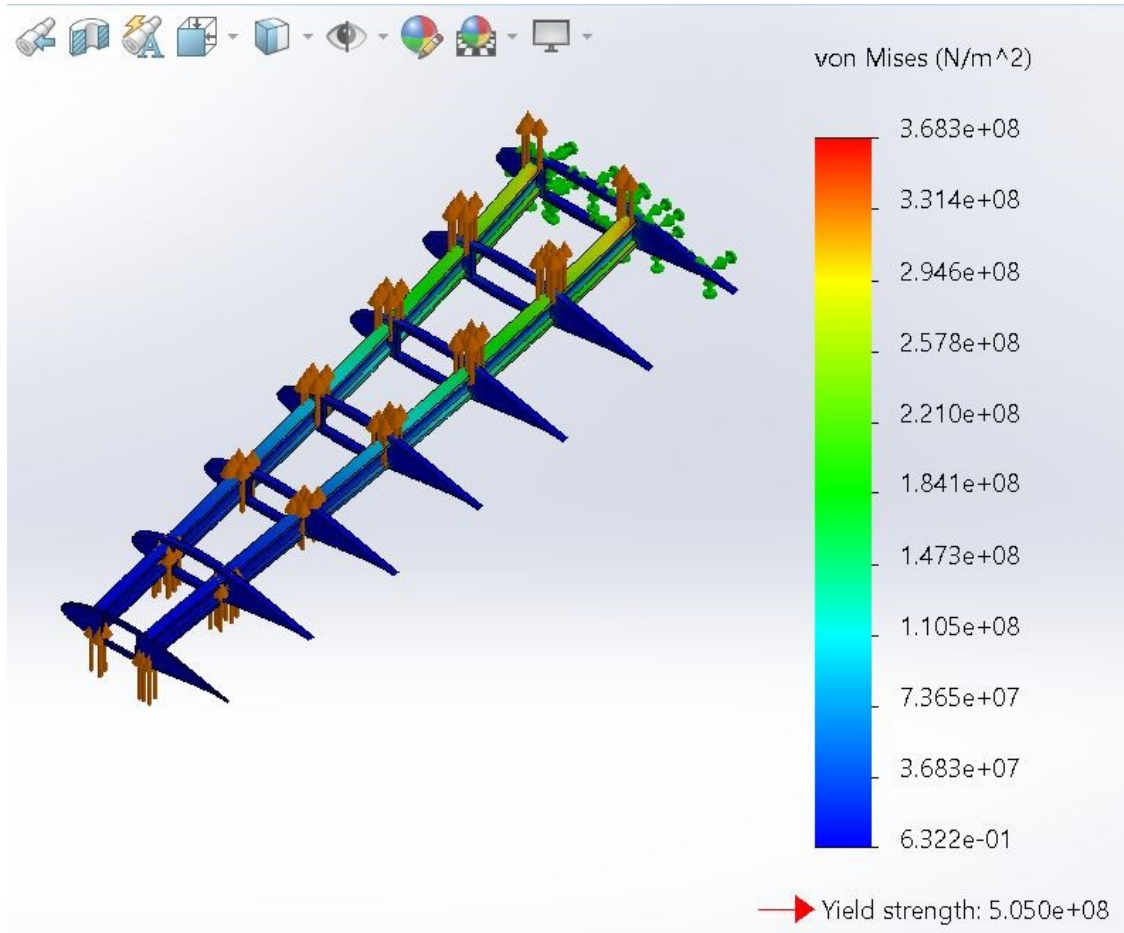


Figure 44: FEA of the Wing

In this case, the factor of safety is 1.37 when the aircraft is under the ultimate load.

XI.2 V-n diagram

To determine the flight envelope of the aircraft a V-n plot was made. Using a Matlab plotter, Figure 45 was made [41]. This plot shows the envelope for flaps down (outer line) flaps down (innermost lines), and at ultimate load factors (ULF) of 3.75 and 6. 3.75 was chosen since it is the assumed value in FLOPS and satisfies the FAR requirement that the ULF be greater than equation 7 but less than 3.8. For The Hummingbird equation 7 is equal to 3.08.

$$n = 2.1 + \frac{24000}{MTOW + 10000} \quad (7)$$

6 was also chosen since that is the expected load from a rolling pull out maneuver from MIL-A-8861 B [42]. Table 23 lists all the important envelope speeds.

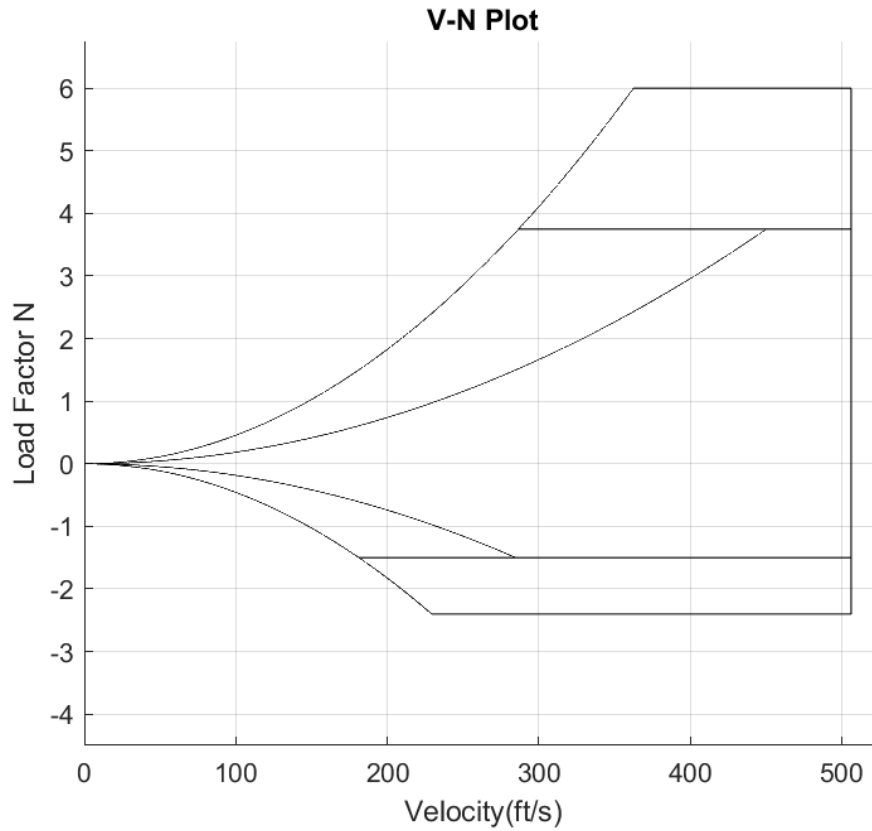


Figure 45: V-n Diagram

Table 23: Design Speeds from the V-n Diagram

Design Speeds	Velocity (ft/s)
Cruise	337
Stall (Flaps Up)	145
Stall (Flaps Down)	231
Maneuvering Speed (Flaps Up)	450
Maneuvering Speed (Flaps Down)	287
Negative Maneuvering Speed (Flaps Up)	279
Negative Maneuvering Speed (Flaps Down)	179
Dive Speed	506

To calculate and plot a V-n Plot with gust lines a different Matlab plotter was used. This plotter only calculates in metric, however, are identical to values found in Table 23 [43].

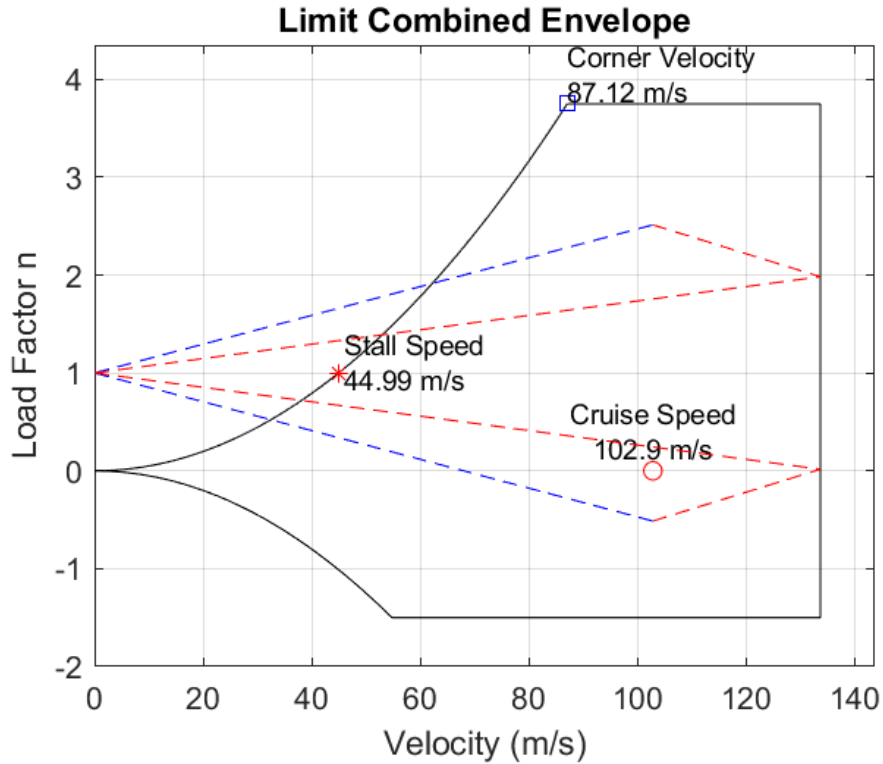


Figure 46: V-n Diagram with Gust Lines With ULF = 3.75

XII Weight Statement

XII.1 Initial Estimates

For the initial weight estimates of the structures of the aircraft, the equations provided in Nicolai and Carichner's Fundamentals of Aircraft and Airship Design were used [3]. These equations use design aspects of the aircraft to estimate the weight of the wings, fuselage, horizontal and vertical tail, and landing gear. These initial estimates are displayed in the table below.

Table 24: Empirical Weight Estimations

Structure	Weight (lb)
Wing	1237.719
Fuselage	1954.496
Horizontal Tail	87.578
Vertical Tail	39.213
Landing Gear	585.763

After designing the wing structure, Solidworks evaluated the weight of the wing to be 1379.0 lbs, making it fairly similar to the weights that were previously calculated. The consistency with weight estimation through the equations,

and Solidworks increased confidence in the weight statement calculated. These estimations were relatively close to the final weight estimations done in FLOPS.

XII.2 FLOPS Weight Analysis

The design parameters from previous sections formed the input for the FLOPS analysis both for the weight estimations and the mission analysis presented in the next section. This analysis mainly used the default values with the exception of the pilot weights to include the ejection seats, overriding the wing weight with the one outputted by the Solidworks model, the engine weight, and provisions for external payload. Table 25 shows the finalized weight estimations.

Table 25: Weight Statement

Component	Percent Weight	Weight (lb)
Wing	8.57	1237
Horizontal Tail	0.74	107
Vertical Tail	0.99	142
Landing Gear	3.50	505
Nacelle	0.42	60
<i>Structure Total</i>	<i>(27.80)</i>	<i>(4013)</i>
Engine	4.14	598
Miscellaneous Systems	0.30	44
Fuel System Tanks and Plumbing	3.36	484
<i>Propulsion Total</i>	<i>(7.80)</i>	<i>(1126)</i>
Surface Controls	4.71	680
Auxiliary Power	1.83	264
Instruments	0.76	110
Hydraulics	0.97	140
Electrical	3.23	466
Avionics	0.83	119
Armament	0.55	80
Furnishings and Equipment	1.79	259
<i>System and Equipment Total</i>	<i>(14.92)</i>	<i>(2154)</i>
<i>Weight Empty</i>	<i>50.52</i>	<i>7292</i>
Crew	2.98	430
Unusable Fuel	0.50	72
Engine Oil	0.12	18
Ammunition	1.31	200
Miscellaneous	0.01	1
<i>Operating Weight</i>	<i>55.44</i>	<i>8002</i>
External Store	20.79	3000
<i>Zero Fuel Weight</i>	<i>76.23</i>	<i>11002</i>
Mission Fuel	23.77	3431
<i>Gross Weight</i>	<i>100</i>	<i>14433</i>

XIII Performance

XIII.1 Takeoff and Landing Field Length

To calculate the Takeoff and Landing Performance, the empirical steps were used [3]. Initially, using the preliminary sizing data, a trade study on the sensitivity of Thrust and CL_{max} was done to estimate a target for the thrust and CL_{max} required.

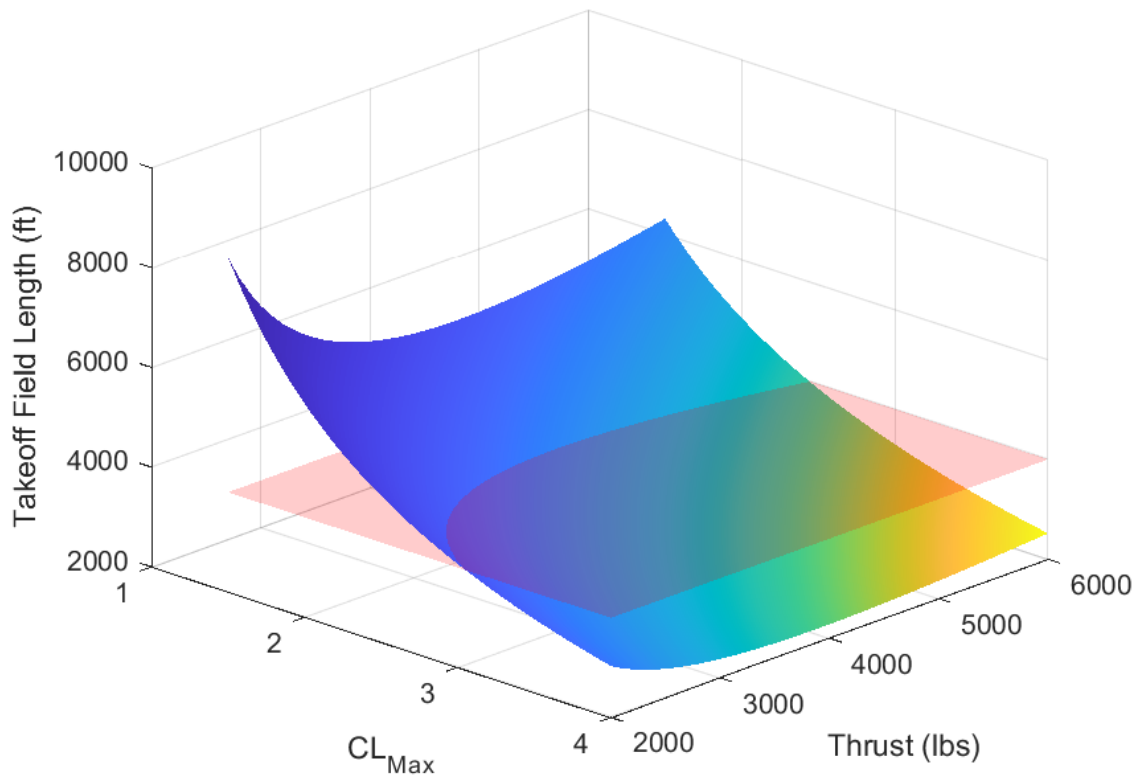


Figure 47: Sensitivity Analysis of the Takeoff Field Length

In Figure 26 one can see that the coefficient of lift maximum needs to be greater than 2 and the thrust needs to be greater than 3,000 lb. Thus a central target of 3 and 4,000 lb were chosen to give a margin if future design adjustments negatively impact either parameter. Note: the red intersecting plane is the 4,000 field length requirement.

Later when the propulsion and wings were sized and it was confirmed that a thrust of 4,000 lbs and a $CL_{2.75}$ were confirmed to be achievable, the equations were run again using those values. Table 26 and ?? tabulates the results. Appendix II has tabulated values of the assumptions made.

Table 26: Takeoff Field Lengths

Segment	0 ft Density Alt. (ft)	6000 ft Density Alt. (ft)
Ground	1708.21	2043.51
Rotation	311.34	340.53
Transition	1293.68	1547.61
Total	3313.23	3931.65

Table 27: Landing Field Lengths

Segment	0 ft Density Alt. (ft)	6000 ft Density Alt. (ft)
Approach	435.18	481.19
Free Roll	348.80	381.50
Braking	1770.88	2118.49
Total	2554.86	2981.18

XIII.2 Mission Performance

To analyze the mission performance of The Hummingbird, FLOPS was used. Using the data from the previous sections a FLOPS model of the plane can be built. FLOPS is a program designed to evaluate and optimize initial aircraft concepts. In this case, design parameters such as the lengths and weights of components are inputted along with an engine deck from the GasTurb engine model. FLOPS takes the aircraft model and simulates it through the desired design mission.

Figure 48 shows the design mission translated into a FLOPS mission.

```
# MISSION SEQUENCE DEFINITION

START          MACH NUMBER = 0.2000          ALTITUDE =          0. FT

1. CLIMB       USE CLIMB SCHEDULE 1

2. CRUISE      USE CRUISE SCHEDULE 3          SEGMENT DISTANCE = 100.0 N MI

3. HOLD        USE CRUISE SCHEDULE 2          HOLD TIME = 240.0 MIN

4. CLIMB       USE CLIMB SCHEDULE 1

5. CRUISE      USE CRUISE SCHEDULE 1          SEGMENT DISTANCE = 100.0 N MI

6. DESCENT

7. END         MACH NUMBER = 0.3000          ALTITUDE =          0. FT
```

Figure 48: Design Mission Sequence

For the climb segments the minimum speed is 0.2 Mach. For Cruise Schedule 1, FLOPS sets an optimal altitude and mach number for the desired range. Cruise Schedule 3, however, a fixed Mach, 0.533, is given while an optimal altitude for the set range is used. This difference in cruise definition enforced the 20 minute requirement to go from climb to the hold segments. The results of the FLOPS analysis are found in Table 28. The plane is carrying its full payload for this mission.

Table 28: Design Mission Results. 3126.9 lb fuel burn, Total Range of 836.1 nmi.

Segment	Initial WT (lb)	Fuel (lb)		Time (min)		Dist (nmi)		Mach		Alt. (ft)	
		Segmt	Total	Segmt	Total	Segmt	Total	Start	End	Start	End
Taxi Out	14433	7	7	5	5			0	0.2		
Climb	14426	37	44	2.2	7.2	6.8	6.8	0.2	0.3	0	10000
Cruise	14389	204	249	17.6	24.8	100	106.8	0.300	0.533	10000	10000
Hold	14184	1635	1884	240	268.4	0	106.8	0.533	0.289	3000	3000
Climb	12549	19	1903	1.2	269.6	3.5	110.3	0.289	0.3	3000	10000
Cruise	12530	1213	3115	224	493.6	714.8	825.1	0.3	0.3	10000	10000
Descent	11318	5	3120	3.5	497.1	11.0	836.1	0.3	0.3	10000	0
Reserves	11313	311	4331								
Taxi In		7		5	502.1						

For the Ferry mission a similar run is made only at 60% payload capacity and for the cruise segment, the plane flies at the optimal altitude velocity. The results are shown below in Table 29.

Table 29: Ferry Mission Results. 1325.3 lb fuel burn, Total Range of 950 n mi.

Segment	Initial WT (lb)	Fuel (lb)		Time (min)		Dist (nmi)		Mach		Alt. (ft)	
		Segmt	Total	Segmt	Total	Segmt	Total	Start	End	Start	End
Taxi Out	10999	7	7	5	5			0	0.320		
Climb	10992	38	45	2.6	7.6	7.6	7.6	0.320	0.300	0	18000
Cruise	10954	1266	1311	298.1	305.7	923.0	930.6	0.300	0.300	18000	18000
Descent	9688	8	1318	6.3	312.1	19.4	950.0	0.300	0.300	18000	0
Reserves	9680	131	1449								
Taxi In		7		5	317.1						

XIII.3 Payload-Range

Using FLOPS the maximums of the aircraft can be explored. By varying the payload capacity and expending reserves different ranges can be found. Table 30 provides the results while Figure 49 graphically shows that same information.

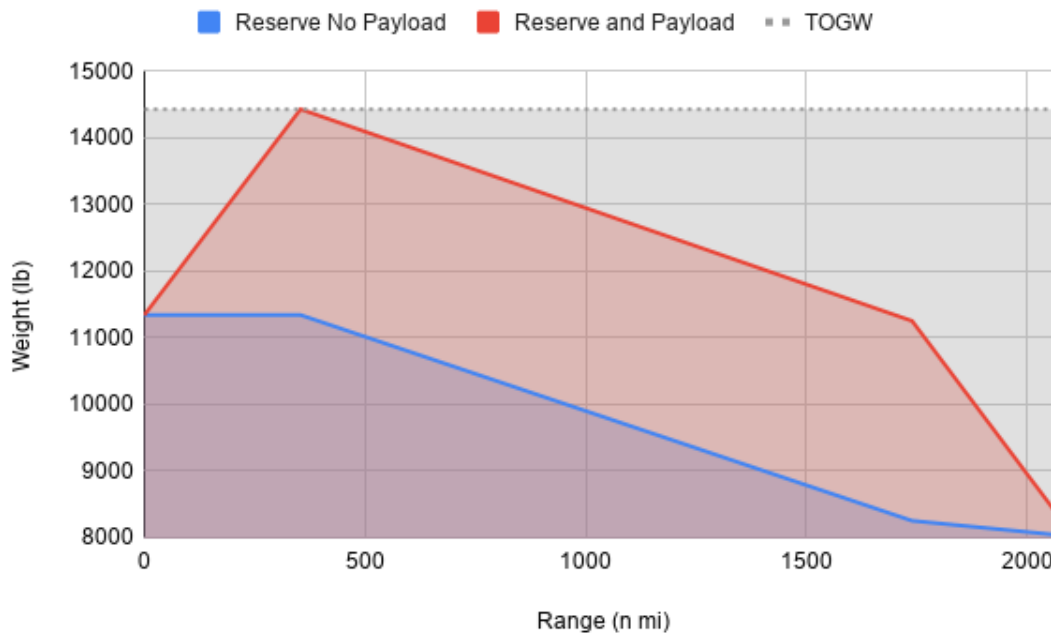


Figure 49: Payload Range Diagram. Note that the bottom of the chart is set at the OEW

Table 30: Possible Configurations to Achieve More Range

Range (n mi)	Fuel Weight (lb)	Description
0	0	Empty
354	3089	Max Payload and Fuel with Reserve
1740	6089	Theoretical Max possible Fuel Weight with Reserve Held
2080	6400	Theoretical Max possible Fuel Weight and Spent Reserve

Thus, The Hummingbird could in theory achieve a range of over 2000 n mi if all possible variable weight is converted into fuel. I.e. The theoretical max is achieved if the internal fuel cells are full and the payload was all external fuel stores.

XIII.4 Survivability

This section of the report details important performance metrics outputted by XROTOR for takeoff, cruise, and service ceiling cases. The values of importance for this project are total thrust produced and the ideal efficiency of the rotor. Full XROTOR case outputs can be found in the Appendix of this work. Additionally, acoustic analysis performed in XROTOR for each of these cases are shown. The calculations and method for determining the service ceiling can also be found in this section. Survivability considerations and implementations are discussed with reference to their importance in the RFP.

Takeoff

Below are the inputs and outputs, as well as the acoustic analysis plot, for the XROTOR takeoff case.

Table 31: XROTOR Inputs for Initial Rotor Model

Property	Units	Value	Comments
Power	hp	1300	Based on improved PT6A model
Velocity	ft/s	223.1	From takeoff calculations
RPM	RPM	1500	Based on improved PT6A model
Altitude	ft	500	Sea level, 500 used to produce usable noise signature

Table 32: XROTOR Outputs for Takeoff Case

Property	Units	Value
Thrust	lbf	1645.7
Ideal Efficiency	N/A	0.8293
Max Ground Noise	dB	69

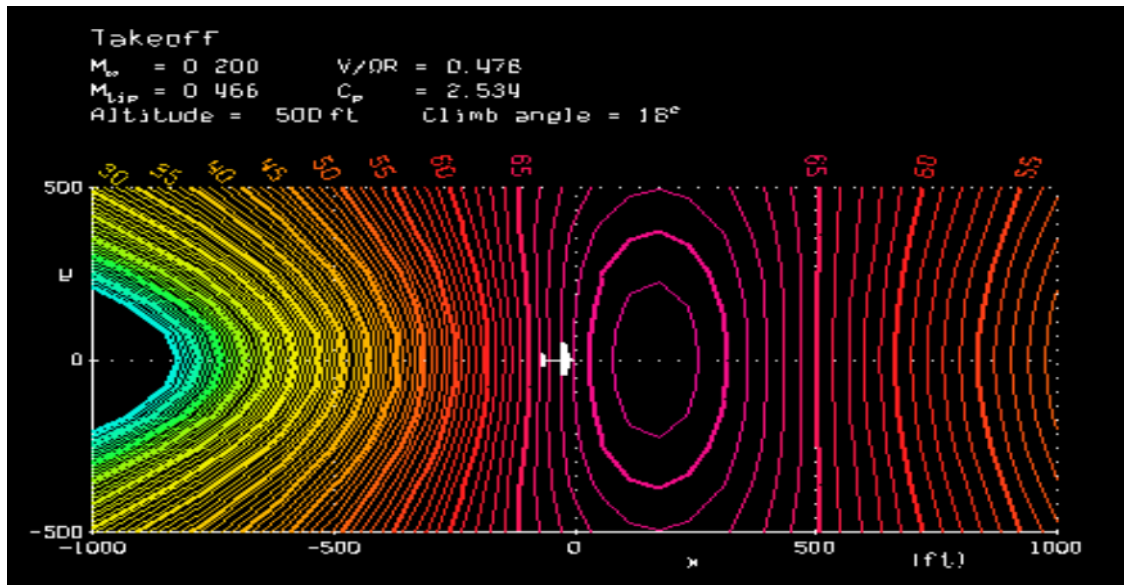


Figure 50: XROTOR Acoustic Analysis for Takeoff Case

Cruise

Below are the inputs and outputs, as well as the acoustic analysis plot, for the XROTOR cruise case.

Table 33: XROTOR Inputs for Cruise Case
 *XROTOR crash, lower power than available used.

Property	Units	Value	Comment
Power	hp	983	Based on improved PT6A model*
Velocity	ft/s	321.5	From cruise calculations
RPM	RPM	1500	Based on improved PT6A model
Altitude	ft	10000	Cruise height

Table 34: XROTOR Outputs for Cruise Case

Property	Units	Value
Thrust	lbf	1052.2
Ideal Efficiency	N/A	0.9136
Max Ground Noise	dB	44

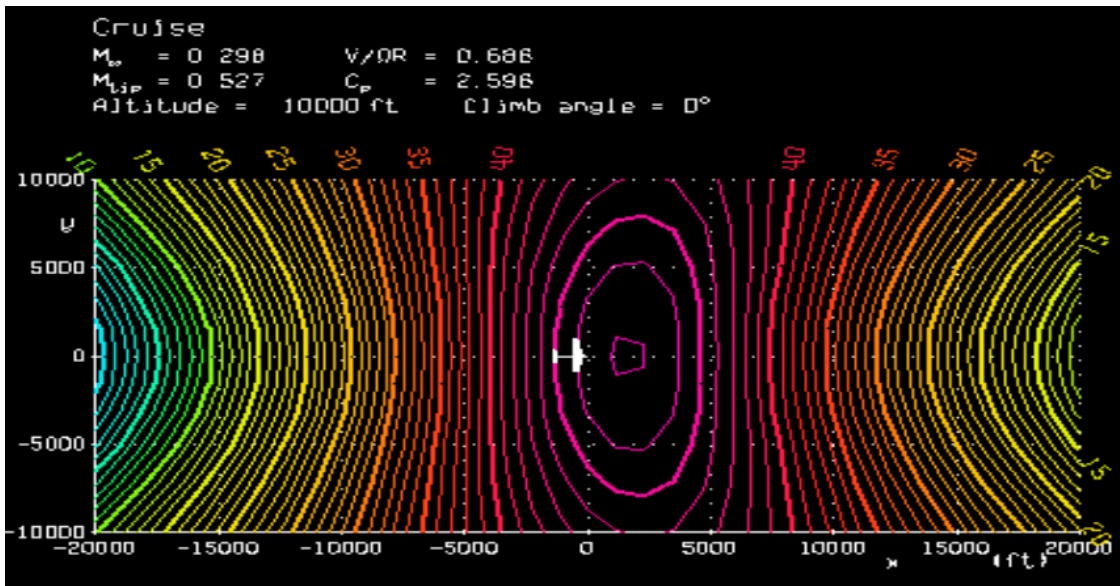


Figure 51: XROTOR Acoustic Analysis for Cruise Case

Service Ceiling

In order to calculate the service ceiling of 34000 ft for the aircraft, a MATLAB script was created to iterate the following equation at varying altitudes:

$$P_s = \frac{V(T - D)}{W} \quad (8)$$

The script begins at 30000 ft and iterates up 100 ft per calculation loop until P_s falls under 100 fpm, the standard for aircraft [44]. In order to iterate the drag value at a new height, a built-in MATLAB density function updates every loop. However, iterating the thrust value at a new height required a thrust slope to be calculated. This was done by

running an additional analysis case at 31000 ft and dividing the thrust difference by 10 to reach the decrease in thrust per 100 ft of gained altitude. The accuracy of the program's output was checked by comparing the calculated thrust at 34000 ft, 519.4 lbf, to an analysis case run in XROTOR at 34000 ft, 521.6 lbf. The full script for this application is located in Appendix III.

Below are the inputs and outputs, as well as the acoustic analysis plot, for the XROTOR service ceiling case.

Table 35: XROTOR Outputs for Service Ceiling Case
 *XROTOR crash, lower power than available used.

Property	Units	Value	Comment
Power	hp	509.6	Based on improved PT6A model*
Velocity	ft/s	295.3	From cruise calculations
RPM	RPM	1500	Based on improved PT6A model
Altitude	ft	34000	Service Ceiling

Table 36: XROTOR Outputs for Service Ceiling Case

Property	Units	Value
Thrust	lbf	521.6
Ideal Efficiency	N/A	0.8896
Max Ground Noise	dB	31

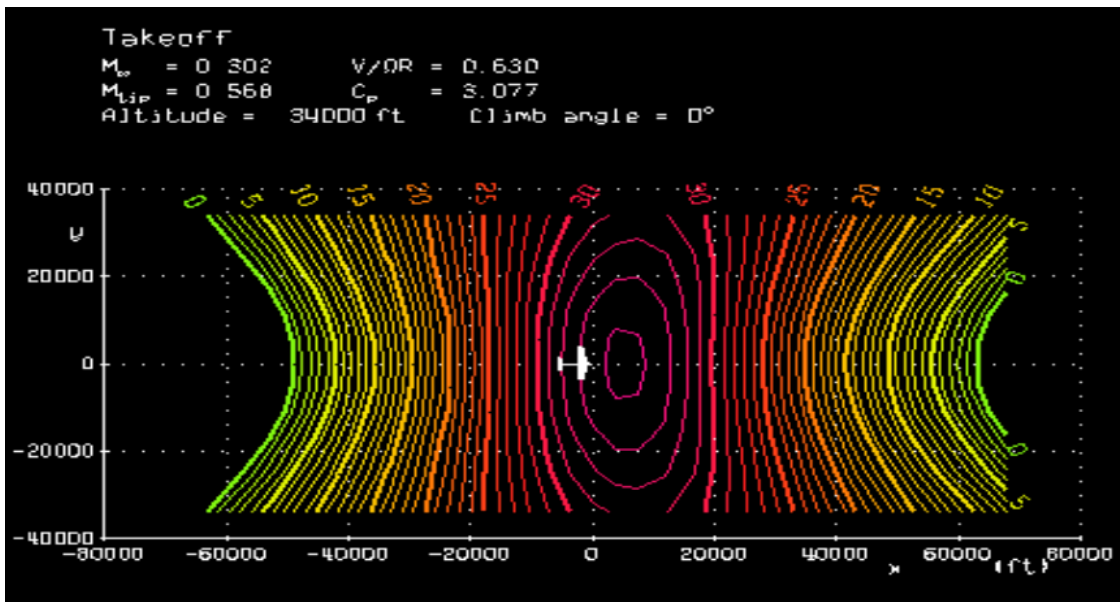


Figure 52: XROTOR Acoustic Analysis for Service Ceiling Case

Other Survivability Considerations

The RFP for this project lists survivability as a main objective and therefore multiple survivability considerations were made for this aircraft. Researching survivability for light attack aircraft illuminated two main methods of

achieving increased survivability: reduced susceptibility and reduced vulnerability. While these two strategies are not mutually exclusive, it was determined that resources should be invested in decreasing vulnerability rather than reducing susceptibility [3]. The main factor in this decision was the significant cost associated with creating a low susceptibility or stealth aircraft. This section contains an annotated list of features and design decisions made to decrease the aircraft's vulnerability to threats.

Chaff

Chaff dispensing systems have been used on combat aircraft since WW2 and provide emergency protection from incoming missiles. The ALE-47 airborne countermeasures dispensing system is currently installed on over 4000 vehicles in 30 countries around the world including: F-18, F-16, and F-15 [45]. This system was chosen specifically because it offers system flexibility, platform customization, and continuous product support.

Titanium Tub

Cockpit and pilot protection are at the forefront of all vulnerability considerations and the RFP states so clearly. This aircraft will feature an 1100 lb titanium 'tub' similar to the one found in the A-10 Thunderbolt II [46]. While this feature adds significant weight to the aircraft, it is critical to the aircraft's survivability and overall mission success.

Gas Tank

The fuel tank is exceedingly important to protect for a combat aircraft and is a major cause of catastrophic system failures. In order to minimize the probability of a fire or explosion, two main considerations were made. The first consideration made is the location, fuel tank protection is maximized by positioning the fuel tank at the top of the central fuselage. [Nicolai] This decreases the probability that an incoming projectile will make impact with the highly explosive jet fuel stored inside. The second consideration involves the use of a nitrogen fuel inerting system to further minimize the probability of a catastrophic explosion. These systems function by pumping inert nitrogen-enriched air into the fuel tank as it empties, keeping the oxygen concentration levels below 12% to prevent combustion [47].

Control Surface redundancy

Dividing control surfaces into multiple sections allows for continued control and capability in the event that one section is damaged. This concept has been employed in the past, with great success, on aircraft such as the A-10 Thunderbolt II [3].

XIV Cost Estimation and Analysis

Venturing from the technical production of the aircraft, the team had to estimate a cost for the aircraft to make a realistic and reasonably priced aircraft. During the cost analysis process the primary focus was calculating the cost of the aircraft and the price of the aircraft. The cost of an aircraft is the total amount of expenditures for resources, usually

measured in dollars, needed to manufacture an aircraft. The price of an aircraft is the amount of dollars paid for the aircraft by customers which includes the profit the manufacture earns from selling the aircraft, which is in addition to the cost to produce the aircraft. Due to the nature of this aircraft's intended assignment as a military light attack aircraft the cost analysis must be adapted based on several assumptions [48]. For example, military/government operations typically have a limited amount of budget. A military's operational goal is to achieve the required missions within a specific budget amount. In order to fulfill this strenuous requirement, the acquisition and operating cost for the aircraft needs to be as low as possible.

XIV.1 Overview of Cost Methodology

A complex aircraft analysis tool was utilized in order to create a well-constructed cost estimation. For this specific project the cost analysis tool used was embedded in the Advanced Aircraft Analysis 4.0 (AAA) program. The cost analysis method used to develop the AAA software was adapted from Dr. Jan Roskam's methodology in the "Airplane Design Part VIII: Airplane Cost Estimation: Design, Development, Manufacturing and Operating." AAA has a variety of categories for aircraft analysis which reflect the Roskam methodology including Weight, Aerodynamics, Performance, Geometry, Propulsion, Stability and Control, Dynamics, Loads, Structures, and Cost. Within each of these categories are various subsections to help with the intended analysis.

This project, in particular, utilized the Cost category which had seven subsets: AMPR Weight Estimation, Research/Development/Test/Evaluation Cost, Acquisition Cost, Military Operating Cost, Life Cycle Cost and Disposal, and Airplane/Engine/Propeller Price Data. By completing all relevant subsets of the Cost Analysis tab, a fairly accurate cost estimation was produced. In order to operate the Cost Tool there were a combination of inputs needed in each category that resulted in the calculation of the output values. The tool requires a combination of previously calculated values, researched numerical factors, historical values, and internally calculated values performed by the program to achieve the intended output values.

XIV.2 Assumptions

Making engineering educated assumptions was critical in completing the cost estimation and analysis. The cost methodology laid out in the Roskam textbook provided specific ranges for various cost factors with detailed guidelines for evaluating each variable. Some variables to highlight that had to be chosen from outside research rather than the Roskam textbook ranges are the service life, number of aircraft manufactured, and number of flights per year. The service life was chosen to be 25 years because during peacetime this is the average aircraft service life and peacetime was assumed for the next 30 years. The number of aircraft manufactured was chosen because the A-29 has been around

since 2015 and a little over 250 aircraft have been sold; using this number it was estimated that in the year 2025 the roll out would consist of approximately 25% of a 5 year project would be produced in the first order. One cannot assume this project would find as much success as the A-29 Super Tucano therefore 60 aircraft seemed reasonable. Finally, the number of flights per year was a calculated output value based mostly on the average mission time of 2 hours. The variable nomenclature can be found in Appendix IV.

Table 37: Input Variables and Assumptions

Variable	Assumption
$F_{\text{difficulty}}$	1.5 (moderate use of technology)
F_{CAD}	1.0 (using manual drafting techniques)
N_{rdte}	20 (military program range 6-20)
$R_{\text{rate 1989}}$	\$65/hr (AAA provided table)
N_{flight}	20 (military aircraft 6-20)
N_{static}	0
F_{mat}	1.0 (aluminum alloy)
$C_{\text{eng rdte}}$	\$1,000,000 (research supported)
$R_{\text{man rdte 1989}}$	\$33/hr (AAA provided table)
$R_{\text{t rate 1989}}$	\$44/hr (AAA provided table)
R_{rdte}	0.33 (suggested in AAA)
F_{obs}	1.1 (no stealth requirement airplanes)
F_{TSf}	0.2 (if test and simulation facilities are required)
F_{pro}	0.1 (for suggested 10% profit)
$F_{\text{fin rate}}$	0.1 (for low interest on military deals)
N_{man}	50 (given in RFP)
$R_{\text{man prog 1989}}$	\$35/hr (AAA provided table)
$R_{\text{t prog 1989}}$	\$45/hr (AAA provided table)
F_{int}	0 (for military airplanes)
t_{ft}	20 (average for military)
F_{fton}	4 (average for military)
$U_{\text{ann ft}}$	1200 (given in RFP)
F_{misc}	0.02 (suggested in AAA)
F_{OL}	1.005 (factor that accounts for oil and lubricants)
N_{yr}	25 yrs (peacetime)
R_{loss}	5 (estimated from A-6 and common aircraft)
R_{crew}	2 (given in RFP)
MHP_{flhr}	2 (suggested in AAA)
F_{disp}	0.01 (suggested in AAA)
Year	2025 (given in RFP)

XIV.3 Calibration

In order to calibrate the AAA tool to perform an accurate cost estimation for the Hummingbird, the program had to be tested and adjusted to find the known value of the A-29 Super Tucano. Although the AAA calculates a variety of cost values the only way to calibrate the cost prototype is to use the acquisition cost because that is the only known value. Life cycle cost and operating cost are difficult to calibrate with due to military deal privilege. Before the calibration

using the A-29 a preliminary cost model produced an acquisition cost per Hummingbird airplane of \$31,990,000; after this excessive evaluation, it was clear some adjustments had to be applied hence the A-29 calibration. By tweaking several variables that had acceptable ranges of large magnitude, the cost model began to take shape. After extensive meddling the calibration was complete once the AAA model produced a cost per airplane of \$25.697 (merely \$250,000 away from the known value). Once this acquisition cost was honed, many inputs stayed the same due to the similarities of the light attack aircraft categories. Major variable changes included the Takeoff Weight, Max level speed, and number of aircraft produced. These relative inputs were altered to represent the values of the Hummingbird in order to produce a comprehensive cost estimation.

XIV.4 Results

The cost analysis evaluation calculated the values for a large amount of cost values. In regards to this project, four essential categories of aircraft cost analysis were identified to be used for a comprehensive cost estimation. The four categories included: Research/ Development/Test/Evaluation (RDTE) Cost, Life Cycle Cost, Total Cost per Plane, and Operating Cost.

The RDTE Cost is used solely as a preliminary evaluation consisting of values accumulated during the beginning phases of the aircraft program involving activities which take a new aircraft all the way from planning and conceptual design to certification. These beginning phases typically include design, construction, and ground and flight testing. The Hummingbird Program's preliminary RDTE Cost evaluation was \$912,131,000.

The Manufacturing and Acquisition Cost category allowed for the total cost per aircraft. This category includes all materials and labor to manufacture and acquire an aircraft. This cost estimation is in the ending phases of the aircraft program. The total cost per aircraft is \$29,322,000.

The Operating Cost category is used as an evaluation only for aircraft in peace time. This method should only be used for preliminary cost estimating purposes. It is important to assume that because this is a military aircraft political and budgetary constraints must be disregarded because these variables are impossible to translate into the cost methodology. After the completion of this cost module section the final Operating Cost evaluation was \$2,495,846,000. This breaks down to \$1742.86 per hour of operation for each individual aircraft. This number is higher than the \$1000 per hour in the press when involving light attack aircraft [49]; this value is an output that uses over 15 variables to calculate. With this in mind, the human error factor of a less than complete understanding of the AAA tool would justify this still reasonable operating cost for a new aircraft program. Two additional important output values include the maintenance cost for the program and fuel costs. The Program Cost for Fuel, Oil and Lubricants came out to \$152,694,000, while the Direct Maintenance Personnel Cost for the Program was \$865,383,000.

The final cost category was the Life Cycle Cost of a military aircraft. This methodology uses all previous cost

estimations to calculate the total life cycle cost of a program. This cost is a summation of the program's total cost for RDTE, Acquisition, Operation, and Disposal over the lifetime of a program. The program's Life Cycle Cost was \$2,561,744,000. This is the total cost that all governments and or militaries must focus on in any cost discussions due to its comprehensive assessment; in this instance the comprehensive assessment of the entire Hummingbird Program cost.

XV Conclusion

The Hummingbird is an ideal solution to the RFP since it is more than capable of meeting the desired performance requirements. The acquisition cost is higher at \$29 million than other aircraft though the operating cost, at \$1743 per flight hour, is far lower than the majority of aircraft in service. The plane is conventionally designed to minimize cost and maximize opportunities for "off the shelf" parts. The aircraft is confidently able to carry out the design and ferry missions with room to spare. There is still a large margin available in terms of both space and weight for future iterations. Future work could include using that free space for expanding the plane's capabilities, such as more survivability measures, or for a higher fidelity optimization and weight and cost reduction. In its current form, however, Team Hummingbird fully recommends The Hummingbird as the initial conceptual design for comprehensive design and production work.

XVI Acknowledgements

Team Hummingbirds would like to thank the University of Virginia Mechanical and Aerospace Engineering department for their support in this project. In addition to Dr. Quinlan, Mr. David Eames has provided vital feedback for this design. Lastly, the team would like to thank its sister teams, Team Kestrel and Team Wade Boggs, for collaborating in overcoming the high learning curve of the tools used throughout the project.

Bibliography

- [1] How does the pratt whitney canada pt6 differ from other turboprop engines? url=<https://aviation.stackexchange.com/questions/22151/how-does-the-pratt-whitney-canada-pt6-differ>.
- [2] Saeed Farokhi. *Aircraft Propulsion*. John Wiley Sons, 2 edition, 2014.
- [3] Leland M. Nicolai and Grant Carichner. *Fundamentals of aircraft design: Volume I aircraft design*. American Institute of Aeronautics Astronautics, 2010.
- [4] *PT6A-60 SERIESTRAINING MANUAL*. Nov 2007.
- [5] Wikipedia contributors. Brayton cycle. url=http://en.wikipedia.org/w/index.php?title=Brayton_cycle&oldid=993744786, Dec2020.
- [6] New manufacturing milestone: 30,000 additive fuel nozzles. url=<http://www.ge.com/additive/stories/new-manufacturing-milestone-30000-additive-fuel-nozzles>.
- [7] Arthur Thirion, Emily Newton, Olawale Olayemi, and Vineeth Venugopal. High-temperature materials for gas turbines and their future. url=<https://matmatch.com/blog/the-future-of-high-temperature-materials-for-gas-turbines/>, Aug 2018.
- [8] Aeronautics, Space Engineering Board, Division on Engineering, Physical Sciences, National Academies of Sciences Engineering, and Medicine. *Commercial aircraft propulsion and energy systems research: Reducing global carbon emissions*. National Academies Press, 2016.
- [9] Request for proposal austere field light attack aircraft. url=https://www.aiaa.org/docs/default-source/uploadedfiles/education-and-careers/university-students/design-competitions/undergraduate-team-aircraft-design-competition/aiaa-2021-undergraduate-team-aircraft-design-rfp—light-attack-aircraft-2-.pdf?sfvrsn=b54e3cac_2.
- [10] Jan Roskam. *Airplane Design Part 1*. Darcorporation, 2005.

- [11] Jan Roskam. *Airplane Design Part 2*. Darcorporation, 2012.
- [12] darcorp. Advanced aircraft analysis. url=<https://www.darcorp.com/advanced-aircraft-analysis-software/>, Oct 2018.
- [13] Flight optimization system (flops) software v.9. url=<https://software.nasa.gov/software/LAR-18934-1>, journal=Nasa.gov.
- [14] GasTurb GmbH. Gasturb - home. url=<https://www.gasturb.de/>.
- [15] NASA. Openvsp. url=<http://openvsp.org/>.
- [16] Student edition. url=<https://www.solidworks.com/product/students>.
- [17] Harold Youngren Mark Drela. Xrotor. url=<https://web.mit.edu/drela/Public/web/xrotor/>.
- [18] Jan Roskam. *Airplane design Part 3*. DARcorporation, Lawrence, Kan, 1985.
- [19] Mk 82 aircraft bomb. url=<http://characterisationexplosiveweapons.org/studies/annex-e-mk82-aircraft-bombs/>.
- [20] Agm-65 maverick tactical air-ground missile. url=<https://www.airforce-technology.com/projects/agm-65-maverick-tactical-missile/>, Jan 2021.
- [21] Agm-65 maverick. url=<https://www.af.mil/About-Us/Fact-Sheets/Display/Article/104577/agm-65-maverick/>, Aug 2003.
- [22] Aim-9x sidewinder missile. url=<https://www.raytheonmissilesanddefense.com/capabilities/products/aim-9x-sidewinder-missile>.
- [23] Gun pod weapon system. url=<https://dillonaero.com/product/gunpodweaponsystem/>, journal=Dillonaero.com.
- [24] Fn m3p. url=<https://fnamerica.com/products/weapon-systems/fn-m3p/>, Sep 2009.
- [25] Ac-130h spectre - military aircraft. url=<https://fas.org/man/dod-101/sys/ac/ac-130.htm>.
- [26] Vspaero tutorial. url=<http://openvsp.org/wiki/doku.php?id=vspaerotutorial>.
- [27] Naca 63-415 airfoil (n63415-il). url=<http://airfoiltools.com/airfoil/details?airfoil=n63415-il>.
- [28] Aviation photo 1955280: Embraer a-29b super tucano (emb-314). url=<https://www.airliners.net/photo/Colombia—Air/Embraer-A-29B-Super/1955280>.
- [29] The air force just finished strapping new wings onto the a-10 warthog to keep it flying until the late 2030s. *Business Insider*, Aug 2019.

- [30] Daniel P. Raymer. *Aircraft design: A conceptual approach*. American Institute of Aeronautics Astronautics, 5 edition, 2012.
- [31] Aerospace engineering - airplane design (aerodynamic). url=<https://nptel.ac.in/courses/101/106/101106035/>.
- [32] Bandu N. Pamadi. *Performance, stability, dynamics, control*. American Institute of Aeronautics Astronautics, 3 edition, 2015.
- [33] Dynamic longitudinal, directional, and lateral stability. url=https://www.centennialofflight.net/essay/Theories_of_Flight/Stability_I
- [34] X-57 maxwell aircraft. url=<https://www.aerospace-technology.com/projects/x-57-maxwell-aircraft/>, Aug 2016.
- [35] Brayton cycle experiment jet engine. url=<http://www.turbinetechnologies.com/educational-lab-products/turbojet-engine-lab/brayton-cycle-experiment-jet-engine>.
- [36] A. V. Sotov, A. V. Agapovichev, V. G. Smelov, V. V. Kokareva, M. O. Dmitrieva, A. A. Melnikov, S. P. Golanov, and Yu M. Anurov. Investigation of the in-738 superalloy microstructure and mechanical properties for the manufacturing of gas turbine engine nozzle guide vane by selective laser melting. *The international journal of advanced manufacturing technology*, 107(5–6):2525–2535, 2020.
- [37] Shunyu Liu and Yung C. Shin. Additive manufacturing of ti6al4v alloy: A review. *Materials Design*, 164:107552, 2019.
- [38] Rob Finfrock. Why this hydrogen-powered engine could be the future of flying, May 2020.
- [39] Committee on Aeronautics Research, Technology for Environmental Compatibility, Studies, Information Services, Aeronautics, Space Engineering Board, Transportation Research Board, Division on Engineering, Physical Sciences, and National Research Council. *Securing the future of U.S. air transportation: A system in peril*. National Academies Press, 2003.
- [40] Kenneth S. Brentner, Bolor Erdene Zolbayar, and Thomas F. Jaworski. An investigation of noise from electric, low-tip-speed aircraft propellers. 2018. Funding Information: This work has been partially supported by Georgia Tech as part of their NASA LEARN project entitled “Economical Thin-Haul Aviation Concepts (ETHACS)” and partially by Penn State. Any opinions expressed within this paper are solely those of the authors. Publisher Copyright: © Copyright 2018 by AHS International, Inc. All rights reserved.; AHS International Technical Meeting on Aeromechanics Design for Transformative Vertical Flight 2018 ; Conference date: 16-01-2018 Through 18-01-2018.
- [41] Vistasp Edulji. *V-N Plotter*. November 8, 20202.

- [42] MIL-A-8861B. Feb 1986.
- [43] Sivakumar Ramakrishnan. *V-n Diagram*. Oct 2020.
- [44] FAA. *Airplane Flying Handbook*. 2016.
- [45] Ale-47 airborne countermeasures dispenser system. url=<https://www.baesystems.com/en-us/product/ale47-airborne-countermeasures-dispenser-system>.
- [46] Dennis R. Jenkins. *Warbirdtech 20: Fairchild-Republic A/Oa-10 Warthog*. Specialty Press, 1999.
- [47] Safer flight w/ fuel tank aircraft nitrogen generating system. url=<https://www.generon.com/aircraft-nitrogen-generating-systems-ags-for-fuel-tank-inerting-system/>, Aug 2019.
- [48] Jan Roskam. *Airplane design PT. VIII: Airplane cost estimation: Design, development, manufacturing and operating*. Darcorporation, 1990.
- [49] Too little for too much? or a lot for a little? the air force oa-x light-attack program. url=<https://www.csis.org/too-little-too-much-or-lot-little-air-force-oa-x-light-attack-program>.

Appendices

I Initial TOGW Calculation

Table 38: Initial TOGW Calculation Varying TOGW by 1000 lb

W_fixed	W_fuel	W_TO	W_empty_avail	W_empty_req
3600	1882.590308	8000	2517.409692	3802.103025
3600	2117.914096	9000	3282.085904	4250.747612
3600	2353.237885	10000	4046.762115	4696.752368
3600	2588.561673	11000	4811.438327	5140.395514
3600	2823.885462	12000	5576.114538	5581.903229
3600	3059.20925	13000	6340.79075	6021.462939
3600	3294.533039	14000	7105.466961	6459.232434
3600	3529.856827	15000	7870.143173	6895.346348
3600	3765.180616	16000	8634.819384	7329.920876
3600	4000.504404	17000	9399.495596	7763.057297
3600	4235.828193	18000	10164.17181	8194.844656

Table 39: Finer Initial TOGW Calculation Varying TOGW by 200 lb

W_fixed	W_fuel	W_TO	W_empty_avail	W_empty_req
2800	2242.691479	9530.237015	4487.545536	4487.545536
3000	2389.991233	10156.18203	4766.190801	4766.190801
3200	2536.625756	10779.30018	5042.674425	5042.674425
3400	2682.643675	11399.79809	5317.154417	5317.154417
3600	2828.087391	12017.85595	5589.768557	5589.768557
3800	2972.99418	12633.63215	5860.63797	5860.63797
4000	3117.397049	13247.26696	6129.869914	6129.869914
4200	3261.325416	13858.8854	6397.559983	6397.559983

II Takeoff and Landing Assumptions

Table 40: Assumed Values for Takeoff and Landing Calculations

Parameter	Value	Comment
Rolling Coefficient	0.025	MIL Standard
Ground Friction	0.04	Firm and dry dirt
Ground CL	0.26	Nikolai Equation
CD_0	0.022	Averaged from Similar Aircraft
delta CD_Flaps	0.01	Nikolai
delta CD_gear	0.035	Nikolai
CD_brake	0.43	Nikolai

III Noise Signatures

III.1 XROTOR Outputs

```

=====
Free Tip Vortex Wake Formulation Solution: Takeoff
no. blades : 5          radius(m) : 0.9100      Wake adv. ratio: 0.91712
thrust(N)   : 0.732E+04 power(W)   : 0.969E+06      adv. ratio: 0.47572
Efficiency  : 0.5137    speed(m/s) : 68.000       torque(N-m): 0.617E+04
Eff induced: 0.5187    Eff ideal  : 0.8293    Tcoef      : 1500.000
Tnacel(N)  : -2.8373   hub rad.(m): 0.0750     disp. rad. : 0.9932
Tvisc(N)   : -45.7269 Pvisc(W)  : 0.335E+04
rho(kg/m3) : 1.22600   Vsound(m/s): 340.000   mu(kg/m-s) : 0.1780E-04
-----
Sigma: 0.73871
          Ct: 0.87115   Cp: 2.53440   J: 1.49451
          Tc: 0.99320   Pc: 1.93341  adv: 0.47572

i  r/R  c/R  beta(deg)  CL   Cd  REX10^6  Mach  effi  effp  na.u/U
1  0.090 0.1606 86.09 0.240 0.0081 0.69 0.203 0.560 0.681 0.000
3  0.155 0.2049 81.38 0.538 0.0071 0.91 0.208 0.734 0.942 0.000
5  0.247 0.3097 76.48 0.765 0.0060 1.46 0.221 0.714 0.976 0.000
7  0.343 0.4062 73.37 0.957 0.0054 2.06 0.238 0.650 0.985 0.000
9  0.437 0.4690 70.92 1.113 0.0052 2.60 0.260 0.601 0.989 0.000
11 0.527 0.4994 68.89 1.235 0.0051 3.02 0.284 0.563 0.991 0.000
13 0.612 0.5041 67.10 1.323 0.0051 3.32 0.309 0.535 0.992 0.000
15 0.691 0.4889 65.44 1.381 0.0052 3.48 0.334 0.514 0.992 0.000
17 0.762 0.4576 63.82 1.416 0.0053 3.50 0.359 0.500 0.992 0.000
19 0.825 0.4130 62.22 1.435 0.0056 3.35 0.381 0.492 0.992 0.000
21 0.879 0.3575 60.80 1.446 0.0059 3.05 0.400 0.487 0.992 0.000
23 0.924 0.2929 59.82 1.458 0.0064 2.60 0.417 0.482 0.991 0.000
25 0.959 0.2218 59.31 1.473 0.0074 2.03 0.430 0.478 0.990 0.000
27 0.983 0.1464 59.13 1.497 0.0107 1.37 0.439 0.489 0.986 0.000
29 0.997 0.0722 59.10 1.518 s 0.0621 0.68 0.445 0.622 0.920 0.000
=====
Free Tip Vortex Wake Formulation Solution: Cruise
no. blades : 5          radius(m) : 0.9100      Wake adv. ratio: 1.08105
thrust(N)   : 0.468E+04 power(W)   : 0.733E+06      adv. ratio: 0.68559
Efficiency  : 0.6259    speed(m/s) : 98.000       torque(N-m): 0.467E+04
Eff induced: 0.6342    Eff ideal  : 0.9136    Tcoef      : 1500.000
Tnacel(N)  : -0.9176   hub rad.(m): 0.0750     disp. rad. : 0.4141
Tvisc(N)   : -45.9067 Pvisc(W)  : 0.253E+04
rho(kg/m3) : 0.90455   Vsound(m/s): 328.800   mu(kg/m-s) : 0.1682E-04
-----
Sigma: 0.73871
          Ct: 0.75447   Cp: 2.59644   J: 2.15385
          Tc: 0.41415   Pc: 0.66172  adv: 0.68559

i  r/R  c/R  beta(deg)  CL   Cd  REX10^6  Mach  effi  effp  na.u/U
1  0.090 0.1606 86.09 0.117 0.0079 0.78 0.300 0.657 0.217 0.000
3  0.155 0.2049 81.38 0.253 0.0069 1.00 0.305 0.847 0.852 0.000
5  0.247 0.3097 76.48 0.383 0.0057 1.57 0.315 0.840 0.946 0.000
7  0.343 0.4062 73.37 0.526 0.0050 2.15 0.330 0.774 0.972 0.000
9  0.437 0.4690 70.92 0.660 0.0047 2.62 0.348 0.723 0.981 0.000
11 0.527 0.4994 68.89 0.777 0.0045 2.96 0.368 0.683 0.986 0.000
13 0.612 0.5041 67.10 0.872 0.0045 3.17 0.390 0.653 0.988 0.000
15 0.691 0.4889 65.44 0.945 0.0045 3.25 0.413 0.630 0.989 0.000
17 0.762 0.4576 63.82 0.997 0.0046 3.20 0.434 0.616 0.990 0.000
19 0.825 0.4130 62.22 1.033 0.0048 3.02 0.455 0.608 0.990 0.000
21 0.879 0.3575 60.80 1.059 0.0050 2.72 0.473 0.603 0.990 0.000
23 0.924 0.2929 59.82 1.084 0.0054 2.30 0.488 0.597 0.990 0.000
25 0.959 0.2218 59.31 1.113 0.0060 1.78 0.500 0.589 0.989 0.000
27 0.983 0.1464 59.13 1.156 0.0072 1.20 0.508 0.585 0.987 0.000
29 0.997 0.0722 59.10 1.230 0.0098 0.60 0.513 0.589 0.984 0.000
=====

```

```

=====
Free Tip Vortex Wake Formulation Solution: 30000ft
no. blades : 5          radius(m) : 0.9100      Wake adv. ratio: 1.12497
thrust(N)   : 0.270E+04 power(W)   : 0.440E+06   adv. ratio: 0.62962
Efficiency  : 0.5518    speed(m/s) : 90.000    torque(N-m): 0.280E+04
Eff induced: 0.5597    Eff ideal  : 0.8897    rpm       : 1500.000
Tnacel(N)  : -0.7114   hub rad.(m): 0.0750    Tcoef    : 0.5576
Tvisc(N)   : -28.5880  Pvisc(W)  : 0.157E+04  disp. rad.: 0.0750
rho(kg/m3) : 0.45922   Vsound(m/s): 303.280  mu(kg/m-s) : 0.1477E-04
-----
Sigma: 0.73871
      Ct: 0.85670    Cp: 3.07080    J: 1.97802
      Tc: 0.55758    Pc: 1.01041  adv: 0.62962

i  r/R  c/R  beta(deg)  CL    Cd  REx10^6  Mach  effi  effp  na.u/U
1  0.090 0.1606 89.45 0.231 0.0099 0.41 0.299 0.312 0.035 0.000
3  0.155 0.2049 84.74 0.465 0.0088 0.53 0.304 0.667 0.882 0.000
5  0.247 0.3097 79.84 0.623 0.0074 0.84 0.315 0.710 0.954 0.000
7  0.343 0.4062 76.73 0.780 0.0066 1.15 0.331 0.668 0.974 0.000
9  0.437 0.4690 74.29 0.926 0.0063 1.41 0.351 0.630 0.982 0.000
11 0.527 0.4994 72.25 1.051 0.0062 1.60 0.374 0.600 0.985 0.000
13 0.612 0.5041 70.46 1.152 0.0062 1.72 0.399 0.575 0.987 0.000
15 0.691 0.4889 68.80 1.227 0.0063 1.78 0.423 0.556 0.988 0.000
17 0.762 0.4576 67.18 1.279 0.0065 1.76 0.447 0.544 0.989 0.000
19 0.825 0.4130 65.58 1.314 0.0067 1.66 0.469 0.537 0.989 0.000
21 0.879 0.3575 64.16 1.339 0.0071 1.50 0.489 0.533 0.989 0.000
23 0.924 0.2929 63.18 1.362 0.0077 1.27 0.506 0.528 0.988 0.000
25 0.959 0.2218 62.67 1.391 0.0086 0.99 0.519 0.522 0.987 0.000
27 0.983 0.1464 62.49 1.436 0.0105 0.66 0.529 0.522 0.985 0.000
29 0.997 0.0722 62.46 1.505 s 0.0206 0.33 0.534 0.574 0.973 0.000
=====
Free Tip Vortex Wake Formulation Solution: 31000ft
no. blades : 5          radius(m) : 0.9100      Wake adv. ratio: 1.10490
thrust(N)   : 0.256E+04 power(W)   : 0.410E+06   adv. ratio: 0.62962
Efficiency  : 0.5618    speed(m/s) : 90.000    torque(N-m): 0.261E+04
Eff induced: 0.5698    Eff ideal  : 0.8911    rpm       : 1500.000
Tnacel(N)  : -0.6360   hub rad.(m): 0.0750    Tcoef    : 0.5484
Tvisc(N)   : -27.1394  Pvisc(W)  : 0.151E+04  disp. rad.: 0.0750
rho(kg/m3) : 0.44276   Vsound(m/s): 301.756  mu(kg/m-s) : 0.1466E-04
-----
Sigma: 0.73871
      Ct: 0.84253    Cp: 2.96649    J: 1.97802
      Tc: 0.54836    Pc: 0.97609  adv: 0.62962

i  r/R  c/R  beta(deg)  CL    Cd  REx10^6  Mach  effi  effp  na.u/U
1  0.090 0.1606 88.62 0.209 0.0100 0.41 0.301 0.391 0.145 0.000
3  0.155 0.2049 83.91 0.428 0.0088 0.53 0.306 0.704 0.878 0.000
5  0.247 0.3097 79.01 0.584 0.0073 0.84 0.317 0.734 0.953 0.000
7  0.343 0.4062 75.90 0.741 0.0066 1.16 0.333 0.686 0.973 0.000
9  0.437 0.4690 73.45 0.886 0.0062 1.42 0.354 0.645 0.981 0.000
11 0.527 0.4994 71.41 1.011 0.0061 1.61 0.377 0.612 0.985 0.000
13 0.612 0.5041 69.63 1.111 0.0061 1.73 0.401 0.586 0.987 0.000
15 0.691 0.4889 67.97 1.186 0.0062 1.78 0.426 0.567 0.988 0.000
17 0.762 0.4576 66.34 1.238 0.0064 1.76 0.450 0.553 0.989 0.000
19 0.825 0.4130 64.74 1.273 0.0066 1.67 0.473 0.546 0.989 0.000
21 0.879 0.3575 63.33 1.299 0.0069 1.50 0.493 0.542 0.989 0.000
23 0.924 0.2929 62.35 1.323 0.0075 1.28 0.510 0.536 0.988 0.000
25 0.959 0.2218 61.84 1.352 0.0084 0.99 0.523 0.530 0.987 0.000
27 0.983 0.1464 61.65 1.398 0.0101 0.67 0.533 0.528 0.985 0.000
29 0.997 0.0722 61.63 1.478 0.0151 0.33 0.538 0.548 0.979 0.000
=====

```

```

=====
Free Tip Vortex Wake Formulation Solution: Service Ceiling
no. blades : 5          radius(m) : 0.9100      Wake adv. ratio: 1.12620
thrust(N)   : 0.232E+04 power(W)   : 0.380E+06   torque(N-m): 0.242E+04
Efficiency  : 0.5508    speed(m/s) : 90.000    rpm       : 1500.000
Eff induced: 0.5591    Eff ideal  : 0.8896    Tcoef    : 0.5578
Tnacel(N)  : -0.6142   hub rad.(m): 0.0750    disp. rad.: 0.0750
Tvisc(N)   : -25.8872 Pvisc(W)  : 0.142E+04
rho(kg/m3) : 0.39536   Vsound(m/s): 297.560   mu(kg/m-s) : 0.1437E-04
-----
Sigma: 0.73871
          Ct: 0.85703   Cp: 3.07755   J: 1.97802
          Tc: 0.55780   Pc: 1.01263  adv: 0.62962

i  r/R  c/R  beta(deg)  CL   Cd  REx10^6  Mach  effi  effp  na.u/U
1  0.090 0.1606 89.46 0.231 0.0104 0.37 0.305 0.312-0.014 0.000
3  0.155 0.2049 84.75 0.466 0.0092 0.47 0.310 0.666 0.876 0.000
5  0.247 0.3097 79.85 0.624 0.0077 0.74 0.321 0.709 0.952 0.000
7  0.343 0.4062 76.74 0.781 0.0069 1.02 0.338 0.668 0.972 0.000
9  0.437 0.4690 74.29 0.927 0.0066 1.25 0.358 0.630 0.981 0.000
11 0.527 0.4994 72.25 1.053 0.0065 1.42 0.381 0.599 0.985 0.000
13 0.612 0.5041 70.46 1.154 0.0065 1.53 0.406 0.574 0.987 0.000
15 0.691 0.4889 68.80 1.229 0.0066 1.57 0.431 0.556 0.988 0.000
17 0.762 0.4576 67.18 1.282 0.0068 1.55 0.456 0.543 0.988 0.000
19 0.825 0.4130 65.58 1.317 0.0071 1.47 0.478 0.536 0.989 0.000
21 0.879 0.3575 64.16 1.342 0.0074 1.33 0.498 0.532 0.988 0.000
23 0.924 0.2929 63.18 1.366 0.0080 1.13 0.516 0.527 0.988 0.000
25 0.959 0.2218 62.67 1.394 0.0091 0.87 0.529 0.521 0.987 0.000
27 0.983 0.1464 62.49 1.439 0.0113 0.59 0.539 0.521 0.984 0.000
29 0.997 0.0722 62.46 1.506 s 0.0232 0.29 0.544 0.578 0.969 0.000

```

III.2 Matlab Script for Service Ceiling

Ps = 200; %fpm Thrust = 607; %lbf alt = 30000; %feet while Ps > 101 alt2 = alt *.3048; Cd = .05; [T, a, P, rho] = atmosisa(alt2); %SI units rho = rho / 515.378; V = 295; %ft/s A = 278.85; %ft² Drag = Cd * .5 * rho * V² * A; %lbf W = 10000; %lbs Ps = (V/W *(Thrust-Drag))*60 %fpm alt Thrust alt = alt + 100; Thrust = Thrust - 9.5/4.448; end

IV Cost Variables

Table 41: Variables Nomenclature

Variable	Definition	Variable	Assumption
$F_{\text{difficulty}}$	Difficulty Judgement Factor	N_{man}	# of Airplanes Produced to Production Standard in Manufacturing Phase
F_{CAD}	CAD Judgement Factor	$R_{\text{man prog 1989}}$	Manufacturing Labor Rate for the Entire Program in 1989
N_{rdte}	# of Airplanes Produced for the RDTE Phase	$R_{\text{t prog 1989}}$	Tooling Labor Rate for the Entire Program in 1989
$R_{\text{rate 1989}}$		F_{int}	Interior Cost Factor
N_{flight}	# of Flight Test Airplanes	t_{ft}	# of Flight Test Hours
N_{static}	# of Static Test Airplanes	F_{ftoh}	Overhead Factor for Production Flight Tests
F_{mat}	Materials Correction Factor	$U_{\text{ann ft}}$	Annual Utilization in Flight Hours
$C_{\text{eng rdte}}$	Cost per Engine during RDTE phase	F_{misc}	Cost of Miscellaneous Items Factor
$R_{\text{man rdte 1989}}$	Manufacturing Labor Rate in RDTE Phase in 1989	F_{OL}	Factor Which Accounts for the Cost of Oil and Lubricants
$R_{\text{t rate 1989}}$	Tooling Labor Rate in RDTE Phase in 1989	N_{yr}	Operating Years of the Airplane
R_{rdte}	RDTE Production Rate in Units per Month	R_{loss}	Annual Loss Rate
F_{obs}	Low Observable Factor	R_{crew}	Crew Ratio Per Airplane
F_{Tsf}	Cost Adjustment Factor for Test and Simulation Facilities	MHP_{flhr}	# of Maintenance Man hours per Flight Hour
F_{pro}	RDTE Profit Fraction	F_{disp}	Disposal Cost Factor
$F_{\text{fin rate}}$	RDTE Finance Cost Fraction	Year	The Year